

# Cascade equations and hadronic interactions at very high energies

Zur Erlangung des akademischen Grades  
eines Doktors der Naturwissenschaften  
von der Fakultät für Physik des  
Karlsruher Instituts für Technologie (KIT)

genehmigte Dissertation

von  
Herr Dipl.-Phys. Dipl.-Ing. Anatoli Fedynitch  
aus  
Moskau

Referent: Prof. Dr. Dr. h.c. Johannes Blümner  
Koreferent: Priv.-Doz. Dr. Stefan Gieseke  
Betreuer: Dr. Ralph Engel (KIT)  
Dr. Alfredo Ferrari (CERN)

Tag der mündlichen Prüfung: 2015/11/27



Das tiefste und erhabenste Gefühl, dessen wir fähig sind, ist das Erlebnis des Mystischen. Aus ihm allein keimt wahre Wissenschaft. Wem dieses Gefühl fremd ist, wer sich nicht mehr wundern und in Ehrfurcht verlieren kann, der ist seelisch bereits tot.

(A. Einstein)



# Inhaltsverzeichnis

<b>1</b>	<b>Introduction</b>	<b>1</b>
<b>I</b>	<b>Atmospheric cascades</b>	<b>3</b>
<b>2</b>	<b>Atmospheric cascades</b>	<b>5</b>
2.1	Cascade Equations . . . . .	6
2.1.1	Hadron solutions . . . . .	9
2.1.2	Decays and lepton production . . . . .	11
2.2	Increasing the level of detail . . . . .	13
2.2.1	The flux of cosmic rays . . . . .	14
2.2.2	Geometry and atmosphere . . . . .	16
2.3	Hadronic interactions . . . . .	18
<b>3</b>	<b>Matrix form of the coupled cascade equations</b>	<b>23</b>
3.1	Derivation of the matrix notation . . . . .	24
3.2	Eigenmodes, stiffness and stability . . . . .	28
3.3	The resonance approximation . . . . .	30
<b>4</b>	<b>The MCEQ code</b>	<b>35</b>
4.1	Goals and motivation . . . . .	35
4.2	About the software . . . . .	36
4.2.1	General design and program structure . . . . .	36
4.2.2	Package MCEQ . . . . .	38
4.2.3	Performance acceleration and the <code>kernels</code> module . . . . .	40
4.2.4	Current and future execution performance . . . . .	45
4.3	Supplied models . . . . .	46
<b>5</b>	<b>Atmospheric lepton calculations</b>	<b>49</b>
5.1	Comparison with Monte Carlo and iterative solutions . . . . .	49
5.2	Which particles matter in lepton production? . . . . .	51
5.3	Studying hadronic interactions through cosmic ray observations	54
5.3.1	Phase-space . . . . .	55
5.3.2	Comparison with high-precision measurements of atmospheric muons . . . . .	57
5.3.3	What do we learn about hadronic interactions? . . . . .	57

5.4	The effect of the atmosphere on inclusive leptons . . . . .	62
5.5	Predictions of conventional and prompt fluxes . . . . .	65
<b>II</b>	<b>Aspects of hadronic interactions</b>	<b>69</b>
<b>6</b>	<b>Has the LHC reached the black disk limit?</b>	<b>71</b>
6.1	Introduction . . . . .	71
6.2	Multiplicities at LHC energies . . . . .	72
6.3	About $S$ -matrix theory and the pomeron . . . . .	73
6.4	Impact parameter representation . . . . .	74
6.5	Eikonal approximation and cross-sections in PHOJET . . . . .	75
6.6	Reconstructing the impact parameter amplitude from elastic scattering . . . . .	78
6.6.1	Interference structure of the complex scattering amplitude	78
6.6.2	Interpolation of the elastic amplitude . . . . .	80
6.7	Results and discussion . . . . .	82
6.8	Returning to multiplicity distributions at the LHC . . . . .	83
<b>7</b>	<b>A new revision of PHOJET and DPMJET</b>	<b>89</b>
7.1	Technical state of the programs at the beginning of the project .	90
7.1.1	PHOJET . . . . .	90
7.1.2	DPMJET . . . . .	91
7.2	Goals for the new version . . . . .	93
7.3	Multi-particle modification . . . . .	94
7.4	Modifications for cascades and very high energies . . . . .	96
7.4.1	Proton-proton cross-sections . . . . .	96
7.4.2	Meson-nucleon cross-sections . . . . .	98
7.5	New parton density functions . . . . .	99
7.5.1	Choosing a PDF for very high energy applications . . . . .	100
7.5.2	A comment on Generalized Parton Densities . . . . .	103
7.5.3	New standard PDF for PHOJET . . . . .	104
7.6	Insight in the energy dependence of the hard cross-section through LHC data . . . . .	106
7.6.1	Hard cross-section and multi-parton interactions . . . . .	106
7.6.2	New energy dependence of transverse momentum cutoff .	108
7.7	DPMJET vs. LHC data . . . . .	111
7.8	Discussion . . . . .	114
<b>8</b>	<b>Summary and outlook</b>	<b>119</b>
<b>A</b>	<b>Supporting programs</b>	<b>137</b>
A.1	Package CRFluxModels . . . . .	137
A.2	Package ParticleDataTool . . . . .	137
A.3	Package PyInteractionModels . . . . .	138
A.4	Package SpectraForMCEq . . . . .	139

A.5	Tool PYTHIADECAYS . . . . .	140
A.6	Package AcceleratorData . . . . .	140
A.7	MCVD - Monte Carlo ValiDation . . . . .	141



# Chapter 1

## Introduction

The observation of mysterious phenomena in space, such as dark matter, dark energy or the big bang, requires science to find a fundamental connection between microscopic quantum world and the largest scales of the universe. Astroparticle physics is a discipline, which sees particles as one of the carriers of information about distant astrophysical sources where they were created and accelerated. A number of processes, which occur during the transport of particles through space and matter on the way to the Earth obscure the information about their sources, but in turn encode some additional properties of the space in between. In the latest interaction our atmosphere acts as a dense propagation medium and detector at the same time, adding more challenges to the investigation of the particle's history.

Although the transport happens on astrophysical time and distance scales, each particle undergoes microscopical particle physics processes that can be studied to some extent in laboratory conditions. This allows us to model phenomena, which we believe to understand, at high precision to avoid introducing additional uncertainties due to our calculation methods, for example. However, some parts of particle physics are far from being completely understood and in fact, this discipline still suffers from a lack of consistent description from first principles. Complex models of hadronic interactions, which describe the creation of secondary particles when two hadrons collide, try to merge phenomenology with theory and create different scenarios about processes at scales of the weak and strong force. Indeed there is enough room for coexistence of multiple scenarios or multiple models, since each experiment shows only a little slice of the entire phase-space, leaving bigger gaps in the knowledge.

The aim of this thesis is to study the interface between these two worlds, the microscopic world of particle interactions and the macroscopic world of particle transport. The most nearby particle cascades at high energies and larger scales are extensive air showers in the atmosphere of the Earth. They are well studied in the context of cosmic ray physics with a good coverage of measurements. In particular leptons, which are created in decays of secondary particles, reflect the history of the shower development and contain a significant fraction of information about hadronic interactions.

I researched possibilities to increase the level of detail of the calculation

method with the aim to study the role of hadronic interactions and short-lived particles in greater detail. By introducing a new matrix form of the coupled hadronic cascade equations, many details of hadronic interactions can be preserved in the calculation. This form makes it convenient to discuss numerical properties, such as stability and stiffness, and helps to identify and eliminate performance bottlenecks, resulting in a dramatical increase in calculation speed without sacrificing precision. The efficiency of this solver opens new perspectives in studying the role of hadronic interactions in atmospheric cascades and allows for investigations of contributing hadron species and the phase-space, relevant for inclusive lepton production. A significant limitation is the precision of interaction models, resulting in large uncertainties in phase-space regions where no accelerator measurements exist. One possibility to study hadronic interactions from the perspective of atmospheric lepton observations is presented that makes use of the new calculation method.

The demand for higher precision of interaction models is also tackled from a microscopical particle physics point of view. I studied and improved the Monte Carlo event generator DPMJET-III by reviewing its performance with respect to an extensive set of experimental data including the LHC. The appearance of a specific curvature in charged-particle multiplicity distributions lead to an investigation about the form of the elastic scattering amplitude, raising questions about the relevance of the black disk limit at LHC energies. The connection between the scattering amplitudes and the underlying partonic picture is studied in the eikonal framework that is an integral part of DPMJET-III and many other minimum-bias event generators.

Although DPMJET-III contains sophisticated physical models, it is technically not well suited for Monte Carlo particle cascade codes, since the generator did not support alternating projectile-target combinations, and because the model was not well studied at high energies, physically and technically. Removing this limitation would reduce uncertainties in particle transport codes dealing with interactions of hadrons and nuclei, such as FLUKA that is actively employed in future high-energy collider development like the upgrades of the LHC and the future circular collider (FCC). In addition, bringing DPMJET-III into air-shower simulators like CORSIKA or astrophysical simulations would enable a better modeling of nuclear effects, on one hand, and on the other hand reduce other uncertainties which arise from the need to combine models spanning distinct energy ranges. In contrast to most competing programs, DPMJET-III is one of the few models that is capable of generating events at energies close to the particle production threshold up to the highest cosmic ray energies.

The improvements of the program at high energies were achieved by modifying the behavior of the hard QCD cross-section, new parton density function, global fits to cross-section data and general re-tuning. The preliminary version has been compared with an extensive set of collider and fixed target data to validate the performance and it has also been used for atmospheric flux calculations.

# Part I

## Atmospheric cascades



# Chapter 2

## Atmospheric cascades

Hadronic interactions of high energy cosmic rays with air nuclei produce extensive cascades of secondary particles. The electromagnetic component of electrons and  $\gamma$ -rays dissipates its energy in form of bremsstrahlung and pair production. In a particle cascade, hadrons can either interact, producing a

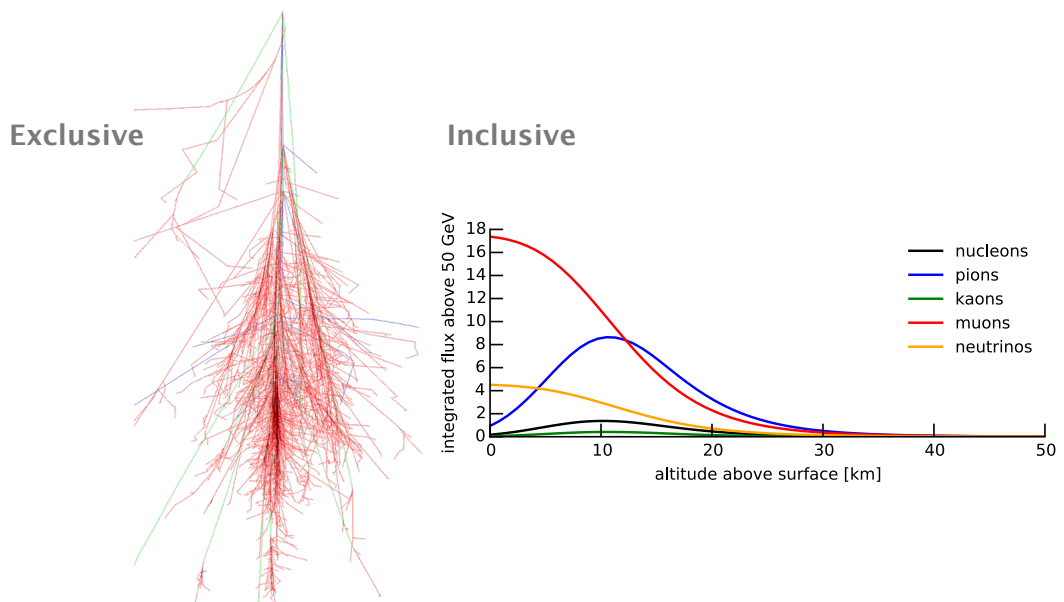


Figure 2.1: Exclusive air-shower calculation from a full Monte Carlo simulation (left) and inclusive fluxes calculated numerically in this work (right).

sub-cascade similar to the original one but at lower energy. Or they can decay into leptons or other hadrons. Since leptons interact very weakly with the atmosphere, they reflect the history of the air-shower development and easily reach down to the surface. The right panel of Figure 2.1 demonstrates this effect by the monotonic increase of the muon and neutrino particle density. In an exclusive calculation, one is interested in modeling realistic final states according to a single realistic initial state. A Monte Carlo program seems to be the most reasonable simulation method, because by using random numbers it can generate an infinite number of shower topologies and also employ

detailed physical models of sub-leading processes, such as multiple scattering. The high degree of realism is on the other hand a drawback of the Monte Carlo calculation, since the history of every particle has to be traced, and there are billions of particles in a high energy particle shower. Due to the requirements on computing time and storage, one has to deal with a limited number of repetitions constraining the achievable precision. Rare processes or subtle signatures might therefore be smeared out by the statistical error.

In cosmic ray experiments, volumetric or planar detectors at the surface measure incoming particles over a certain range of time. Because the atmosphere can not be instrumented, the reconstruction of an exclusive final state from observations is impossible. What is instead possible, is to measure a fraction of the surviving particles at the surface and sometimes the dissipated electromagnetic energy using fluorescence detectors (calorimetry). With the aid of Monte Carlo simulations, the experiments aim to reconstruct from these sparse observations the evolution of the particle shower. The typical goal is to arrive at the initial state, the incoming cosmic ray particle energy and mass.

On the other hand, it is not the ultimate goal of an experiment to reconstruct one shower. The observations are usually integrated over a longer time frame, to derive an inclusive observable, such as the spectrum or the composition of the flux of cosmic rays [40]. In the measurement of the cosmic ray flux, the experiment is integrating over all possible final states and intermediate states to arrive at a distribution of initial states.

In neutrino or muon experiments the goal is often different. When a detector measures a single or a bundle of particles, one typically wants to know what the probability for the creation of this particle in a rare process is (like decay of charmed hadrons), or from which initial cosmic ray energy it might come. These experiments are therefore more interested in the final state by integrating over all initial and intermediate states.

So, depending on what the goal of the cascade calculation one has to choose appropriate methods and combine techniques which result in exclusive or inclusive predictions. In this work the attention lies on the efficient and detailed calculations of inclusive observables by using cascade equations.

## 2.1 Cascade Equations

The flux is defined as the rate of particles per unit area, unit solid angle and time

$$\phi = \frac{dN}{dAd\Omega dt} [\text{cm}^{-2}\text{sr}^{-1}\text{s}^{-1}]. \quad (2.1)$$

Usually we are also interested in the energy spectrum of particles and employ the differential expression

$$\Phi = \frac{d\phi}{dE} = \frac{dN}{dEdAd\Omega dt} [\text{GeV}^{-1}\text{cm}^{-2}\text{sr}^{-1}\text{s}^{-1}]. \quad (2.2)$$

The units cm and GeV are chosen according to conventions in the inclusive lepton community rather than the typical m and TeV of the cosmic ray community.

It is convenient to write the cascade equation in the slant depth variable representing the history of the geometric trajectory  $l$  through the atmosphere

$$X(h_O) = \int_0^{h_O} dl \rho_{air}(l). \quad (2.3)$$

For homogeneous media this equation further simplifies to the simple expression for depth  $X = l\rho$ . In the case of the atmosphere the relation between  $l$  and the slant depth is not so trivial. More details about the Earth's spherical geometry and atmosphere are discussed in section 2.2.2.

With these conventions the transport of hadrons through a medium at high energy is described by the system of coupled cascade integro-differential equations

$$\frac{d\Phi_h(E, X)}{dX} = -\frac{\Phi_h(E, X)}{\lambda_{int,h}(E)} \quad (2.4a)$$

$$-\frac{\Phi_h(E, X)}{\lambda_{dec,h}(E, X)} \quad (2.4b)$$

$$-\frac{\partial}{\partial E}(\mu(E)\Phi_h(E, X)) + \quad (2.4c)$$

$$+\sum_l \int_E^\infty dE_l \frac{dN_{l(E_l) \rightarrow h(E)}}{dE} \frac{\Phi_l(E_l, X)}{\lambda_{int,l}(E_l)} \quad (2.4d)$$

$$+\sum_l \int_E^\infty dE_l \frac{dN_{l(E_l) \rightarrow h(E)}^{dec}}{dE} \frac{\Phi_l(E_l, X)}{\lambda_{dec,l}(E_l, X)}. \quad (2.4e)$$

The index  $h = \pi^+, \pi^-, K^+, \dots$  represents one specific type of particles. The sink terms (2.4a) and (2.4b) model the absorption of particles due to interactions with air nuclei or their loss due to decay into other types of particles. The continuous energy loss term Eq. (2.4c) represents processes such as ionization and radiative losses. For ultra-relativistic particles these losses take values between several MeV/(g/cm<sup>2</sup>) up to a few hundreds MeV/(g/cm<sup>2</sup>). With respect to the energies for which the following calculations are valid ( $> 50$  GeV), the term (2.4c) is at most sub-leading. For the low energy content of very inclined cascades, where particles can traverse up to  $\mathcal{O}(1e5)$  g/cm<sup>2</sup>, the energy loss can not be neglected. Also some processes which involve photons and produce muons in the final state are neglected throughout this work. At very high energies the pair production of muons  $\gamma \rightarrow \mu^+ \mu^-$  contributes to a very small fraction of the flux [83]. Also, a part of the interaction cross section can be attributed to photo-hardronic interactions, in particular electro-magnetic disociation resulting in hadrons in the final state.

The source terms (2.4d) and (2.4e) are responsible for the couplings between the individual cascade equations. The flux of particles  $h$  at a certain depth is either fed by secondaries from interactions of other hadrons or by daughter

products from decays of unstable particles. The lower limit of the integral is motivated by energy conservation, since only those "mother" particles with a  $E \geq E_h$  can contribute.

The absorption rate is expressed as an interaction length

$$\lambda_{int}^h(E) = \frac{\langle m_{air} \rangle}{\sigma_{inel,p-air}(E)}. \quad [\text{g/cm}^2] \quad (2.5)$$

It varies slowly with energy driven by the inelastic (or particle production) cross-section. Its values for different species of hadrons are of the same order of magnitude, as far as measurements exist. In contrast, the decay length

$$\lambda_{dec}^h(E, X) = \frac{c\tau_h E \rho_{air}(X)}{m_h} \quad [\text{g/cm}^2] \quad (2.6)$$

can vary by orders of magnitude. The life-time  $\tau$  is dilated for this ultra-relativistic case, introducing the proportionality to the energy  $E$  in the laboratory frame. Another reason for the variation is due to the value of the particle's life-time itself.

Figure 2.2 draws a clear picture. The dashed line in the log-log plot represents the interaction length and which compared to the other lines is nearly constant. The boost dependence is visible in the linear dependence of  $\lambda_{dec}^h$  on  $E$ . The two lightest charged hadrons,  $\pi^\pm$  and  $K^\pm$ , have similar decay lengths. But for heavy-flavor hadrons, such as  $D$ -mesons or  $\Lambda_C$ -baryons, the life-time is five orders of magnitude smaller compared to that of charged pions. At high energies the short life-time is compensated by the relativistic boost.

The cross-over, where  $\lambda_{int} \approx \lambda_{dec}$ , naturally separates the particle cascade into two regimes, a low-energy or decay dominated and a high-energy, interaction dominated regime. The energy at which this transition occurs is called critical energy [65]

$$\epsilon_p(h_{atm}) = \frac{m_h c^2 h_{atm}}{c\tau_p} \quad (2.7)$$

and takes values of, for example, 115 GeV for  $p = \pi^\pm$ , 850 GeV for  $p = K^\pm$  for a typical scale height of 6.5 km in isothermal planar atmospheres. Charmed mesons typically reach this point at several PeV. Typically this feature is used to construct two limits in which the cascade equations can be solved analytically [65, 95]. As the lower plot in Figure 2.2 demonstrates, the critical energy is not a constant and varies as a function of the density.

In the case of zero particle couplings  $c_{l(E_l) \rightarrow h(E)}$  and  $d_{l(E_l) \rightarrow h(E)}$  and negligible energy loss at high energies, each equation is a homogeneous linear first order differential equation where the solutions have simple exponential forms. The couplings, either due to inelastic hadronic interactions of hadrons with air or due to the decay in hadronic or (semi-)leptonic final states, link the evolution of different species  $h$  and thus increase subsequently the order of the system.

The coefficient of the interaction couplings are expressed as inclusive particle production spectra

$$\frac{dN_{l \rightarrow h}(E_l)}{dE} = \frac{1}{\sigma_{inel,l-Air}(E_l)} \frac{d\sigma_{l \rightarrow h}(E_l)}{dE}. \quad (2.8)$$

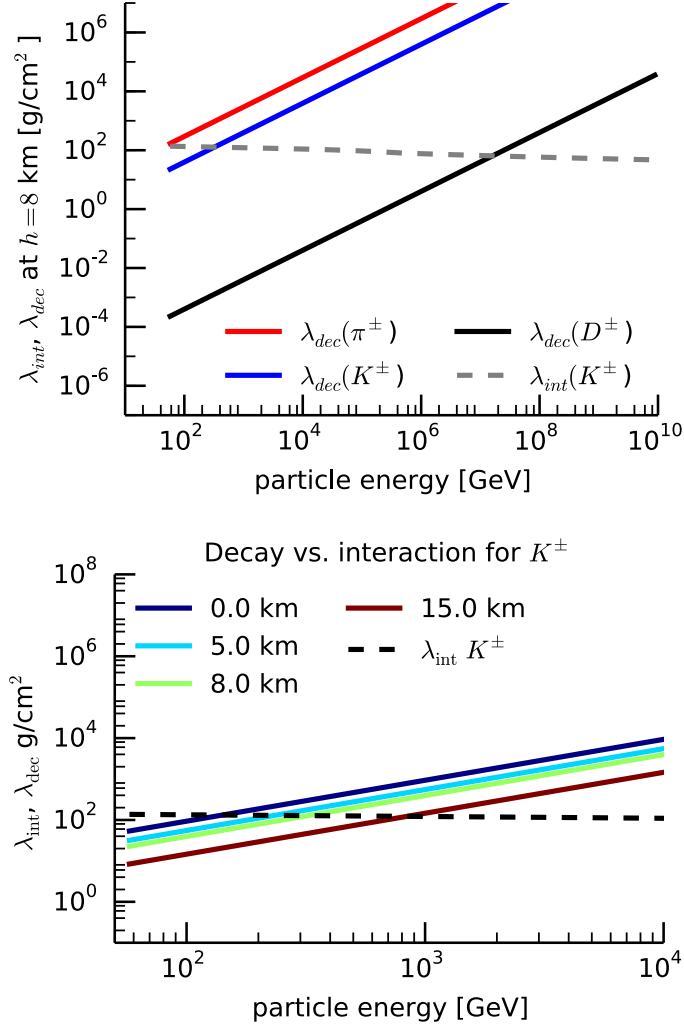


Figure 2.2: (top) Interaction and decay lengths. (bottom) Critical energy for kaons as a function of the altitude for a vertical trajectory.

Decays are expressed in a similar way

$$\frac{dN_{l \rightarrow h}^{dec}(E_l)}{dE} = \sum_i BR_{i,l \rightarrow h} \frac{dN_{i,h}}{dE}. \quad (2.9)$$

$BR_i$  denotes the branching ratio for a decay channel  $i$ . Note that decays are Lorentz invariant and thus do not have explicit energy dependence.

### 2.1.1 Hadron solutions

Let us try to explore the equation and find approximate solutions for fluxes of hadrons, without requiring too much knowledge about the "ingredients" of a detailed calculation.

In the simplest case we ignore geomagnetic and anisotropy effects and assume that the hadronic cascade is initiated at the top of the atmosphere by

isotropically distributed cosmic ray nucleons. A classical parametrization is a power-law source flux, governed by single differential power-law index  $\gamma$  [65]

$$\Phi_{\text{nucleons}} = \Phi_0 E^{-\gamma}, \quad \gamma = 2.7. \quad (2.10)$$

For a while we neglect the contribution of other hadrons and try to derive a solution for protons in air. We restrict ourselves to high energies and neglect the energy loss term and write

$$\frac{d\Phi_p(E, X)}{dX} = -\frac{\Phi_p(E, X)}{\lambda_{int,p}(E)} + \int_E^\infty \frac{\Phi_p(E', X)}{\lambda_{int,p}(E')} \frac{dN_{p \rightarrow p}(E')}{dE'} dE'. \quad (2.11)$$

Since protons are the only particle species, there is just one coupling integral and obviously no decay terms. In analogy to *approximation A* of electromagnetic cascade theory, we assume that the solutions factorize in an  $X$  dependent part and a power-law behavior in  $E$

$$\Phi_p(E, X) = A_p(X) E^{-\gamma}. \quad (2.12)$$

Neglecting the energy dependence of the interaction length, we insert this *ansatz* in (2.11) and divide by  $E^{-\gamma}$

$$\frac{dA_p(X)}{dX} = -\frac{A_p(X)}{\lambda_{p,int}} - \frac{A_p(X)}{\lambda_{p,int}} \int_E^\infty \left(\frac{E'}{E}\right)^{-\gamma} \frac{dN_{p \rightarrow p}(E')}{dE'} dE'. \quad (2.13)$$

Further, we assume that the particle production spectrum (Feynman) scales,

$$E' \frac{dN_{p \rightarrow p}(E')}{dE'} = \frac{dN_{p \rightarrow p}}{dx}, \quad x = \frac{E}{E'} \quad \text{and} \quad 0 < x < 1 \quad (2.14)$$

i.e. it is independent of the interaction energy. Substituting the energy fraction variable  $x$  in (2.13) we obtain

$$\begin{aligned} \frac{dA_p(X)}{dX} &= -\frac{A_p(X)}{\lambda_{p,int}} \left[ 1 - \int_0^1 x^{\gamma-1} \frac{dN_{p \rightarrow p}}{dx} dx \right] \\ &= -\frac{A_p(X)}{\lambda_{p,int}} [1 - Z_{pp}] = -\frac{A(x)}{\Lambda} \end{aligned} \quad (2.15)$$

The factor  $Z_{pp}$  is called the spectrum weighted moment or simply Z-factor,

$$Z_{lh} = \int_0^1 x^{\gamma-1} \frac{dN_{l \rightarrow h}}{dx} dx, \quad (2.16)$$

a neat method to express particle production in a cascade with a single number. The effective attenuation length  $\Lambda$  is the interaction length enhanced by the re-generation fraction, since protons can again produce protons in interactions.

The solution for the proton cascade becomes simply

$$\Phi_p(E, X) = A_p(0) e^{-X/\Lambda_p} E^{-\gamma}, \quad \Lambda_p = \frac{\lambda_{int,p}}{1 - Z_{pp}} \quad (2.17)$$

Rewriting Eq. (2.11) using the new variables and the current assumptions gives

$$\begin{aligned}\frac{d\Phi_p(E, X)}{dX} &= -\frac{\Phi_p(E, X)}{\lambda_{int,p}} + Z_{pp} \frac{\Phi_p(E, X)}{\lambda_{int,p}} \\ &= -\frac{\Phi_p(E, X)}{\lambda_{int,p}} + S(p \rightarrow p, E),\end{aligned}\quad (2.18)$$

where  $S$  is the shortcut notation for the particle production source term.

Let us introduce one additional particle species and look on the influence of the coupling. Using the upper notation the equation for pions in the  $p, \pi$  system writes

$$\begin{aligned}\frac{d\Phi_\pi(E, X)}{dX} &= -\frac{\Phi_\pi(E, X)}{\lambda_{int,\pi}} - \frac{\Phi_\pi(E, X)}{\lambda_{dec,\pi}(E, X)} + \sum_{h=p, \pi} S(h \rightarrow \pi, E) \\ &= -\frac{\Phi_\pi(E, X)}{\lambda_{int,\pi}} - \frac{\Phi_\pi(E, X)}{\lambda_{dec,\pi}(E, X)} + Z_{\pi\pi} \frac{\Phi_\pi(E, X)}{\lambda_{int,\pi}} + Z_{p\pi} \frac{\Phi_p(E, X)}{\lambda_{int,p}}.\end{aligned}\quad (2.19)$$

One can guess that the complications due the couplings become uncomfortable for more than 4-5 charge separated species. Solutions for this form can only be found by introducing additional approximations, such as neglecting the production of protons by pions  $S(\pi \rightarrow p) = 0$ , and by considering the corner cases where either the decay or the interaction term can be neglected. The solution for the pion-proton cascade in the low energy limit, where pion interactions can be neglected is

$$\Phi_\pi^L(E, X) = \frac{Z_{p\pi}}{\lambda_{int,p}} \Phi_p(E, 0) e^{-X/\Lambda_p} E^{-\gamma} \lambda_{dec,\pi}(E, X). \quad (2.20)$$

In the high energy limit where  $\lambda_{int,\pi} \ll \lambda_{dec,\pi}(E, X)$  the decay terms can be neglected and one finds the solution

$$\Phi_\pi^H(E, X) = \frac{Z_{p\pi}}{1 - Z_{pp}} \Phi_p(E, 0) \frac{\Lambda_\pi}{\Lambda_\pi - \Lambda_p} (e^{-X/\Lambda_\pi} - e^{-X/\Lambda_p}). \quad (2.21)$$

The solution for the entire energy range can be obtained by interpolation like

$$\Phi = \frac{\Phi^L \Phi^H}{\Phi^L + \Phi^H}. \quad (2.22)$$

Semi-analytical solutions have been subject of books [65] and detailed publications, such as [95, 44, 93].

### 2.1.2 Decays and lepton production

In analogy to the fluxes of hadrons, we can write down the cascade equation for muons

$$\begin{aligned}\frac{d\Phi_{\mu^\pm}(E, X)}{dX} &= -\frac{\Phi_{\mu^\pm}(E, X)}{\lambda_{dec,\mu}(E, X)} + \sum_h D(h \rightarrow \mu^\pm, E) \\ &= -\frac{\Phi_\mu(E, X)}{\lambda_{dec,\mu}(E, X)} + Z_{\pi^\pm \mu^\pm}^D \frac{\Phi_{\pi^\pm}(E, X)}{\lambda_{dec,\pi}(E, X)} + Z_{K^\pm \mu^\pm}^D \frac{\Phi_{K^\pm}(E, X)}{\lambda_{dec,K}(E, X)} + \dots\end{aligned}\quad (2.23)$$

The muon flux is driven by two source terms, the decays of charged pions and kaons. The decay Z-factors  $Z^D$  have been introduced by P. Lipari in [95] in analogy to particle production

$$Z_{hl}^D = \sum_i BR_i(h \rightarrow l) \int_0^1 x^{\gamma-1} \frac{dN_{i,h \rightarrow l}}{dx} dx. \quad (2.24)$$

as the sum over all contributing branching ratio times the spectrum weighted moment. In a 1D calculation, it is sufficient to use the energy fraction variable

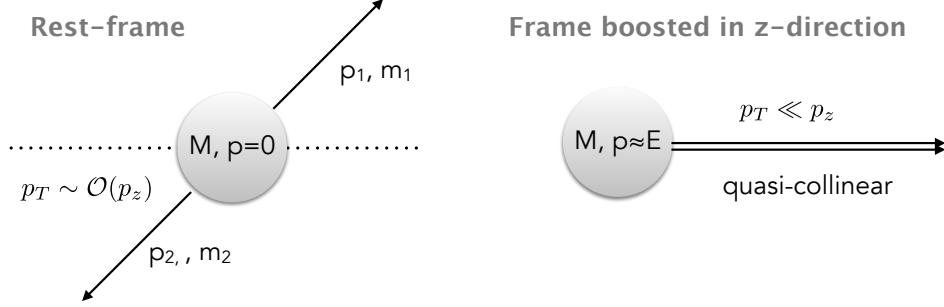


Figure 2.3: Quasi-collinear decays in boosted frame.

x. As illustrated in Figure 2.3 at sufficiently high energy ( $E \gg M$ ) all decay products are moving collinearly to the trajectory of the incoming particle.

The calculation of the decay  $x$ -distribution can be performed analytically for simpler cases, such as for some 2-body decays and 3-body decays, see for example [65, 95, 105]. The other method, which is employed throughout this work, is to use a Monte Carlo program and compute the distributions numerically. This approach takes matrix elements properly into account and one can also easily obtain polarization dependent distributions. The relevant inclusive decay spectra

$$\frac{dn}{dx} = \sum_i BR_i(h \rightarrow l) \frac{dN_{i,h \rightarrow l}}{dx} \quad (2.25)$$

in Figure 2.4 demonstrate how the energy is shared in decays and also the rate at which leptons occur in the final state (compare  $y$ -axis value).

Although the approach is technically straight forward, some special care has to be taken regarding chained decays in the definition what a stable particle is. For example, in the decay channel  $\Gamma_1$ :  $D^*(2010)^+ \rightarrow D^0\pi^+$  [106], is the  $D^0$  a stable particle? It will usually decay immediately, unless the energy is so high that it can survive for hundreds of meters in air and becomes attenuated by interactions. In the end, the choice depends on the goal, level of detail and energy range of the calculation and it is just pointed out here that the values of  $Z$  and  $Z^D$  are not universal and depend on what one considers as a short life-time. The convention in cosmic ray physics is to declare all particles with a proper life-time longer than  $c\tau_{K_S^0} = 2.68$  cm as the mother mesons of conventional atmospheric leptons, and the rest as the origin of prompt leptons.

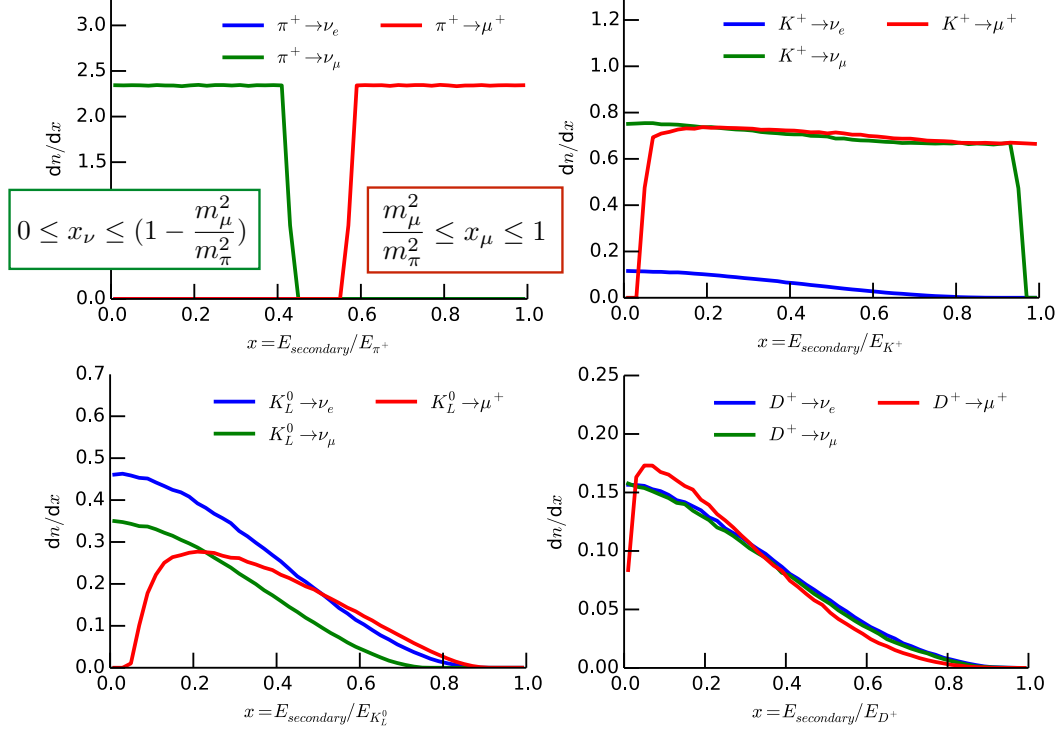


Figure 2.4: Examples of inclusive decay spectra, calculated from PYTHIA 8 Monte Carlo [128] and the tool PYTHIADECAYS (see A.5).

Table 2.1: Dominant production channels of atmospheric leptons [106]

conventional decays	branching ratio	prompt decays	branching ratio
$\mu^- \rightarrow e^- \bar{\nu}_e \nu_\mu$	100 %	$D^+ \rightarrow \bar{K}^0 \mu^+ \nu_\mu$	9.2 %
$\pi^+ \rightarrow \mu^+ \nu_\mu$	99.99 %	$D^0 \rightarrow K^- \mu^+ \nu_\mu$	3.3 %
$K^+ \rightarrow \mu^+ \nu_\mu$	63.55 %	$D_s^+ \rightarrow \tau^+ \nu_\tau$	5.55 %
$K_{e3}^0: K_L^0 \rightarrow \pi^\pm e^\mp \nu_e$	40.55 %	$\tau^- \rightarrow \mu^- \bar{\nu}_\mu \nu_\tau$	17.41 %
$K_{\mu 3}^0: K_L^0 \rightarrow \pi^\pm \mu^\mp \nu_\mu$	27.04 %	$\tau^- \rightarrow e^- \bar{\nu}_e \nu_\tau$	17.83 %
$K_{e3}^+: K^+ \rightarrow \pi^0 e^+ \nu_e$	5.07 %	$\eta \rightarrow \mu^+ \mu^- \gamma$	$3.1 \times 10^{-4}$
$K_{\mu 3}^+: K^+ \rightarrow \pi^0 \mu^+ \nu_\mu$	3.35 %		

For completeness the dominant production processes are listed in Table 2.1. The left table lists the channels of so called conventional leptons. Their mother particles live long enough to travel through the air for a while before they decay. The right table lists the leptonic decay channels of very short lived mesons. As it will be discussed in section 5.2 the competition between their production cross-section, small branching ratios and atmospheric absorption can make rare particles the dominant source.

## 2.2 Increasing the level of detail

The previous section explored the cascade equations in a basic way to arrive at some analytic understanding of the basic physics. When discussing

the hadronic cascade in section 2.1.1 it should have become clear, that semi-analytical solutions can only be obtained by doing numerous approximations. The goal of this chapter is to study the "ingredients" of a realistic calculation on a deeper level. The goal of the following sections is to provide a more detailed view on the flux of cosmic rays, the atmosphere, the geometry and finally on hadronic interactions.

### 2.2.1 The flux of cosmic rays

#### Measurements

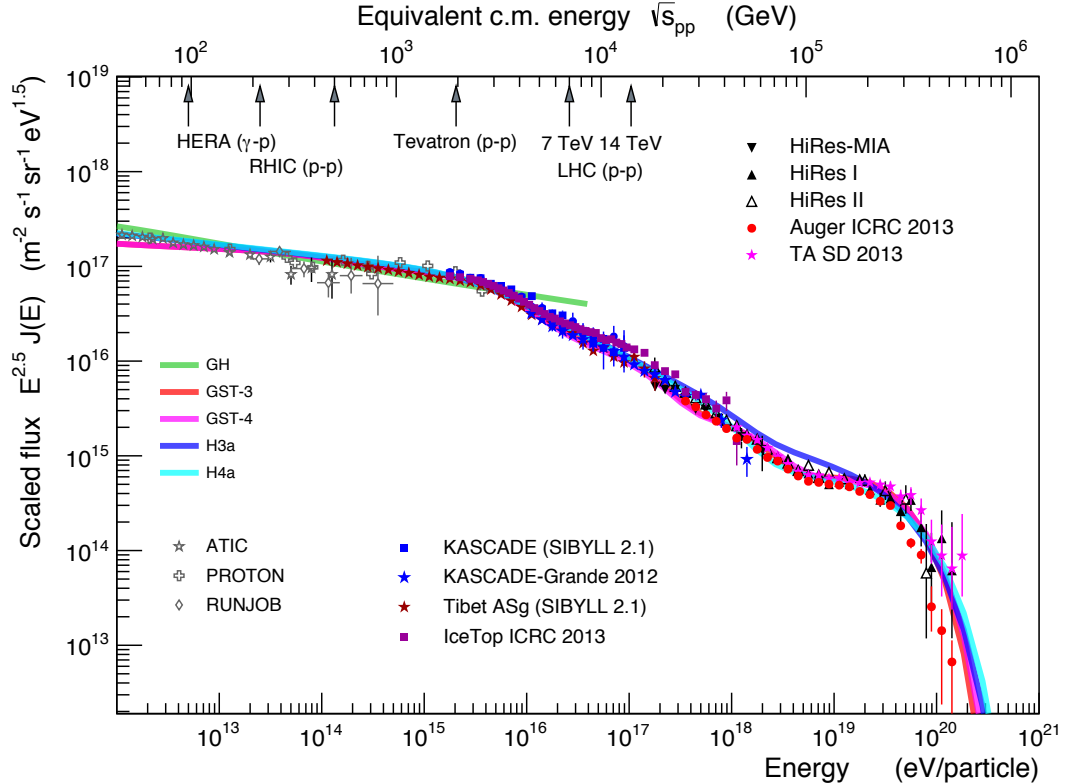


Figure 2.5: All particle spectrum as measured by ground based arrays. The data points are compiled according to the summary plot (28.8) in [106]. The lines represent are obtained from parameterizations given in the text. Figure by R. Engel.

The observed primary cosmic-ray flux covers a particle energy range from below  $10^9$  eV up to several  $10^{20}$  eV. In order to perform measurements over 12 orders of magnitude in energy, a variety of different detection methods is used. Below  $\sim 100$  TeV particle energy, air-borne and satellite experiments such as AMS [22], PAMELA [15], ATIC-2 [109], CREAM [20, 21] and TRACER [31], directly measure particle energy and mass. Above  $\sim 100$  TeV, the cosmic-ray flux becomes too small and must be detected indirectly by large ground-based air-shower arrays, either by detecting secondary particles at ground or by measuring fluorescence light in air or combinations of both. The fact that

primary particles can only be observed indirectly by detecting portions of the induced air-shower makes it more difficult to measure the exact properties of the primary cosmic-ray spectrum. A number of very large surface arrays have been built to observe cosmic-rays up to about  $10^{20}$  eV.

The direct measurements provide the most unbiased results on cosmic-ray spectrum and composition, and great progress was made the past years. In particular, recent observations by CREAM [21] show an overall harder helium spectrum as compared to protons and, mainly, a flattening of their spectral index at about 230 GeV/nucleon. This result was confirmed by PAMELA [15] and it is consistent with the latest AMS results [17]. This flattening of the cosmic-ray spectrum could be an effect of particle propagation through the Galaxy or of acceleration in their sources.

The indirect measurements have provided the observation of cosmic-ray spectrum at the knee region (which is at about  $3 \times 10^{15}$  eV, where it steepens from  $\sim E^{-2.7}$  to  $\sim E^{-3}$ ) and up to the highest energies. Measurements by KASCADE-Grande [26] indicated that at energies of the knee the composition becomes heavier, in general agreement with the notion of rigidity-dependence. The highest energy cosmic-rays above the so-called ankle at  $3 \times 10^{18}$  eV are expected to be of extragalactic origin due to the high level of isotropy, which would not be present for Galactic sources. There is an ongoing dispute regarding the composition of the cosmic ray flux at ultra-high energies. The measurements of the Pierre Auger observatory support a heavy composition while the Telescope Array excludes a heavy composition [10, 1]. The inconsistency between these two observations stems presumably from inaccuracies of hadronic interaction models and we can hope that improved models and more sophisticated data analysis methods will resolve this discrepancy in near future.

### Flux parameterizations

In order to have a good description of the expected atmospheric lepton flux arising from cosmic-ray interactions in the Earth's atmosphere, a careful parametrization of the cosmic-ray composition is necessary. The typical picture for cosmic-ray acceleration is based on the idea by B. Peters [110], where each source class can only accelerate up to a maximum rigidity. Each mass group can reach a maximum energy, after which its population quickly drop. Several current models are assembled as a series of "Peters cycles", broken power-laws with rigidity dependent cutoff.

$$\phi_m(E) = \sum_j a_{m,j} E^{-\gamma_{m,j}} \times \exp\left[-\frac{E}{Z_m R_{c,j}}\right] \quad (2.26)$$

In this equation  $m$  represents the element or the mass group such as H, Fe or CNO. The model can be built up of several classes of accelerators  $j$  (generations), represented by different maximum characteristic rigidities  $R_c$  up to which they can accelerate. The normalization  $a$  and the spectral index  $\gamma$  de-

pend on many details of the acceleration process, the density of (potential) sources etc., but they can also be obtained from fits to data.

In this work three models are of particular interest. The model H3a in [66] is based on ideas by M. Hillas. The knee and ankle are the consequence of three components, a galactic component A (Super-Nova remnants), another galactic component B (presumably young pulsars) and an extragalactic component C (presumably AGNs). In this model the parameters are adjusted to CREAM data at lower energies and to the majority of high energy observations. A second alternative version H4a contains only protons in the extragalactic component C. The model considers five mass groups (H, He, CNO, Mg-Si, Fe).

The other model GST-3 and GST-4 [69] is based on the same ideas, but attempts to reproduce more features of the indirect measurements, such as the "second knee" in KASCADE-Grande and IceTop data. The parameter values are determined in a fit rather than by adjustment. GST-4 is an alternative version with four generations and a purely protonic composition above the knee.

The last model is an older parameterization [67], which we call GH. This model has been derived mostly from balloon measurements and tries to describe the data up to several tens of TeV, without aiming to model the higher energy features knee and ankle.

Other models, such as poly-gonato [82] or Zatsepin-Sokolskaya [142] exist, and can be used with the following calculation methods. But either they are incompatible with newest observations or do not model the high energy features which we are interested in. In a previous publication [62] the attempt was made to merge the H3a at high-energy and the GH model at energies below 1 TeV.

The resulting all-particle spectra predicted by the various models are superimposed on air shower data in Fig. 2.5.

### 2.2.2 Geometry and atmosphere

Using school-level geometry one should arrive to the following expressions for the total path length and the height above the surface at each point of the trajectory (see left panel of Figure 2.6)

$$l(\theta) = \sqrt{R_{\text{top}}^2 - A_2(\theta)^2} - A_1(\theta) \quad (2.27\text{a})$$

$$h_{\text{atm}}(\Delta l) = \sqrt{A_2(\theta)^2 + (A_1(\theta) + l(\theta) - \Delta l)^2} - R_E. \quad (2.27\text{b})$$

The only free variables are the height of the observation level  $h_{\text{obs}}$  and the zenith angle at the detector  $\theta$ . With the two relations above the slant depth in Eq. (2.3) can be calculated as a function of the atmospheric density.

A traditional way to approximate the relation between depth and density is to approximate the Earth as plane surface. The isothermal atmospheric density can then be modeled by a single exponential with an effective scale

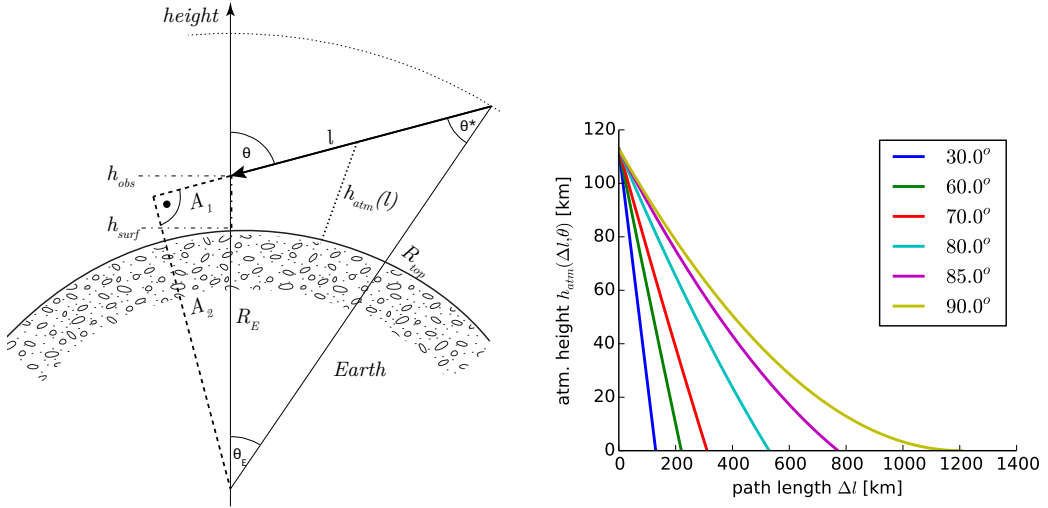


Figure 2.6: One-dimensional shower trajectory in the curved geometry of the Earth.

height  $h_0$  [65].

$$X(\theta) = \frac{\rho(h_0)h_0}{\cos \theta} \quad (2.28)$$

This approximation typically holds up to zenith angles of  $60^\circ$ , or where the dependence of the atmospheric height on the path length becomes not linear (Figure 2.6 right), and fails above that because  $\cos\theta$  produces a divergent behavior.

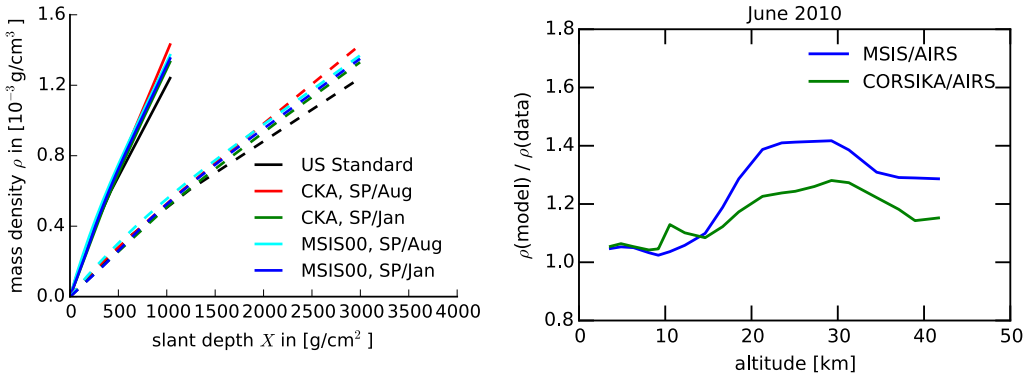


Figure 2.7: (left) Atmospheric density dependence on  $X$ , calculated using parameterizations for the US Standard Atmosphere [129] and the South Pole as implemented in CORSIKA [78], and the NRLMSISE-00 model. Solid lines represent a trajectory for  $\theta = 0^\circ$  and dashed for  $\theta = 70^\circ$ . (right) Comparison between CORSIKA parameterization, NRLMSISE-00 and AQUA/AIRS satellite data at the South Pole.

But first of all, the atmosphere is not isothermal, contains layers and is subject to daily and seasonal variations. An often used approach, based on the idea by Linsley [79], is a parametrization of the relation between height and mass overburden  $X_v(h)$  (slant depth for vertical trajectory) using 5 piecewise

defined exponential functions, representing layers of the atmosphere. A higher flexibility is achieved if tabulated atmospheric data (e.g. from AQUA/AIRS<sup>1</sup> satellite) or detailed numerical models, such as NRLMSISE-00 [113], are used. On the right hand side of Figure 2.7 the possible quantitative sources are compared at the South Pole, which is an extreme case in terms of climate conditions, so the differences can be smaller than the 20-30% somewhere else.

The most flexible way to deal with an arbitrary density profiles is to compute and tabulate the relation  $\rho(X)$ , by integrating numerically on a grid of locations on the path  $l_i$

$$X_i(\theta) = \int_0^{l_i} dl' \rho(h_{\text{atm}}(l', \theta)), \quad (2.29)$$

recording the value of  $\rho$  at each grid point  $i$ . Since the relation  $\rho(X)$  is approximately linear, a smooth interpolating spline can be found easily. Each model and zenith angle are so represented by a set of interpolation coefficients which reflect all subtle differences between the models as demonstrated in Fig. 2.7.

## 2.3 Hadronic interactions

In typical semi-analytical solutions of the atmospheric lepton problem [65, 95], the scaling argument is used to derive energy independent couplings factors, the spectrum weighted moments or  $Z$ -factors (see section 2.1.1). This approach works for power-law cosmic ray spectra in the case where the solutions factorize  $\Phi_l(E_l, X) = A_l(X)E_l^{-\gamma}$  and the interaction length is independent of energy  $\lambda_{\text{int},l}(E_l) \approx \lambda_{\text{int},l}$ . The Figures 2.2 and 2.5 clearly show that both approximations do not hold in the entire energy range.

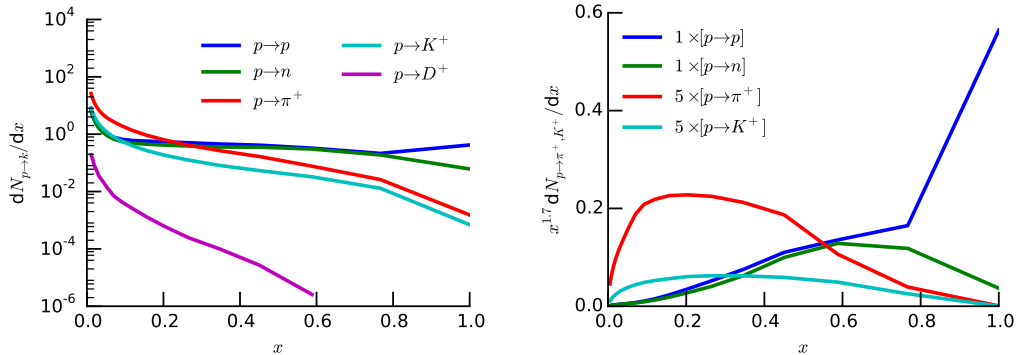


Figure 2.8: (left) Particle production spectra in proton-air interactions obtained with SIBYLL 2.3 (right) Integrand of the Z-factor expression for  $\gamma = 2.7$ .

Figure 2.8 contains particle production spectra in the scaling variable  $x$ . Feynman scaling means that the shape of the particle distribution in the variable Feynman  $x_F = \frac{p_{\parallel}}{\sqrt{s}}$  is independent of the interaction energy. Qualitatively

---

<sup>1</sup><http://disc.sci.gsfc.nasa.gov/AIRS>

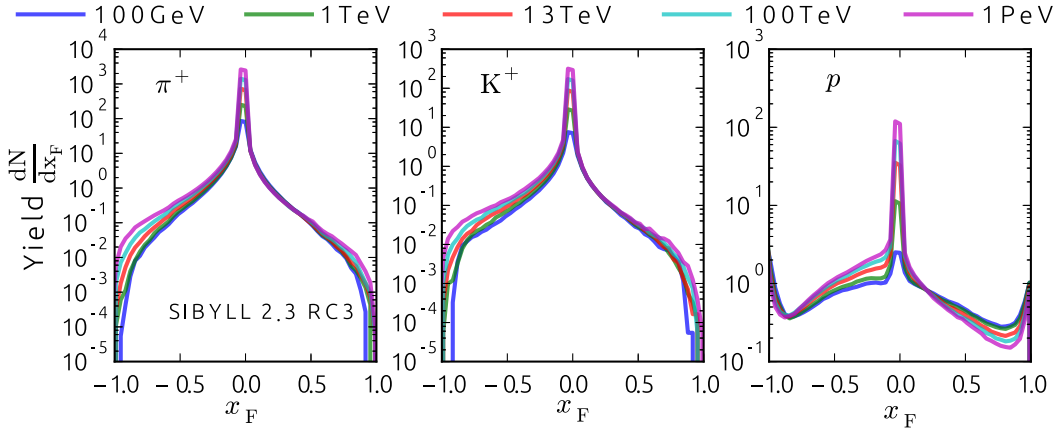


Figure 2.9: Feynman scaling of inclusive particle spectra in SIBYLL 2.3 RC3 in proton-air interactions. Figure by F. Riehn.

there is a significant difference between secondary baryons and mesons. The proton and neutron line are flat for a large fraction of  $x$  values. For inclusive  $p \rightarrow p$  processes the very forward part  $x > 0.8$  is enhanced compared to  $p \rightarrow n$ . This effect is called leading particle effect and it can be microscopically attributed to single diffractive processes where the projectile proton stays intact but one or several nucleons on the target side disintegrate. Also low-mass diffraction processes of the kind  $N + A \rightarrow N^* \rightarrow N + \pi$  contribute in the high  $x$  domains.

The meson spectra are much steeper in case of baryon projectiles. Mesons can be created during fragmentation or in low mass excitations as mentioned above. But since the projectile carries the baryon number "at high momentum", the projectile fragmentation region  $x \gtrsim 0.3$  will be populated mostly by baryons.

In meson-baryon interactions the picture is inverted. The leading particle becomes a meson, preferably with the same valence quark flavor content.

On the right hand side of Figure 2.8 the integrand of the spectrum weighted moments  $Z_{pp}$ ,  $Z_{p\pi^+}$  etc. (see Eq. 2.16) are shown. The convolution with the power-law "beam" spectrum amplifies the forward part of the production distribution. The relatively small difference between  $p$  and  $n$  becomes very very enhanced.

Considering the relevant particle production phase-space in  $x$ , we can already say at this point, that the highest contribution to the meson  $Z_{pM}$ -factors comes from  $0.2 < x < 0.6$ , while for baryons the more forward range  $x > 0.5$  is more important.

So, does Feynman scaling hold? Figure 2.9, where particle production spectra are generated with the hadronic interaction model SIBYLL 2.3 RC3 [64, 19, 117], shows that pion and kaon spectra show approximate scaling at mid  $x_F$ , i.e. indeed a universal form of the forward spectrum. In the central region  $x_F < 0.1$ , the increasing number of multiple parton interactions enhances pair-production and violates scaling. At forward large  $x_F$ , scaling is

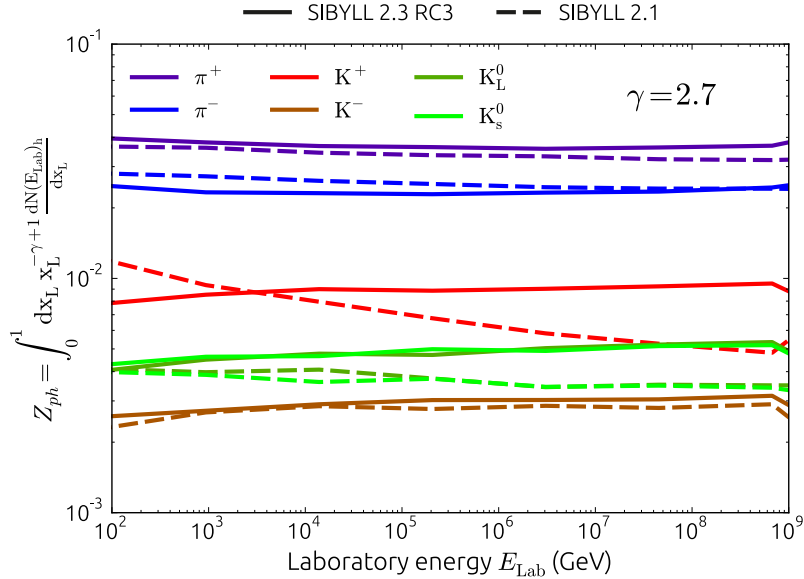


Figure 2.10: Spectrum-weighted moments for SIBYLL 2.1 and SIBYLL 2.3 RC3.

violated for most particles in SIBYLL 2.3 RC3 since they are associated with the fragmentation of the projectile remnant. Proton spectra are not expected to perfectly scale, since they can undergo additional processes, like diffraction, as a part of the projectile.

With the aim to include these effects in the analytical calculations, a more general approach has been pioneered by the authors of [138]. The energy dependent  $Z$ -factor

$$Z_{lh}(E) = \int_E^\infty dE' \left(\frac{E'}{E}\right)^{\gamma(E)-1} \frac{\lambda_{\text{int},l}(E)}{\lambda_{\text{int},l}(E')} \frac{dN_{l \rightarrow h}(E')}{dE}, \quad (2.30)$$

needs only the approximation that the solutions factorize, but it can add three more details:

- the spectral index variation of the cosmic ray flux,
- the growth of the inelastic cross-section and
- the non-scaling behavior of particle production.

Although the method increases the precision of the cascade calculation, one has to face the question how to model the interactions and possible scaling violations. Obviously, since there are no measurements with sufficient  $x_F$  coverage at energies beyond fixed-target experiments, we have to use models. The growth of the inelastic cross-section was incorporated into the  $Z$ -factor expression earlier by [140].

The highest detail is reproduced by Monte Carlo codes, such as DPMJET (see chapter 7), SIBYLL [64, 19, 117], EPOS [114] and QGSJET [108]. Figure 2.10 shows the predictions of the energy dependent  $Z$ -factors for a fixed cosmic ray spectral index  $\gamma = 2.7$ , the older SIBYLL 2.1 and the newest version.

While  $Z_{p\pi}$  is approximately constant as we would expect from Figure 2.9, the kaon moments slightly grow. This effect is motivated by the non-perturbative phenomenon of associated production, where a  $s\bar{s}$  quark pair is raised from the sea and recombines with the projectile valences. The  $s$ -quark forms together with a di-quark from the proton and becomes a  $\Lambda$  baryon, while the  $\bar{s}$  forms with the other quark a  $K^+$ . Although the exact microscopic mechanism is still under discussion, there is evidence from data that the charge ratio of kaons increases towards higher  $x_F$  [135]. The big difference between the 2.1 and the 2.3 versions in kaon production stems from a unphysical feature of the old program, where significantly more kaons were produced in nuclear interactions when compared with the nucleon-nucleon case. This feature is removed from the successor versions.

More details about the specifics of Monte Carlo codes for cosmic ray shower simulations and interactions at very high energy are outlined in sections 7.2. A study about how the models performed for inclusive leptons before LHC data became available, can be found in [62].



# Chapter 3

## Matrix form of the coupled cascade equations

The previous chapter outlined the basic properties of the cascade equations and traditional approaches for finding semi-analytical solutions. Couplings between particle species during the transport through the medium increase the complexity of the equation system and prevent from finding closed solutions for the flux of secondaries. Several assumptions about the form of the primary spectrum, scaling arguments and re-interactions lead to a decoupling of the evolution equations for individual hadron fluxes. Although it is possible to compensate for some of the caveats by using energy-dependent Z-factors, the error due to the remaining approximations is in the order of 5-15% as we have found out from comparisons with Monte Carlo calculations in one of our previous publications [62].

Another, more sophisticated way, to tackle the problem of coupled cascade equations is to solve them numerically. In the past, several successful attempts have been undertaken resulting in basically two methods. One method employs a recursive scheme to solve the equations similarly to the decoupled method [140, 45, 93]. There, the initial iteration leads to a first order approximation of pion and kaon fluxes, neglecting mutual production. Using this first solution driven by just the nucleon flux, cross-talk between the channels is added in additional iterations. Although the scheme yields precise results the computational time for one set of settings takes several days <sup>2</sup>.

The second method is the direct solution of the cascade equations by numerical integration of integro-differential equations. In [42] and the follow up studies [56, 37] the integration is performed directly on discrete grids. The authors follow the goal to calculate air-shower observables, such as  $X_{\max}$  or energy deposit of both, the hadronic and electromagnetic components. Their approach is aimed to save computational time when compared to or integrated with full Monte Carlo and hybrid calculations. The lack of computing power of the older publications focused the particle physics related part of the work on the reduction of statistical errors when obtaining particle spectra from the

---

<sup>2</sup>Personal communication with S. Sinegovsky

slow NEXUS model. Also, the authors restricted themselves on a relatively narrow energy band between 100 GeV and 10 PeV cosmic ray energy. In the more recent papers a full description of the cascade's electromagnetic part was added, the energy range extended and the code published as the CONEX program, a part of the hybrid Monte Carlo scheme in the air-shower simulator CORSIKA [79].

Although the CONEX scheme is quite sophisticated, it fails in certain tasks like

- including short-lived particles and calculations of prompt lepton spectra,
- studies of all possible species of hadrons, not just the most abundant ones,
- studies of couplings and numerical stability
- an open, structured and extensible distribution as modern computer application

The first item above is the most restrictive one (read about the implications in section 3.2). Other points, which are subject of the present work would have been technically possible with CONEX, but have never been carried out, such as inclusive lepton flux calculations.

In the following section a new calculation scheme will be formulated with the aim to overcome the limitations of CONEX and employ it for advanced studies of interaction models.

### 3.1 Derivation of the matrix notation

Starting from the system of coupled cascade equations (Eq. (2.4) reprinted for convenience)

$$\begin{aligned} \frac{d\Phi_h(E, X)}{dX} = & -\frac{\Phi_h(E, X)}{\lambda_{int,h}(E)} \\ & -\frac{\Phi_h(E, X)}{\lambda_{dec,h}(E, X)} \\ & + \sum_l \int_E^\infty dE_l \frac{dN_{l(E_l) \rightarrow h(E)}}{dE} \frac{\Phi_l(E_l, X)}{\lambda_{int,l}(E_l)} \\ & + \sum_l \int_E^\infty dE_l \frac{dN_{l(E_l) \rightarrow h(E)}^{dec}}{dE} \frac{\Phi_l(E_l, X)}{\lambda_{dec,l}(E_l, X)}. \end{aligned} \quad (3.1)$$

we discretize the energy dependence on a logarithmic grid

$$E_i = E_0 \times 10^{di}, \quad (3.2)$$

where  $d$  is chosen accordingly to get 8-9 bins per decade of energy. Making the transition  $dE \rightarrow \Delta E$ , the cascade equation for one energy bin and one particle

species  $h$  becomes

$$\begin{aligned} \frac{d\Phi_{E_i}^h}{dX} = & -\frac{\Phi_{E_i}^h}{\lambda_{int,E_i}^h} + \sum_{E_k \geq E_i}^{E_N} \sum_l \frac{c_{l(E_k) \rightarrow h(E_i)}}{\lambda_{int,E_k}^l} \Phi_{E_k}^l \\ & - \frac{\Phi_{E_i}^h}{\lambda_{dec,E_i}^h(X)} + \sum_{E_k \geq E_i}^{E_N} \sum_l \frac{d_{l(E_k) \rightarrow h(E_i)}}{\lambda_{dec,E_k}^l(X)} \Phi_{E_k}^l. \end{aligned} \quad (3.3)$$

If the flux (or state) vector is defined as

$$\vec{\Phi} = \left( \vec{\Phi}^p \quad \vec{\Phi}^n \quad \vec{\Phi}^{\pi^+} \quad \dots \quad \vec{\Phi}^{\bar{\nu}_\mu} \quad \dots \right)^T, \quad (3.4)$$

where each of the inserted vectors contains the scalar fluxes for each energy bin

$$\vec{\Phi}^p = (\Phi_{E_0}^p \quad \Phi_{E_1}^p \quad \dots \quad \Phi_{E_N}^p)^T. \quad (3.5)$$

The coupling coefficients absorb the energy bin width and the inclusive spectra distributions from Eq. (2.8) and (2.9) evaluated at the secondary energy

$$c_{l(E_l) \rightarrow h(E_h)} = \Delta E_l \frac{dN_{l \rightarrow h}(E_l)}{dE_h}(E_h) \quad (3.6)$$

and

$$d_{l(E_l) \rightarrow h(E_h)} = \Delta E_l \frac{dN_{l \rightarrow h}^{dec}(E_l)}{dE_h}(E_h). \quad (3.7)$$

The production of particle  $h$  with laboratory energy  $E_h$  by interactions (or decays) of a hadron  $l$  with laboratory energy  $E_l$  is parameterized by a single scalar coefficient. The interaction lengths  $\lambda_{int}$  are arranged in diagonal "rate" matrices according to the order in Eq. (3.4)

$$\Lambda_{int} = \text{diag} \left( \frac{1}{\lambda_{int,E_0}^p} \quad \dots \quad \frac{1}{\lambda_{int,E_N}^p}, \quad \frac{1}{\lambda_{int,E_0}^n}, \quad \dots, \quad \frac{1}{\lambda_{int,E_N}^n}, \right. \\ \left. \frac{1}{\lambda_{int,E_0}^{\pi^+}}, \quad \dots, \quad \frac{1}{\lambda_{int,E_i}^{\bar{\nu}_\mu}} \dots \right). \quad (3.8)$$

When packing the decay lengths we factorize out the density  $\lambda_{dec} = \rho(X)\tilde{\lambda}_{dec}$

$$\Lambda_{dec} = \text{diag} \left( \frac{1}{\tilde{\lambda}_{dec,E_0}^p} \quad \dots \quad \frac{1}{\tilde{\lambda}_{dec,E_N}^p}, \quad \frac{1}{\tilde{\lambda}_{dec,E_0}^n}, \quad \dots, \quad \frac{1}{\tilde{\lambda}_{dec,E_N}^n}, \right. \\ \left. \frac{1}{\tilde{\lambda}_{dec,E_0}^{\pi^+}}, \quad \dots, \quad \frac{1}{\tilde{\lambda}_{dec,E_i}^{\bar{\nu}_\mu}} \dots \right). \quad (3.9)$$

By evaluating the structure of the double-sum in Eq. (3.1) the coupling (sub-) matrix for production of  $h$  in interactions of  $l$  is

$$C_{l \rightarrow h} = \begin{pmatrix} c_{l(E_0) \rightarrow h(E_0)} & \dots & c_{l(E_0) \rightarrow h(E_N)} \\ & \ddots & c_{l(E_1) \rightarrow h(E_N)} \\ 0 & & \vdots \\ & & c_{l(E_N) \rightarrow h(E_N)} \end{pmatrix} \quad (3.10)$$

and equivalently in case of decay

$$\mathbf{D}_{l \rightarrow h} = \begin{pmatrix} d_{l(E_0) \rightarrow h(E_0)} & \cdots & d_{l(E_0) \rightarrow h(E_N)} \\ & \ddots & d_{l(E_1) \rightarrow h(E_N)} \\ 0 & & \vdots \\ & & d_{l(E_N) \rightarrow h(E_N)} \end{pmatrix}. \quad (3.11)$$

The upper-triangular form is due to energy conservation  $E_l \geq E_h$ . In this approach the number of primary energy bins is equal to the number of secondary energy bins, yielding square matrices. In the last step, we assemble the full coupling matrix  $\mathbf{C}$  (and  $\mathbf{D}$ , respectively)

$$\mathbf{C} = \begin{pmatrix} C_{p \rightarrow p} & C_{n \rightarrow p} & C_{\pi^+ \rightarrow p} & \cdots \\ C_{p \rightarrow n} & C_{n \rightarrow n} & C_{\pi^+ \rightarrow n} & \cdots \\ C_{p \rightarrow \pi^+} & C_{n \rightarrow \pi^+} & C_{\pi^+ \rightarrow \pi^+} & \cdots \\ \vdots & \vdots & \vdots & \ddots \end{pmatrix}. \quad (3.12)$$

By putting everything together we arrive at the matrix notation

$$\frac{d}{dX} \vec{\Phi} = \left[ (-\mathbf{1} + \mathbf{C}) \boldsymbol{\Lambda}_{int} + \frac{1}{\rho(X)} (-\mathbf{1} + \mathbf{D}) \boldsymbol{\Lambda}_{dec} \right] \vec{\Phi}. \quad (3.13)$$

One might notice the analogy to the space state representation  $x' = \mathbf{A}x$  of control-theory in electrical engineering [97, 98].

### Implications of the matrix notation

Although the notion of seeing the couplings between cascade equations as matrix elements is present in the literature [140, 65, 95, 42] nobody wrote the equation in this form, yet. In my opinion, the advantage of the form (3.13) is that it facilitates seeing the discretized equation system as what it is - a system of ordinary differential equations of order ( $N_{E\text{-bins}} \times N_{\text{particlespecies}}$ ) with non-constant coefficients. The "integro-" part is solved implicitly when integrating over the single variable  $X$ . The algebraic equation itself is of order one. In a homogeneous medium with constant density the equation is linear and the solution is simply

$$\vec{\Phi}(X) = e^{[(-\mathbf{1} + \mathbf{C}) \boldsymbol{\Lambda}_{int} + \frac{1}{\rho} (-\mathbf{1} + \mathbf{D}) \boldsymbol{\Lambda}_{dec}] X} \vec{\Phi}_0, \quad (3.14)$$

where  $\vec{\Phi}_0$  is the initial condition and the  $e$  the matrix exponential function. In air the density is not constant, which influences the linearity of the equation system. But since the value of the derivative can be computed at any depth  $X$  the equation Eq. (3.13) must be suitable for iterative numerical solutions.

Another aspect is the pattern of non-zero couplings in the matrices. As illustrated in Figure 3.1 the contributing production and decay channels can be directly read from visualizations of the matrices. The look at the pattern also immediately reveals that **coupled cascade equations are a sparse problem**, since the number of non-zero elements is very small.

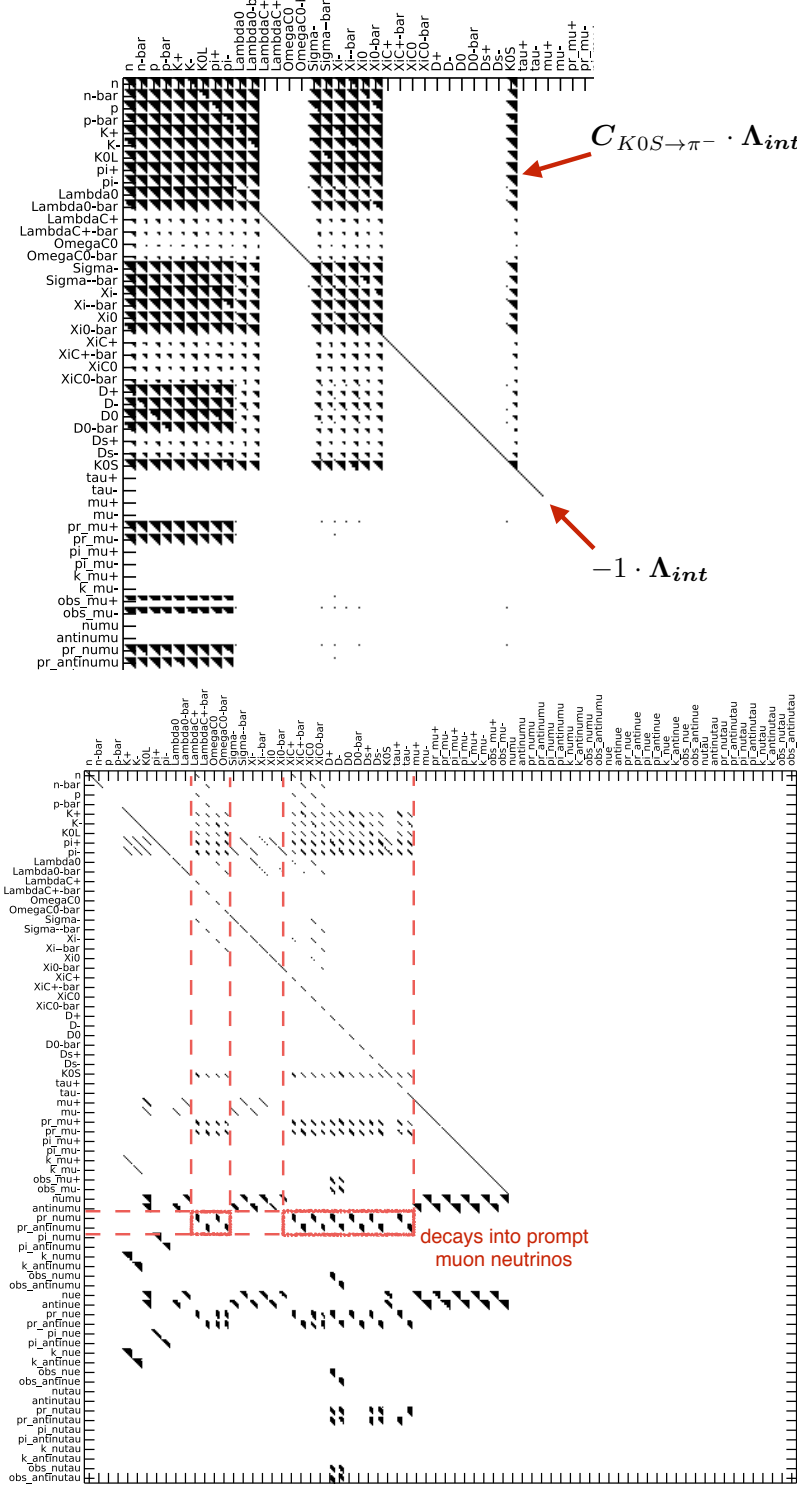


Figure 3.1: Pattern of the interaction (top) and decay (bottom) matrix. Each pixel represents a non-zero element. The view in the interaction matrix is cropped on the region containing most of the non-zero part.

Other terms, such as energy loss, can be added to the equation while keeping its general form, for example

$$\frac{d}{dX} \vec{\Phi} = \left[ (-\mathbf{1} + \mathbf{C})\Lambda_{int} + \frac{1}{\rho(X)}(-\mathbf{1} + \mathbf{D})\Lambda_{dec} \right] \mathbf{L} \vec{\Phi}. \quad (3.15)$$

with  $\mathbf{L}$  being a banded matrix with negative diagonal elements (losses) and positive off-diagonal elements representing the increase of fluxes in lower-energy bins.

But the biggest advantage of this form is the possibility to employ the machinery of numerical linear algebra to study stability. Why this is important will be discussed in the next section.

## 3.2 Eigenmodes, stiffness and stability

Since we have an order-one ordinary matrix differential equation, we expect the solution for  $\vec{\Phi}$  to be of the form

$$\vec{\Phi} = \sum_{i=1}^n c_i e^{\lambda_i^* X} \vec{\Psi}_i, \quad (3.16)$$

with complex constants  $c$ ,  $\lambda^*$  the eigenvalues and  $\vec{\Psi}$  the eigenvectors of the matrix. By studying the eigenvalues, we can determine if the system is stable, i.e. contains no divergent processes, and it will attenuate to a stable final state when starting from an arbitrary initial condition  $\vec{\Phi}_0$ .

What we expect regarding the physics for  $X \rightarrow \infty$  is that since no additional energy is added to the system, the interaction and decay processes will convert all interacting and unstable particles into stable species, in this case neutrinos. We also don't expect semi-stable oscillating modes, because decay and interaction (except elastic scattering) are  $1 \rightarrow$  many processes leading to conversions of higher energetic objects into several lower energetic objects. Following these arguments, the dynamical system will be asymptotically (Lyapunov) stable and the eigenvalues will be real and negative. Another question relates to the magnitude of the eigenvalues. We have in principle just two competing processes, but since the life-time of many particle species can vary by a lot, the decay modes will spread over many orders of magnitude.

The distribution of eigenvalues in Figure 3.2 clearly confirms the expectations from the physics point of view, the real parts are negative and spans many orders of magnitude. The imaginary parts are zero. Some eigenvalues are zero (not shown in the log plot), in particular for the neutrino components, since they don't decay. Neutron and muon decay are a relatively long process and contribute to the plateau close to zero.

The fastest eigenvalues belong to decays of very short-lived particles, such as  $D$ -mesons,  $\Lambda_C^+$  baryons and other heavy flavor particles. This is clearly demonstrated by comparing the eigenvalues of the full matrix with a particle selection inspired by CONEX. Included are only the conventional components up to  $K_S^0$  ( $c\tau = 2.54$  cm), ignoring heavier particles.

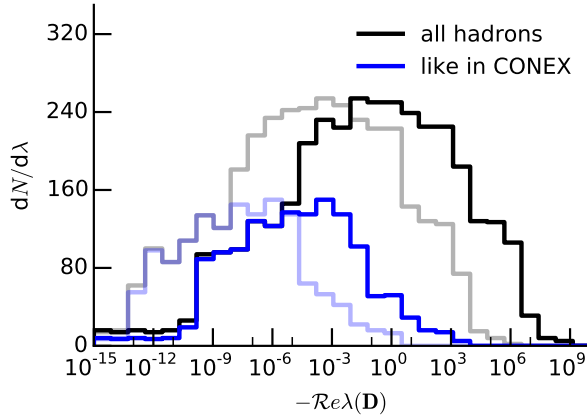


Figure 3.2: Eigenvalues of the decay matrix for the full hadronic system compared with a reduced system, which contains  $p$ ,  $n$ ,  $\pi^\pm$ ,  $K^\pm$ ,  $K_L^0$  and  $K_S^0$ . The solid lines are calculated for the density in the upper atmosphere  $\rho(X = 1 \text{ g/cm}^2)$  and the transparent for the density at the surface.

Let's take the simplest explicit Runge-Kutta type integrator, a forward Euler-method [115]. Using the shortcut notation

$$\vec{y} = \vec{\Phi}$$

$$\mathbf{M}(X) = - \left[ (-\mathbf{1} + \mathbf{C})\boldsymbol{\Lambda}_{int} + \frac{1}{\rho(X)}(-\mathbf{1} + \mathbf{D})\boldsymbol{\Lambda}_{dec} \right]$$

and neglecting the dependence of  $\mathbf{M}$  on  $X$  for a while, we can rewrite Eq. 3.13 as

$$\vec{y}' = -\mathbf{M}\vec{y}. \quad (3.17)$$

One explicit integration step becomes

$$\vec{y}_{n+1} = \vec{y}_n - \mathbf{M}\vec{y}_n\Delta X = (\mathbf{1} - \mathbf{M}\Delta X)\vec{y}_n. \quad (3.18)$$

The exponentiation of a matrix  $\mathbf{A}^n$  tends to zero for  $n \rightarrow \infty$  if the largest eigenvalue is less than unity. By requiring  $\vec{y}_n$  to be bounded the largest eigenvalue of  $(\mathbf{1} - \mathbf{M}\Delta X)$  has to be less than 1, yielding

$$\Delta X < \frac{2}{\lambda_{\max}^*}, \quad \lambda_{\max}^* \in \mathbb{C} \quad (3.19)$$

Now, recall Figure 3.2. For the case where the decay matrix is evaluated for the density of the upper atmosphere,  $\lambda_{\max}^*$  is in the range of  $10^9 \text{ cm}^2/\text{g}$ . In an explicit method the stability constraint above would imply step sizes of the order of  $10^{-9} \text{ g/cm}^2$ . This is obviously not tolerable, since the integration up to  $X_{\text{surface}} \sim 1000 \text{ g/cm}^2$  would require millions of integration steps.

The phenomenon is called stiffness. It is not restricted to certain types of equations but appears mostly in situations where processes of very different time scales come together in a common dynamical system or where the trajectory of the system crosses discontinuities.

There are several methods to tackle stiffness. One approach is based on using more fancy integration methods, which do not result in similar instabilities as demonstrated above with the explicit Euler method. One of these methods which is always stable is the implicit Euler method

$$\begin{aligned}\vec{y}_{n+1} &= \vec{y}_n + \Delta X \vec{y}'_{n+1} \\ \vec{y}'_{n+1} &= (\mathbf{1} + \mathbf{M} \Delta X)^{-1} \vec{y}_n.\end{aligned}$$

This is because the eigenvalues of  $(\mathbf{1} + \mathbf{M} \Delta X)^{-1}$  always satisfy the condition to be less than 1. The problem is, that for each step the matrix cascade equation would have to be inverted. This could be done "relatively efficiently" because coefficients scale with  $1/\rho(X)$ , but a bigger problem is to find a reasonable inversion technique, since the matrix  $\mathbf{M}(X)$  is usually degenerate. Although the degeneracy has mostly technical reasons, a further approach has not been undertaken since already the explicit Euler method can yield satisfactory results, as it will be shown in the next section. Then, one should not expect that such a system can be solved with reasonable accuracy by forcing a "by definition" stable integrator. The origin of stiffness in this case is clearly the underlying physics.

Note that previous numerical codes didn't run into this problem because they didn't include short-lived particles, so the value of  $\lambda_{\max}^*$  was of reasonable magnitude. The authors of [37] claim a step-size of the order of  $5 \text{ g/cm}^2$ , and combine in the stepping algorithm Simpson's rule and numerical evaluation of exponentials. One might speculate that in their code contributions from  $K_S^0$  (the shortest living particle) at lower energies can show inaccuracies. In this work, the direct numerical evaluation of exponential functions could not be used, since some of the decay coefficients by far exceeded the argument's range in double precision.

### 3.3 The resonance approximation

As we have understood in the last section, the numerical solution of the coupled cascade equations becomes a stiff problem as soon as short-lived particles are added to the set of hadrons. The sketch in Figure 3.3 illustrates what the problem is. If the step size is chosen according to the decay lengths of short lived particles the equations become stiff. On the other hand, at very high energies the decay length elongates due to time dilation. So even the short-lived particles can travel long enough through the medium to interact.

The key idea is to separate the energy range into two regions, where in the former particles can be treated similar to a resonance which decays at its vertex. In the latter, high-energy region, the particles are allowed to propagate and experience attenuation due to interactions.

To derive a formalism for "chained" or prompt decays, let us follow the next few steps. Let  $\vec{\eta}_n^{int}$  be the vector containing the fluxes of all resonances which are created during the integration step  $n$ . Using the matrix notation

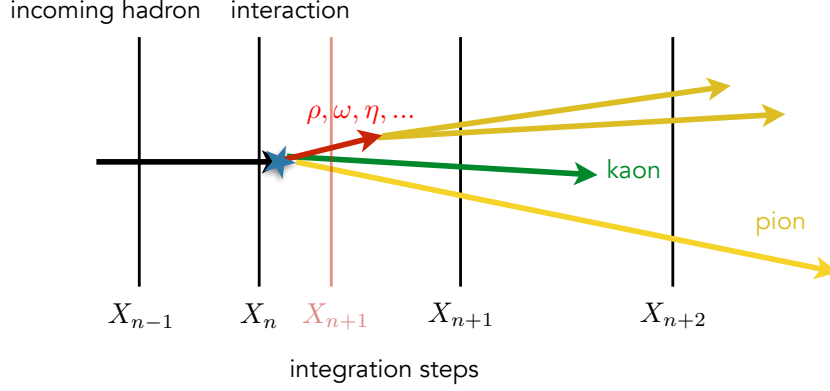


Figure 3.3: Sketch of interrelation between cascade physics and stiffness. To handle short-lived particles in the same way as other hadrons the step-size has to be small (red shaded step, not in scale).

and forward Euler integration as in the last section, we can write

$$\vec{\eta}_n^{int} = \mathbf{C}_{h \rightarrow \eta}^{res} \Lambda_{int} \vec{\Phi} \cdot \Delta X_n. \quad (3.20)$$

$\mathbf{C}_{h \rightarrow \eta}^{res}$  denotes a  $(k \times d_\Phi)$  matrix similar to  $\mathbf{C}$  defined in Eq. (3.12), which contains production coefficients for resonances in interactions of hadrons. According to the approximation, at lower energies all created resonances have to decay into ordinary particles within the same integration step. By writing this condition for a single resonance type  $k$  and one energy bin (index omitted for clarity)

$$\eta_{k,n+1} \equiv 0 = \eta_{k,n} - \frac{1}{\lambda_{dec,eff}^{\eta_k}} \eta_{k,n} \cdot \Delta X_n, \quad (3.21)$$

we obtain the effective decay length

$$\lambda_{dec,eff}^{\eta_k} = \Delta X_n = \rho(X) \tilde{\lambda}_{dec,eff}^{\eta_k}. \quad (3.22)$$

Using  $\lambda_{dec,eff}^{\eta_k}$  instead of the true decay length for short-lived resonances we make sure that all particles decay after one integration step in  $X$ . Note that  $\lambda_{dec,eff}^{\eta_k}$  does not depend on the properties of the resonance. The contribution to the flux of ordinary particles from decays of short-lived intermediate states is

$$\begin{aligned} \Delta \vec{\Phi}_{n+1}^{\eta \rightarrow} &= \mathbf{D}_{\eta \rightarrow h}^{res} \Lambda_{dec,eff}^{res} \vec{\eta}_n \cdot \frac{\Delta X_n}{\rho(X)} \\ &= \mathbf{D}_{\eta \rightarrow h}^{res} \vec{\eta}_n, \end{aligned} \quad (3.23)$$

where  $\mathbf{D}_{\eta \rightarrow h}^{res}$  is a  $(d_\Phi \times k)$  matrix, containing decay coefficients of resonances into hadrons and leptons. The diagonal matrix  $\Lambda_{dec,eff}^{res}$  commutes and is constructed as in Eq. (3.9).

By inserting Eq. (3.20) in (3.23) we obtain the expression for the production of ordinary particles via short-lived intermediate states

$$\begin{aligned} \Delta \Phi_{n+1}^{\eta \rightarrow} &= (\mathbf{D}_{\eta \rightarrow h}^{res} \cdot \mathbf{C}_{h \rightarrow \eta}^{res}) \Lambda_{int} \Phi_n \cdot \Delta X_n \\ &= \mathbf{R} \Lambda_{int} \Phi_n \cdot \Delta X_n. \end{aligned} \quad (3.24)$$

Following the same logic, we can derive the expression for any number  $k$  of ordered chains of prompt processes

$$\begin{aligned}\Delta\vec{\Phi}_{n+1}^{\text{chained}} &= \left( \prod_k D_k^{\text{res}} \right) C \Lambda_{int} \vec{\Phi} \Delta X_n \\ &= R \Lambda_{int} \vec{\Phi} \Delta X_n,\end{aligned}\quad (3.25)$$

or by going back to differentials

$$\frac{d\vec{\Phi}^{\text{chained}}}{dX} = R \Lambda_{int} \vec{\Phi}. \quad (3.26)$$

In fact, this result should be valid in general for all types of dynamical systems.

The interaction of resonances becomes important at high energies, where

$$\lambda_{dec} \approx \lambda_{int}. \quad (3.27)$$

A new parameter  $t_{mix} = \lambda_{dec}(E)/\lambda_{int}(E)$  is a threshold value, separating the energy regime where the particle can be treated as a resonance from a regime where it has to be a full member of the cascade and represented by its own vector in  $\vec{\Phi}$ . In other words, if the interaction probability drops below a certain percentage, treat the particle as if it would be a resonance. A reasonably good value was determined to be  $t_{mix} = 0.05$ .

$\vec{\Phi}^\omega = \begin{pmatrix} \Phi_{E_0}^\omega & \dots & \Phi_{E_i}^\omega \\ & \equiv 0 & \\ & \text{treat as} & \\ & \text{resonance} & \end{pmatrix}$	$\begin{array}{c} \lambda_{dec} < t_{mix} \lambda_{int} \\ \Phi_{E_{i+1}}^\omega \dots \Phi_{E_N}^\omega \end{array}^T$ <p style="text-align: center;">transport as particle</p>
------------------------------------------------------------------------------------------------------------------------------------------------------------------	--------------------------------------------------------------------------------------------------------------------------------------------------------------------------------------

Figure 3.4: Splitting of the energy grid in a resonant part, where the particle promptly decays, and an ordinary part, where it behaves as a longer lived cascade member.

As a further explanation, consider the flux vector for an arbitrary particle  $\omega$  where the decay and interaction lengths cross over within the energy range of the calculation. Its energy grid can be split into two parts, one, which is always zero because in this regime the particle promptly decays and in the second regime it is propagated as if it would be an ordinary particle (Figure 3.4). This splitting results in a certain "cut" structure of the sub-matrices. Figure 3.5 illustrates these cuts using colored surfaces for the non-zero elements. The solid surfaces can be subdivided into three regions:

- (blue) Both the particles  $\omega$  and  $\phi$  are treated as ordinary particles, they survive a number of integration steps, they can decay and interact.
- (red) Both particles are in their resonance regime, so they will not populate the flux vector  $\vec{\Phi}$ . Instead their contribution is implicitly treated as a chained decay of the particle preceding  $\omega$  using Eq. (3.26).

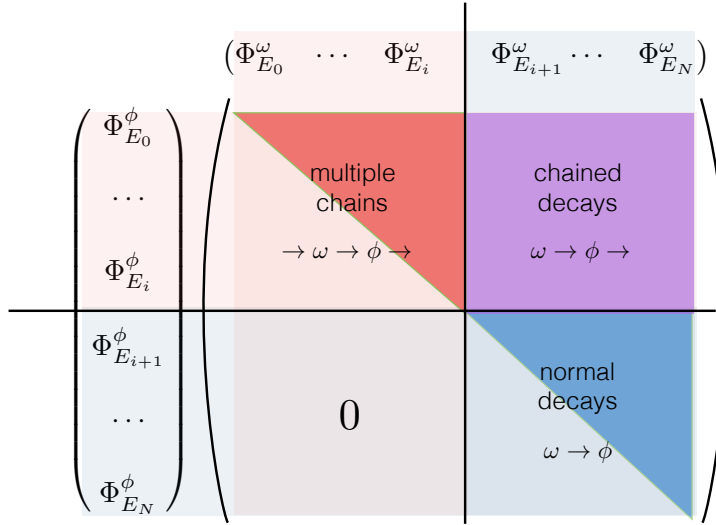


Figure 3.5: Cut structure for a sub-matrix  $\mathbf{C}_{\omega \rightarrow \phi}$

- (violet) The particle  $\omega$  is in its normal "propagation" regime and would create  $\phi$  in its resonance regime. The same formalism of Eq. (3.26) is used to calculate this contribution via single or multiple decay chains into particles which are long-lived at these energies.

This complicates somewhat the procedure to fill the  $\mathbf{C}$ ,  $\mathbf{D}$  and the  $\mathbf{R}$  matrices, where for each particle the individual threshold has to be taken into account as "cut" in row and/or column. However, in practice this is formulated in a short recursive routine. Also the implementation does not explicitly assemble the  $\mathbf{R}$  matrix but directly the sum  $\mathbf{C} + \mathbf{R}$ .

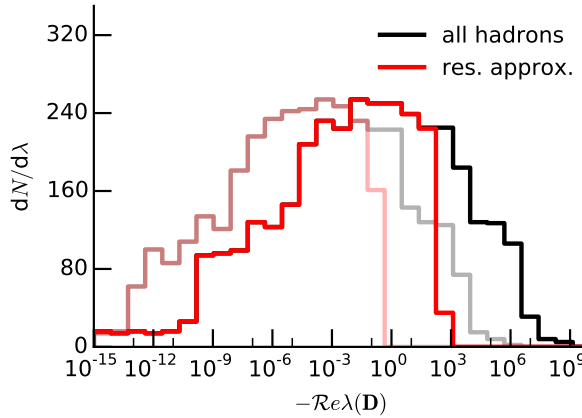


Figure 3.6: Eigenvalues of the decay matrix with and without the resonance approximation. The solid lines are calculated for the density in the upper atmosphere  $\rho(X = 1 \text{ g/cm}^2)$  and the transparent for the density at the surface.

The net result is a very **significant reduction of the stiffness** by approximating decays of heavy flavors and short-lived particles with prompt decays

at energies where their interaction with the medium can safely be neglected. Figure 3.6 proves this result on the level of the eigenvalues. The fastest mode  $\lambda_{\max}^*$  is now six orders of magnitude smaller, affecting by the same amount the stability region of the numerical integrator. Any method can be used to integrate these equations including simple forward Euler steppers. A more sophisticated method could even further reduce the computational time, although for the current set of applications and the complexity of the hadronic cascade a calculation time of a few ( $< 10$  s) is sufficient.

The implementation as computer software is discussed in the next chapter.

# Chapter 4

## The MCEQ code

The program MCEQ (Matrix Cascade EQuations) numerically solves the cascade equations by using the methods from the last chapter.

A popular approach in the current scientific programming paradigm is to write the performance critical parts in a medium or high level language such as C/C++ (or even parts in FORTRAN), but then use a scripting or very high level language like PYTHON to "glue" together independent functional units into a working data processing or calculation chain. Some frameworks based on this approach are the Gaudi framework<sup>3</sup>, its derivative ATLAS' Athena [27] or IceCube's IceTray. This scheme aims to simplify the user's interaction with more complex parts via clear interfaces and in a human-readable programming language.

MCEQ is written in this state-of-the-art approach using PYTHON together with numerical libraries. The open-source code is made available to the community<sup>4</sup> under the terms of the *MIT License*, the most permissive license available.

The first sections of this chapter try to highlight aspects of the software which have been found to be of practical importance. The full program documentation is available online<sup>5</sup>. Results follow in the next chapter.

### 4.1 Goals and motivation

Beyond just being a testbed for the numerical solutions of cascade equations in matrix form, the feature list was motivated from discussions with potential users from the IceCube Collaboration. Since atmospheric neutrinos and muons are the largest background for neutrino volume detectors, their systematic uncertainties depend to some extent on how precise these backgrounds are taken into account. Many of the physical models in a atmospheric neutrino or muon calculation are indeed uncertain. Hadronic interaction models can only be verified at energies accessible to man-made machines, not at cosmic ray en-

---

<sup>3</sup><http://proj-gaudi.web.cern.ch/proj-gaudi/>

<sup>4</sup><https://github.com/afedynitch/MCEq>

<sup>5</sup><http://mceq.readthedocs.org/en/latest/>

ergies. The flux of cosmic rays, in particular the composition above the knee, is also uncertain and there are larger variations between the available models. Further, the atmosphere influences the shape of the atmospheric lepton spectrum and can not be taken into account completely. It can only be modeled in sufficient detail in Monte Carlo simulations, which take too much time to be re-run for each variation. The goals of this program can be summarized in the following list:

1. a calculation method, which is fast enough for systematic studies of atmospheric lepton uncertainties,
2. detailed access and variation to the model of the primary cosmic ray flux,
3. calculations of the average shower, for example the lepton production profile or the energy spectrum of secondaries at any depth  $X$  for a single primary hadron or nucleus,
4. calculation of prompt lepton fluxes from decays of charm,
5. a choice of hadronic interaction models or if possible different versions of a single interaction model with upper bound and lower bound parameters,
6. interchangeable atmospheric profiles obtained either from fits, models of tables,
7. curved geometry and non-divergent behavior for horizontal angles,
8. open access or open-source, so researchers can run and modify the calculations, implement new models or extend the existing ones by themselves

## 4.2 About the software

### 4.2.1 General design and program structure

MCEQ is object-oriented (OO) code. Its concept is based on the architectural patterns of *model-view-controller* (MVC) and the *single-responsibility-principle* (SRP) [101]. The chart of the MVC pattern in Figure 4.1 illustrates the separation of the user from the core functions 'model' through a controller, which takes care of the initialization, command ordering and calculations. As soon as results become available, the 'model' updates the view, the interface for the user. This methods' goal is to separate the more static core functionality from the user interface, which can be anything starting from the command-line to an `ipython notebook`<sup>6</sup> or a graphical-user-interface. By having a flexible "front-end" one avoids altering large fractions of the code in computing related parts. From a scientific tool, in contrast to a commercial software product, users ("experimentalists") typically want to freely choose how they interact with

---

<sup>6</sup><http://ipython.org/notebook.html>

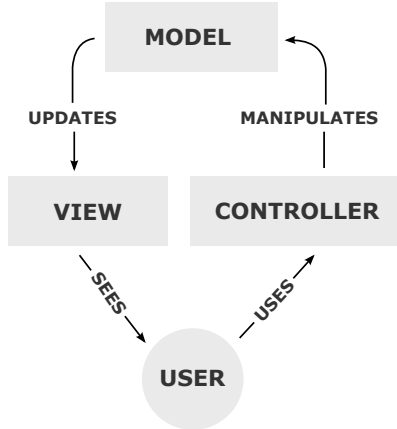


Figure 4.1: Model-view-controller pattern

the software with ideas ranging from a complex experimental data-analysis framework to a simple script producing ASCII tables for plotting.

The SRP is a very powerful method to keep an object-oriented code structured and understandable. It states that each class has a clear responsibility and does only one thing. A class is not allowed to do this *and* that. For example the `class InteractionYields()` is a representation of inclusive particle distributions, obtained from interaction models and saved as files. It knows how to unpack tabulated data from disk, create a content index and fulfill its responsibility to present these data in a specified way to a class higher up in the functional hierarchy. It does not process the decay tables, which are handled in the same way but by the dedicated `class DecayYields()`. Functional similarities are instead grouped into short inheritance trees, like for example in the set of classes representing different density models of the Earth's atmosphere (see Figure 4.3).

The patterns described above are not strictly forced, but rather used as general guidelines for the architecture. The highest priority in the development of scientific code is functionality (physics). Following these patterns during development helped and indeed, additional functionality could be added quickly without breaking existing code.

The structural entities are packages and modules<sup>7</sup>. The dependency graph for the modules is shown in Figure 4.2. The SRP is applied on module level, what can be seen in absent inter-modular dependencies. One can spot from the module diagram the complete set of ingredients for cascade equation calculations, like calculation kernels (numerical integration routines), cosmic-ray primary flux parameterizations, tabulated data, density profiles and particle properties.

---

<sup>7</sup>Modules are separate source files containing variables, functions and classes. Packages are file system folders containing an (empty) `__init__.py` file and at least one module. The PYTHON interpreter converts the file hierarchy into a `package.submodule` import hierarchy, similar to JAVA, C#, .NET, RUBY etc.

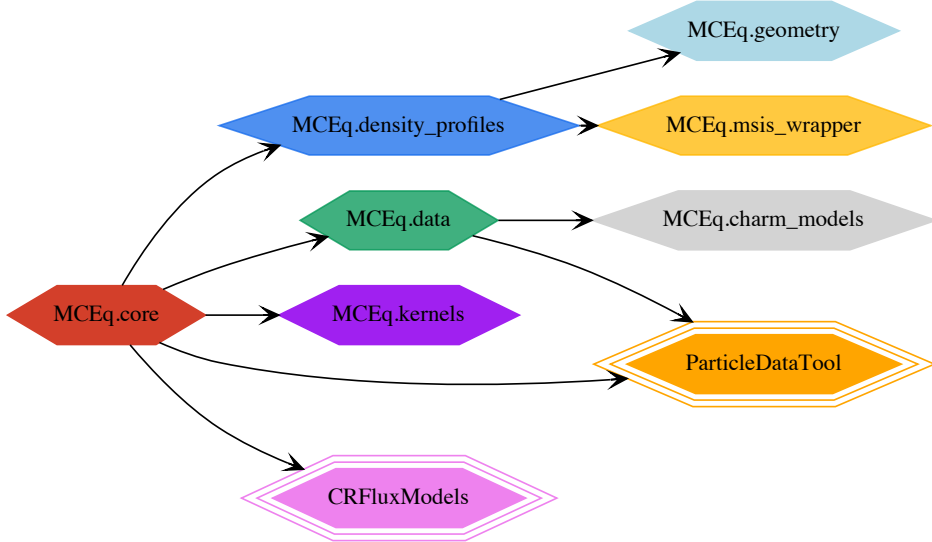


Figure 4.2: Modules in MCEQ. The arrow symbolizes a "depends on" relationship. The two items with multiple boarders are independent single-module packages.

#### 4.2.2 Package MCEQ

Figure 4.3 shows a simplified UML (unified modeling language) class diagram of the package. As already noted in the module overview mutual dependencies between classes in the second rank are reduced. Inheritance hierarchies have a maximum length of three.

##### Module core and `class MCEqRun()`

Most of the program flow is implemented in this main or controller class. It is the first and usually the only object invoked by the user. In fact, SRP is not cleanly implemented in the current version because this main class has two responsibilities. First, to initialize all of its members in-order and second, to launch the calculation kernels. This has historical reasons and will be solved in the upcoming version by creating an "initializer" class, which takes care of parameter changes and keeps track which objects need additional initialization steps.

The general usage pattern is

```

from MCEq.core import MCEqRun

# import the global configuration
from mceq_config import config
# import the primary cosmic ray flux module
import CRFluxModels as pm
  
```

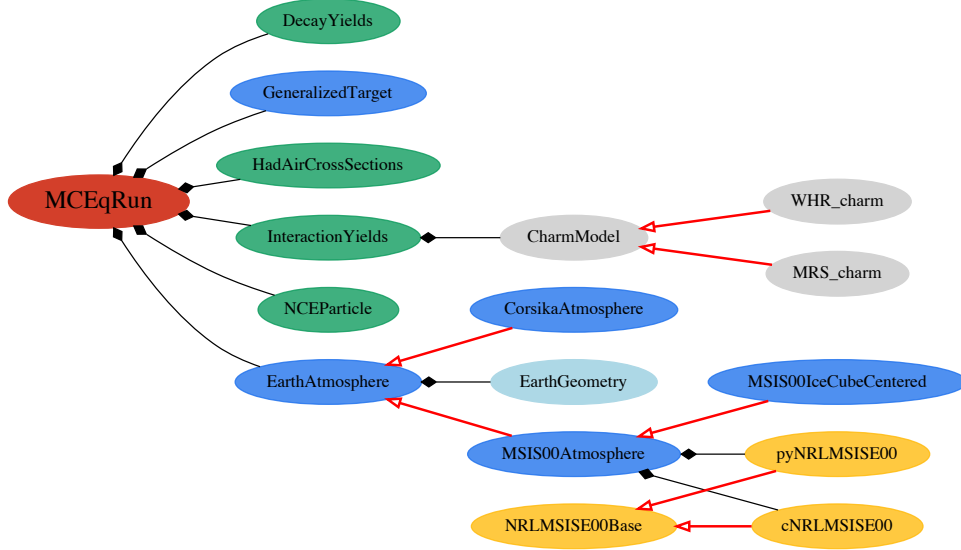


Figure 4.3: (UML) Class diagram of the MCEQ package. Color symbolizes the membership of a class to a module according to the color scheme in Figure 4.2. Hollow diamond edges represent *composition* (objects belong exclusively to the class at the diamond). The meaning of the hollow arrows is "inherits from", showing the short inheritance hierarchies.

```

# create an instance of the management class
# and expand the configuration dictionary into
# the keyword argument list
mceq_run = MCEqRun(interaction_model='SIBYLL2.1',
                     primary_model=(pm.HillasGaisser2012, "H3a"),
                     **config)

# set or change additional parameters using
# public setter methods
mceq_run.set_theta_deg(60.)

# execute the solver according to the options
# provided in the config file
mceq_run.solve()

```

The constructor of `MCEqRun` triggers the generation of particle lists, the loading of tables, the calculation of decay and interaction lengths, the initialization of the density profile and the calculation of the density spline.

The method `solve()` dispatches the call to the appropriate kernel according to the options selected in the configuration, such as `numpy`, `MKL` or `CUDA` (see section 4.2.3).

The results of the calculation are retrieved by

```

# obtain energy grid (fixed) of the solution ,
# (x-axis of the figures)
e_grid = mceq_run.e_grid

# define the power of E to multiply the solution with
# (magnification factor)
mag = 3

# obtain conventional flux of muons at the
# end of integration path (surface)
flux = mceq_run.get_solution('conv_mu+', mag)
+ mceq_run.get_solution('conv_mu-', mag))

```

At this step the user can choose to change parameters using the setters and run subsequent calculations, to plot or to store the results and terminate the execution. The most convenient and therefore recommended graphical user interface is the `ipython notebook`.

### Module data

The classes in this module, depicted green in Figure 4.3, handle hadronic cross-section tables, particle properties and tabulated distributions obtained from Monte Carlo generators. MCEQ is distributed together with byte-compressed versions of the data files for saving space.

The `class HadAirCrossSections()` implements an interface to a table of particle production cross-sections in hadron-air collisions  $\sigma_{\text{prod,h-air}}(E_{\text{lab}})$  in units of mb. Cosmic ray hadronic interaction models provide native routines to obtain  $\sigma_{\text{prod,h-air}}(E_{\text{lab}})$ . They are evaluated at central points of the energy grid and stored on disc as `numpy` arrays. The class also handles the substitution of unknown cross-sections, for example  $D$ -air or  $\Lambda_C$ -air, with known cross-sections like pion-air and nucleon-air, respectively.

The `class InteractionYields` interfaces with a larger dictionary of inclusive particle yields  $dN/dx_F$ , generated from running the Monte Carlo generators for various projectile types and energies (see section 4.3). The resulting histograms are collected from distributed (parallel) calculations on general purpose computer clusters into ordered 2-dimensional arrays, as in Eq. (3.10). During initialization the class traverses and indexes the tree of the projectile's secondary (daughter) particles, instead of evaluating these relationships during run-time.

The `class DecayYields` has an interface similar to `InteractionYields` for inclusive particle decay spectra. Just the roles of projectile and mother (decaying) particle are interchanged (read more about the details in section 4.3).

### 4.2.3 Performance acceleration and the `kernels` module

The `kernels` module contains only module-level functions. The term kernel refers here to the integration routine itself. The evaluated equation is the

forward Euler step

$$\vec{\Phi}_{i+1} = \vec{\Phi}_i + \left[ (-\mathbf{1} + \mathbf{C})\Lambda_{int} + \frac{1}{\rho(X_i)}(-\mathbf{1} + \mathbf{D})\Lambda_{dec} \right] \vec{\Phi}_i \cdot \Delta X_i. \quad (4.1)$$

Access to more sophisticated integration methods is made available by providing an interface to `scipy.integrate.ode`, a wrapper around LINPACK's collection of integrators<sup>8</sup>. It includes various implicit and explicit methods, fine grained control over relative or absolute tolerances, adaptive step-sizes etc.

The interface to integration methods with error-control allowed to compare and verify the results of the simple algorithm above. The error on the flux of leptons is usually negligible, because the energy bins, which are more affected by linearization are the lower energy bins of sub-leading particles. In practice the smoothness is not seriously affected and relative numerical errors up to  $10^{-3}$  are tolerable.

Also, it is possible to use a Jacobian matrix to increase the precision of the linearized solver. The problem is that the original FORTRAN routines directly access the array of the Jacobian, requiring it to be stored in a dense matrix format. Since the Jacobian has to be evaluated at each step in  $X$  (because of  $\rho(X)$ ), the performance penalty is high compared to alternative methods, without explicit forms of a Jacobian matrix.

In practice the multiplication of static matrix contents is carried out in advance

$$\begin{aligned} \text{int\_m} &= (-\mathbf{1} + \mathbf{C})\Lambda_{int} \\ \text{dec\_m} &= (-\mathbf{1} + \mathbf{D})\Lambda_{dec}. \end{aligned}$$

The integration routine in numpy notation becomes

```
phi = np.zeros(dimension_full_eqn_system)

# Fill the nucleon fluxes with cosmic ray flux
# at the top of the atmosphere
set_initial_condition(phi)

#loop over the number of integration steps
for step in xrange(nsteps):
    phi += (int_m.dot(phi) +
            dec_m.dot(rho_inv[step] * phi)) * dX[step]
```

The step-size is calculated according to the stability constraint (3.19). To avoid calculating the eigenvalues  $\lambda^*$ , one can formulate an alternative criterion based on the shortest decay length. After applying the resonance approximation as in section 3.3, we can require, as in Eqns. (3.21) and (3.22), we can the shortest-lived particle density to be non-negative

$$\Phi_{\text{shortest},n+1} = \Phi_{\text{shortest},n} - \frac{1}{\lambda_{\text{dec,max}}} \Phi_{\text{shortest},n} \cdot \Delta X_n \geq 0, \quad (4.2)$$

---

<sup>8</sup> <http://docs.scipy.org/doc/scipy-0.14.0/reference/generated/scipy.integrate.ode.html>

and obtain a condition for the step-size that ensures positive fluxes for all particles

$$\Delta X_n(X) \leq \rho(X) \tilde{\lambda}_{\text{dec,max}}. \quad (4.3)$$

The step-size scales with the density profile and can be calculated a priori as soon as the trajectory and the density spline are known. An additional safety margin of  $\frac{1}{2}$  reduces the linearization error for this bin. With this definition, the integration through a standard atmosphere on a vertical trajectory requires  $\sim 4000$  integration steps. A horizontal trajectory for  $\theta = 0$  requires around 50000 integration steps.

### Basic Linear-Algebra Subroutines (BLAS)

Since this integration only involves matrix-vector or vector-vector operations, it can be represented as BLAS expressions<sup>9</sup>. BLAS is a method to separate architectural optimizations from algorithmic optimizations. There are plenty of implementations, both open-source and proprietary, for various processor and memory architectures. In high-performance computing BLAS helps the developer to avoid optimizing a program on a very low level. When using a BLAS library one can expect a close to ideal implementation of common vector and matrix operations. The performance can vary between the implementations depending on the computation scenario [141]. An interesting insight into implementation details of BLAS is presented here<sup>10</sup>. This example illustrates advanced optimization techniques applied to matrix-matrix multiplications.

There are three groups or levels of subroutines. Level-1 refers to operations on 1-dimensional variables, i.e. on vectors with vectors. Level-2 is a collection of matrix-vector and level-3 of matrix-matrix routines. The present code uses one level-2 instruction `gemv` (general matrix-vector multiplication or dot-product)  $y \leftarrow \alpha Ax + \beta y$  and one level-1 instruction `axpy`, the vector-vector addition  $y \leftarrow \alpha x + y$ .

I have chosen the Intel Math Kernel Library® (MKL), since it is free for academic applications and it employs the highest level of vectorization on present Intel x86 CPUs. It exploits the acceleration through 256-bit or 512-bit wide vector units on AVX® or AVX2® CPUs for *SandyBridge* architectures and above, without additional user code. Since the run-time of the current version of the code is sufficiently short, it was beyond the scope of this study to research on alternative, possibly faster, libraries.

For the integrator code from above the BLAS notation is

```
for step in xrange(nsteps):
    # delta_phi = int_m.dot(phi)
    gemv(trans='T', m=m, n=n, alpha=1.0, A=int_m,
          x=phi, beta=0.0, y=delta_phi)

    # delta_phi = rho_inv * dec_m.dot(phi) + delta_phi
```

---

<sup>9</sup><http://www.netlib.org/blas/>

<sup>10</sup><http://apfel.mathematik.uni-ulm.de/~lehnsghpc/gemm>

```

gemv(trans='T', m=m, n=n, alpha=rho_inv[step]),
      A=dec_m, x=phi, beta=1.0, y=delta_phi)

# phi = delta_phi * dX + phi
axpy(alpha=dX[step]), x=delta_phi, y=phi).

```

Another advantage of BLAS is that the syntax is a de-facto standard. The routines on GPUs or many-integrated-core (MIC) accelerators accept the identical code with a few modifications or by just exchanging the library.

### Dense vs sparse algebra

A matrix is sparse if it contains a small percentage of non-zero elements [130]. The goal in using sparse matrices is either to save space/memory and/or to save time. The idea is to involve only the non-zero elements in the computation and ignore the zeros. The matrices occurring in MCEQ are sparse, containing only a few percent non-zero elements. There are several choices for packing the data into memory. The choice of packing method depending on the sparsity pattern of the matrix and the optimization goal. Examples for sparse matrix

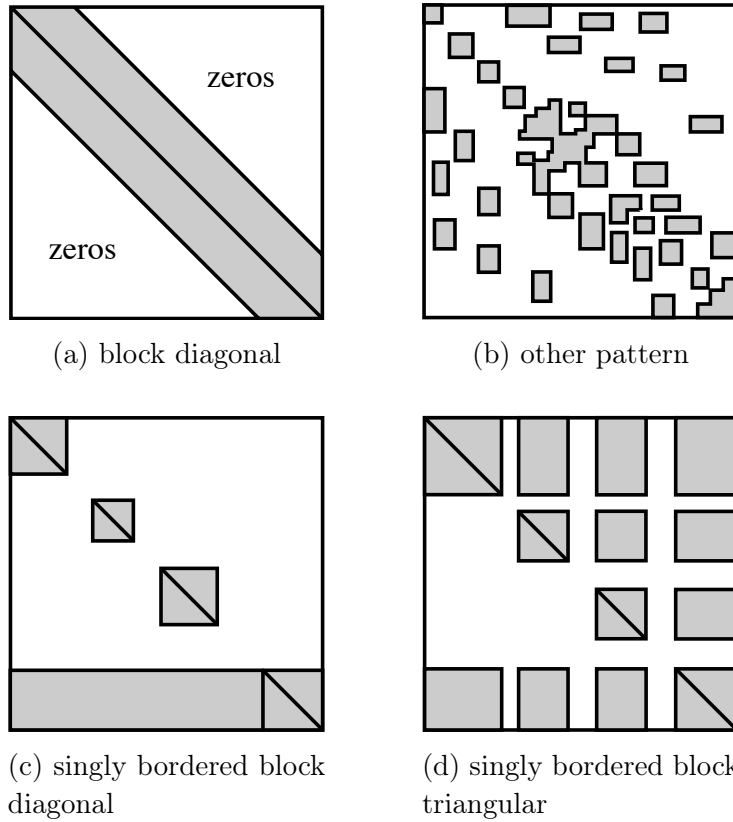


Figure 4.4: Examples of sparse matrix patterns [115]

patterns are given in Figure 4.4. Often it is useful to minimize fill-ins, i.e. small blocks of non-zero elements scattered around the matrix. There are algorithms available which can analyze or factorize the matrix in a pre-conditioning step

[115]. For inclusive flux calculations MCEq is fast enough, so the step of pre-conditioning is omitted, but could be added in future.

Table 4.1: Comparison of storage and computational time for different sparse packing methods.

Packing method	size [MB]		dot-product CPU time	
	<code>int_m</code>	<code>dec_m</code>	<code>int_m</code>	<code>dec_m</code>
compressed sparse row (CSR)	15.7	3.35	-	-
compressed sparse column (CSC)	15.7	3.35	+6%	+6%
block sparse row (BSR)	12.6	2.98	+23%	+38%
dense	299	299	+1100%	+5000%

Some storage and computational time gains for the interaction and decay matrix in MCEq are given in Table 4.1. The numbers draw a clear picture. Dense matrices should be avoided for this type and size of equation systems. Naïvely one might expect that skipping zero-valued calculations in loops by using conditional expressions could yield a similar performance gain. But will be surely slower than using sparse matrices, since branchings prevent the compiler from using the vectorization units and from efficient cache organization.

Currently the module contains four functions:

- `kern_numpy`: default and fall-back implementation using the dot-product notation. Supports dense and sparse matrix formats.
- `kern_CUDA_dense`: dense BLAS implementation for nVidia® GPUs using the CUBLAS® library
- `kern_CUDA_sparse`: sparse BLAS implementation for nVidia® GPUs using the CUBLAS® library
- `kern_MKL_sparse`: sparse BLAS implementation for x86/Intel CPUs using Intel’s Math Kernel Library

As standard choice the `kern_MKL_sparse` routine is highly recommended with a fall-back option to `kern_numpy`. The GPU tests were not conclusive. When using dense FP32 CUBLAS<sup>11</sup> on a weak GPU (nVidia GeForce® m650GT with 1GB GDDR5), it outperformed an Ivy Bridge Intel Core i7-3720QM 2.6 GHz with dual-channel DDR3-1600 memory and MKL (AVX, FMADD, 4 threads) by a small margin or a factor of two compared to the FP64 MKL result. Despite having only a small fraction of its FP32 performance, the GPU had not enough memory to perform the same calculations with FP64 precision. The interface to CUSPARSE<sup>12</sup>, nVidias sparse algebra library, was buggy and it initiated memory copies in-between each step. Therefore, the routine `kern_CUDA_sparse` is labeled as experimental.

<sup>11</sup> <https://developer.nvidia.com/cublas>

<sup>12</sup> <https://developer.nvidia.com/cusparse>

#### 4.2.4 Current and future execution performance

One calculation of an atmospheric spectrum for the default set of models takes in total around ten seconds, of which six or seven seconds are spent on initialization. The integration itself takes around two seconds. The numbers are given for a mobile Quad-Core Intel Core i7-3720QM with MKL.

More inclined cascades take more time, because a larger fraction of the air-shower's trajectory runs through thin densities of the upper atmosphere. From looking at the eigenvalues in Figure 3.6 it becomes clear that to reside within the stability margin, the integrator has to do more smaller steps. Another reason is that one has to integrate up to slant depths  $\mathcal{O}(10^4 \text{ g/cm}^2)$  instead of the typical  $\mathcal{O}(10^3 \text{ g/cm}^2)$  for vertical showers. The calculation time increases in the case of horizontal cascades up to 30-40 seconds.

An interesting feature of sparse matrices is related to the performance scaling for different models. For example, interaction models without charmed hadron production have fewer non-zero coefficients in matrix  $\mathbf{C}$ , resulting in fewer calculations for the dot-product. The performance notably increases by several tens percent.

The program as it is, is currently fast enough for all known use cases. If in future it extends to lower energies, includes electromagnetic cascades or is formulated in 2- or 3-dimensional geometry, there is enough room to scale.

Caching of the sparse matrices can be employed to reduce the main memory footprint and dramatically reduce initialization times. For atmospheric splines a cache is already implemented. With a mostly negligible loss in precision, the total execution time could be reduced to 1-2 seconds.

Finally, linear algebraic expressions have parallel nature. At this moment the code was mostly tested on 2- or 4-core general purpose PCs. Todays high-performance workstations or compute nodes can easily reach several tens of cores. By employing BLAS-libraries one gets shared-memory parallelization for free. The techniques used by BLAS on CPUs are NUMA-aware symmetric-multi-processing, cache optimizations and optimal use of vectorization units. By design GPUs are using a large number of simple ALU units and they are optimized to perform the same arithmetic operation on large arrays in parallel. They are perfectly suited for calculations formulated as linear-algebraic expressions. But their simpler architecture, with less efficient cache algorithms and instruction set, makes them better suited for larger computations than what MCEQ is now. By using sparse matrices the bottle-neck is anyways shifted to the memory bandwidth instead of the floating-point unit's throughput, as it is often the case for dense matrices.

For (piece-wise) homogeneous media the problem becomes piece-wise linear. One would have to compute the trade-off between performance and precision of matrix exponentiation and iterative integration and choose a more appropriate integration routine.

## 4.3 Supplied models

The distribution contains a number of physical models for hadronic interactions, atmosphere and primary cosmic rays. This section is about quantitative aspects of MCEQ.

### Hadronic interactions and particle species

Although other models have been tested in early calculations, the various development versions of SIBYLL were established as the de-facto standard. The selection of baryons, mesons and leptons was, for example, motivated by the particles known to SIBYLL instead of the complete PDG list. For the calculation of inclusive particle production spectra all of the unstable particles were set to stable, including very short-lived resonances. The tool `SpectraForMCEq` (section A.4) organizes and verifies batch runs of event generators on general purpose clusters. Up to 25 million events per (primary particle) projectile type-energy grid point are calculated. The high event number is necessary to obtain smooth distributions for rare heavy particles.

Most of the recent cosmic-ray hadronic interaction models are included (via the `PyInteractionModels` package (appendix A.3)):

- SIBYLL-2.1 [18]
- various development versions of SIBYLL-2.3 [117]
- DPMJET-2.55 [116, 36]
- QGSJET-II-03 and 04 [108]
- Development version of DPMJET-III

The typical list of particles in MCEQ is usually restricted to those which are known to SIBYLL, even if an interaction model knows more particles (they are not important for cascades anyways). In case the critical energy of a

Table 4.2: Particles in MCEQ.

leptons	$\mu^+, \mu^-, \tau^+, \tau^-, \nu_e, \nu_\mu, \nu_\tau, \bar{\nu}_e, \bar{\nu}_\mu, \bar{\nu}_\tau$
mesons	$K^+, K^-, K_L^0, K_S^0, \pi^+, \pi^-, D^+, D^-, D^0, \bar{D}^0, D_s^+, D_s^-, K^{*+}, K^{*-}, K^{*0}, \bar{K}^{*0}, D^{*+}, D^{*-}, D^{*0}, \bar{D}^{*0}, \eta, \eta^*, \eta_C, J/\Psi, \omega, \phi, \pi^0, \rho^+, \rho^-, \rho^0$
baryons	$p, \bar{p}, n, \bar{n}, \Delta^+, \Delta^{++}, \bar{\Delta}^{--}, \bar{\Delta}^-, \Delta^0, \bar{\Delta}^0, \Lambda^0, \bar{\Lambda}^0, \Omega^-, \bar{\Omega}^+, \Sigma^{*+}, \bar{\Sigma}^{*-}, \Sigma^{*+}, \Sigma^{*0}, \bar{\Sigma}^{*0}, \Sigma^+, \bar{\Sigma}^-, \Sigma^0, \bar{\Sigma}^0, \Lambda_C^+, \bar{\Lambda}_C^-, \Omega_C^0, \bar{\Omega}_C^0, \Sigma^-, \bar{\Sigma}^+, \Xi^-, \bar{\Xi}^+, \Xi^0, \bar{\Xi}^0, \Xi_C^+, \bar{\Xi}_C^+, \Xi_C^0, \bar{\Xi}_C^0, \Sigma_C^{*+}, \Sigma_C^{*++}, \bar{\Sigma}_C^{*-}, \Sigma_C^{*0}, \bar{\Sigma}_C^{*0}, \Sigma_C^+, \Sigma_C^{++}, \bar{\Sigma}_C^{--}, \bar{\Sigma}_C^-, \Sigma_C^0, \bar{\Sigma}_C^0, \Xi^{*-}, \bar{\Xi}^{*+}, \Xi^{*0}, \bar{\Xi}^{*0}$

particle exceeds the energy range of the calculation ( $50 - 10^{10}$  GeV), it will not be part of the flux vector  $\vec{\Phi}$  and always treated implicitly via the resonance approximation (section 3.3). A typical dimension of the  $\mathbf{C}$  or  $\mathbf{D}$  matrix is  $6000 \times 6000$ . Depending on the model it results in up to 5% non-zero elements.

## Initial condition

The primary flux is modeled in the superposition approach, i.e. the flux of nuclei is decomposed into fluxes of nucleons at the energy per nucleon. The superposition approach is sufficient for calculations of inclusive fluxes, where the "average shower" matters instead of the statistical fluctuations.

Various models are made available through the interface to the `CRFluxModels` package (section A.1). An "average" hadronic shower can be computed for one single primary particle or nucleus. The code accepts continuous energies and interpolates between two neighboring energy bins.

## Density profile

Density profile refers either to a model of the Earth's atmosphere or to a general target, which consist of a series of homogeneous materials. The integration routines are made independent of the concrete implementation of the density profile  $\rho(X)$  by relying on a pre-calculated spline. Some details about the calculation steps needed for the spline are located in section 2.2.2.

This approach is easy to extend because there the profile  $\rho(h)$  can be based on any type of data, such as a numerical model or tabulated data from satellite observations. The following options are available in the current distribution of the code:

- CORSIKA atmospheres, based on Linsley parameterizations with five exponential functions. Parameter tables are taken from [78] for the South-Pole atmosphere in summer and winter, the US Standard atmosphere [129], and one for middle Europe
- the static NRLMSISE-00 atmospheric model [113] is provided via an `ctypes` interface to the C-version<sup>13</sup> and the native `PYTHON` version<sup>14</sup>. The `PYTHON` version is simply translated from C, without using `numpy` and vectorized expressions. It is therefore way too slow for any serious calculations.
- For NRLMSISE-00 the location above the detector is taken independent of the zenith angle. To enable experimentalists to calculate the neutrino fluxes coming from all around the globe, the detector or IceCube centered version parametrizes the geographic coordinates as a function of the detector zenith. In this case, the up-going flux at  $\theta = 180^\circ$  is calculated using the North Pole atmosphere.

## Decays

Inclusive decay distributions are calculated with `PYTHIA 8` [128] and the tool `PYTHIADECAYS` (section A.5). In contrast to CORSIKA, where only decay

---

<sup>13</sup><http://www.brodo.de/space/nrlmsise/>

<sup>14</sup><https://github.com/DeepHorizons/Python-NRLMSISE-00>

channels up to branching ratios of  $10^{-2}$  are included, PYTHIA knows many of rare branchings. When calculating the distributions for the  $\mathbf{D}$  matrix, all particles from Table 4.2 are set to stable except the decaying one. Therefore, short-lived particles are handled as stable final state.

For example, in the decay process  $\eta'(958) \rightarrow \pi^+ \pi^- \eta$ , the  $\eta$  is a stable particle. Its prompt decay into other secondaries is handled with the chained decay scheme in MCEQ. This procedure simplifies the algorithm, which assembles the  $\mathbf{D}$  matrix, because every particle is treated in exactly the same way. Another advantage of managing chained decays in MCEQ rather than PYTHIA is the statistical error. Taking the above example, the inclusive chained decay of  $\eta' \rightarrow \eta + X \rightarrow \mu^+ \mu^- + X$  would have only the statistics of  $N_{\text{trials},\eta'} \times BR(\eta' \rightarrow \eta) \times BR(\eta \rightarrow \mu^+ \mu^-)$  if calculated in PYTHIA with  $\eta$  defined as unstable.

A further advantage is related to break-down studies of individual contributions from each particle species (see results in 5.2). The decay couplings can be copied into so-called observer or alias groups. The flux vector contains several additional "alias" labels for leptons, marked by the prefix `obs_`, i.e. `obs_numu`, `obs_antinutau` etc. The sub-matrices for these observer groups are identical copies of the original decay sub-matrices

$$\mathbf{D}_{h \rightarrow l_{\text{obs}}} = \mathbf{D}_{h \rightarrow l} \quad (4.4)$$

In the configuration file one can define hadrons, of which the leptonic decay products are scored in this observer category in addition to the original final state particle. This way of scoring allows to trace the contribution of every single meson, baryon and resonance to the flux of leptons.

# Chapter 5

## Atmospheric lepton calculations

After having introduced the MCEQ code and the calculation methods, this chapter is aiming to highlight some of the results.

### 5.1 Comparison with Monte Carlo and iterative solutions

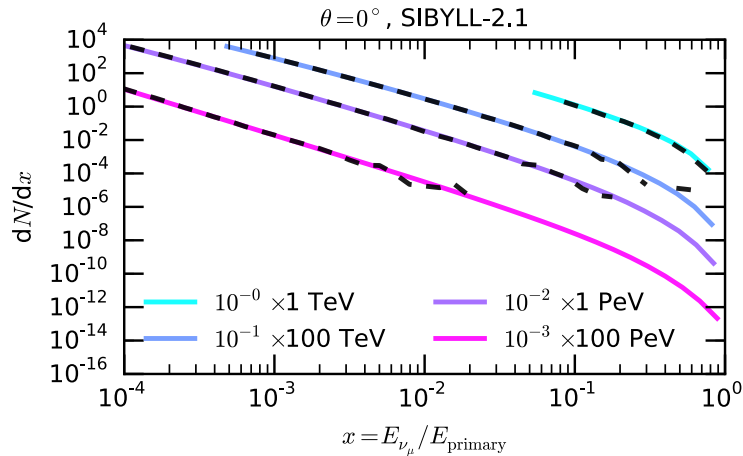


Figure 5.1: Muon neutrino yield as a function of the primary hadron's energy fraction carried by the neutrino at the surface. The calculation is for vertical shower trajectory and SIBYLL-2.1. The dashed lines are obtained from a full CORSIKA Monte Carlo and the colored lines from MCEQ.

The comparison with a full Monte Carlo calculations allows to estimate the method's precision. In a previous work with CORSIKA [62], a full air-shower simulation ran for several thousands of times for discrete energy points. The lepton numbers at the surface were scored in histograms and then appropriately re-weighted to obtain a flux. Figure 5.1 compares the "raw" particle yield at the surface with the calculation using the matrix method in MCEQ. At lower  $x$ , the two distinct methods match excellently. At higher  $x$  the Monte Carlo runs out of statistics, because the pions and kaons at these energies interact

more often with air in flight and do not decay into leptons. This is one of the reasons why an air-shower Monte Carlo is inefficient at very high energies. Decay biasing techniques have been employed to improve this point, but the soft secondary meson distributions (see Figure 2.9) will require a high number of trials anyways. Biasing event generators in  $x_F$  is currently not possible or foreseen. Other techniques, such as particle stack re-ordering and "importance sampling" can improve the efficiency<sup>15</sup>, but only to a certain degree. It should be clear that Monte Carlo simulations can not compete with the performance of an efficient numerical solver in inclusive flux calculations.

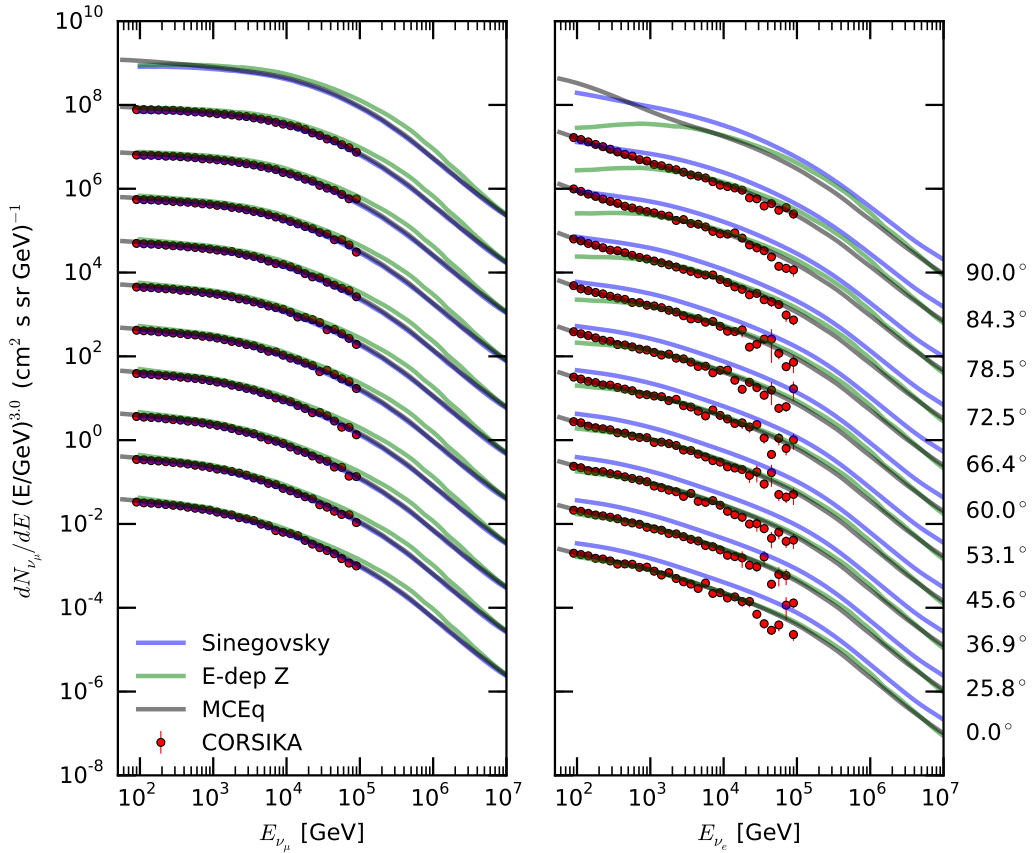


Figure 5.2: Comparison between four calculation methods using the same combination of interaction model, atmosphere, zenith angle and primary flux. "CORSIKA" and "E-dep Z" are from the previous Monte Carlo calculation [62] and "Sinegovsky" is from [123]. On the right is the flux of  $\nu_\mu + \bar{\nu}_\mu$  and  $\nu_e + \bar{\nu}_e$  on the left hand side.

Figure 5.2 compares the solutions from MCEQ with other calculations using an identical set of physical models, i.e. QGSJET-II-03 for hadronic interactions, H3a primary flux, and US Standard atmosphere. For muon neutrinos the different methods agree very well, with the exception of the energy-dependent Z-factor method. The semi-analytical calculation predicts a result which is up

---

<sup>15</sup>See Kyle Jero's talk at MANTS 2015 <https://indico.cern.ch/event/395631/>

to 15% higher, in particular in the interpolation region between the low and high energy solutions (see section 2.1.1). Electron neutrinos are a factor 10 less abundant in air-showers as muon-neutrinos. The CORSIKA calculation runs therefore out of statistics at higher energies, but it matches the MCEQ calculation very well at lower energies. The energy-dependent Z-factor method does not contain the terms for muon decay, visible the large disagreement at lower energies and higher inclination. The prediction by Sinegovskaya is higher. This is related to a different derivation of the form factors for the 3-body decays of  $K_L^0$ , which were obtained from [105].

As a conclusion, we can note that the agreement between a full Monte Carlo method and the method in MCEQ is excellent. The iterative method by Sinegovskaya et al. also achieves similar results. The traditional semi-analytical method with energy-dependent Z-factors adds another (unnecessary) 15% error. The advantage of MCEQ is surely the computing time and the flexibility to exchange models and parameters. The CORSIKA method takes between 10-100 kCPUh, the iterative method at around 50 CPUh<sup>16</sup> and MCEQ a few seconds.

## 5.2 Which particles matter in lepton production?

The matrix method allows to calculate the contribution of each particle species in the cascade to the total flux of atmospheric leptons. The conventional flux at lower energies has been often studied in the past and it is known since half a century that these leptons originate mostly from pion and kaon decays. At higher energies it is not simple to obtain reasonable predictions, because of the lack of experimental data and, on the other hand, because other calculation methods become complicated if more particles are included.

This study uses one of the recent release candidates (RC3a) of the SIBYLL-2.3 hadronic interaction model. During the whole development cycle, the model was compared with other inclusive lepton calculations and high-precision muon data, in addition to the usual fixed-target and collider observations.

The "labels" in the figures below are assigned to the fraction of leptons, which are created in direct decays of this particular mother particle. Throughout the section, prompt contributions are those coming from decays of particles with a critical energy (Eq. (2.7))  $\epsilon \geq \epsilon(D^+)$ , the most long-lived charmed particle.  $K_S^0$  is in this scheme a conventional mother particle. The "other" categories sum together all particles which rarely decays into leptons. The primary cosmic-ray flux model is fixed to a simple broken-power law from [138] with a knee. Although it does not well represent the cosmic ray flux measurements, it resembles its general properties and its smoothness simplifies viewing the multitude of lines in each plot.

---

<sup>16</sup>Personal communication with S. Sinegovsky

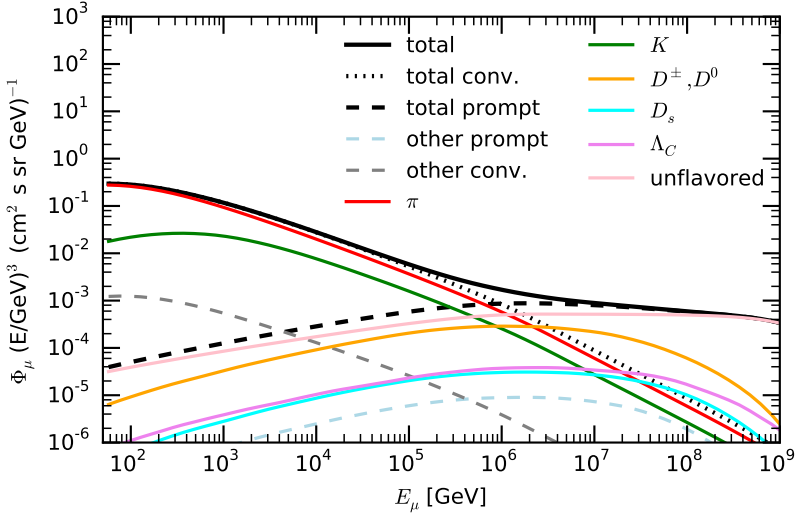


Figure 5.3: Muon ( $\mu^+ + \mu^-$ ) flux, split up into individual contributions of mother particles.

Figure 5.3 shows the different contributions to the total muon flux. It is properly accounted for chained or resonance decays. The conventional flux is clearly dominated by pion decays. Kaon decays play a secondary role, since a smaller fraction of the meson's energy is attributed to the muon (see also Figure 2.4). At energies above a PeV, decays of light unflavored mesons take the lead. A further break-down into contributions from these mesons is shown

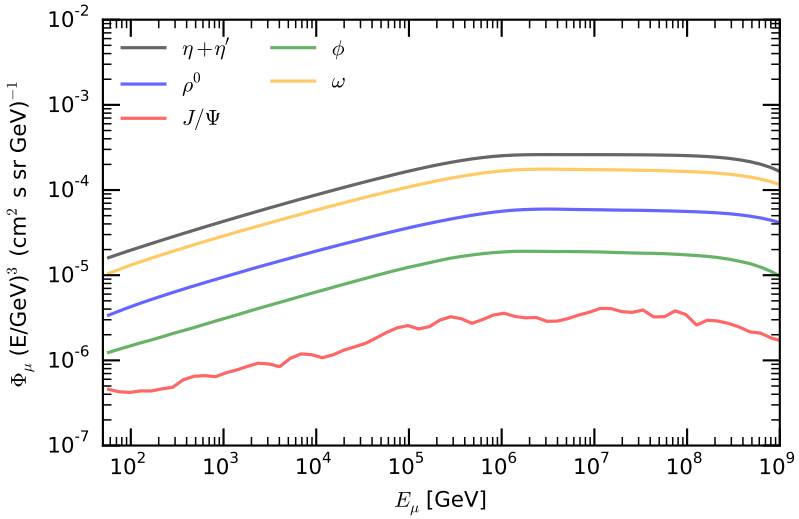


Figure 5.4: Detailed view into the unflavored component of prompt muons.

in Figure 5.4. Those muons are mostly created in decays of  $\eta$ ,  $\rho^0$  and  $\phi$ , which have small branching ratios  $< \mathcal{O}(10^{-4})$  into muon pairs. This unflavored component has been explored by the authors of [83]. Although the decay is

rare, the higher abundance of those mesons in particle production results in a higher flux compared to charmed  $D^0$  and  $D^\pm$  mesons. Worth to note is the attenuation of the prompt component from charmed particles above 10 PeV due to interactions with air. Charmed baryons play a sub-leading role and contribute a factor ten less.

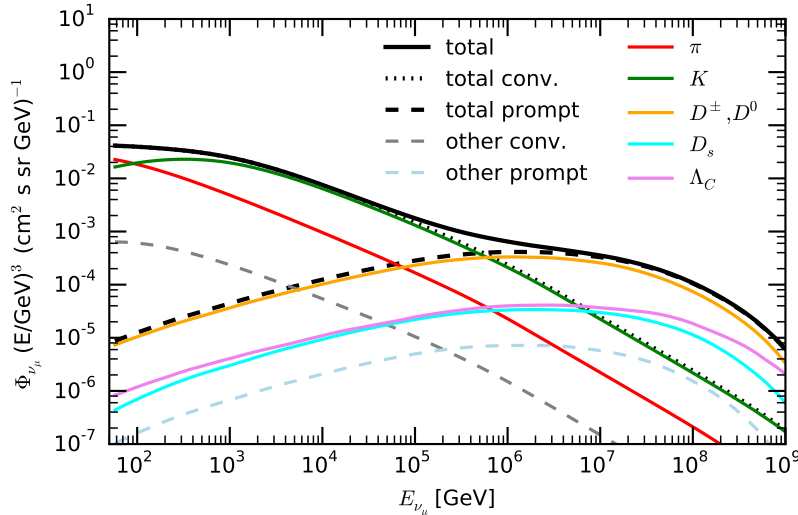


Figure 5.5: Muon neutrino ( $\nu_\mu + \bar{\nu}_\mu$ ) flux, split up into individual contributions of mother particles.

Conventional muon neutrinos (Figure 5.5) at high energies are originating mostly from 2- and 3-body decays of  $K^\pm$  and to a very small fraction from  $K_L^0$  decays (included in "other conv."). Prompt fluxes are dominated by  $D$  meson decays. Prompt baryons play a sub-leading role.

Electron neutrinos (Figure 5.6) have the most complex structure of mother particles. Up to a few hundreds GeV they come from 3-body decays of  $K^\pm$ ,  $K_L^0$  and  $\mu^\pm$ . The muon decay component is roughly one power steeper, because this tertiary decay implies that the mothers of the muons decayed at much higher energies, where they experienced attenuation due to interactions. The authors of [68] found it worth to highlight the role of  $K_S^0$  decays to the conventional electron neutrino flux (brown line). However, when considering even the lowest model for charm production, this contribution is roughly 10-100 times smaller than the prompt flux. At energies above hundreds of TeV the flux of electron and muon neutrinos is roughly equal due to the similar branching ratios of charmed mesons into both neutrino flavors.

The flux of tau neutrinos has the simplest structure because there is no conventional component and each  $\tau$  neutrino is created in association with a heavy tau lepton or in decays of  $\tau$ . Nonetheless it is worth to point out, that the highest contribution to the flux does not come from the decay  $D_s \rightarrow \tau \nu_\tau$  but from the subsequent chained decay  $\tau \rightarrow l \nu_l \bar{\nu}_\tau$ . In this last decay the  $\tau$  neutrino obtains a large fraction of the  $\tau$  lepton's energy, more than what it directly gets in decays of  $D_s$ .

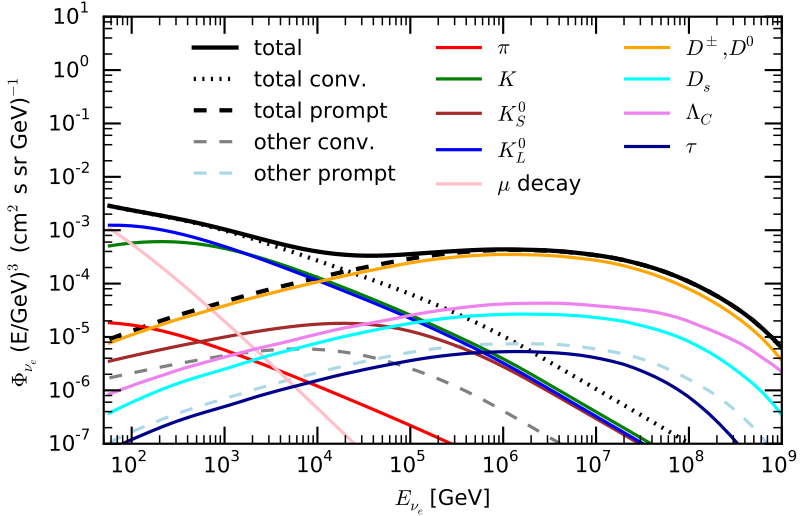


Figure 5.6: Electron neutrino ( $\nu_e + \bar{\nu}_e$ ) flux, split up into individual contributions of mother particles.

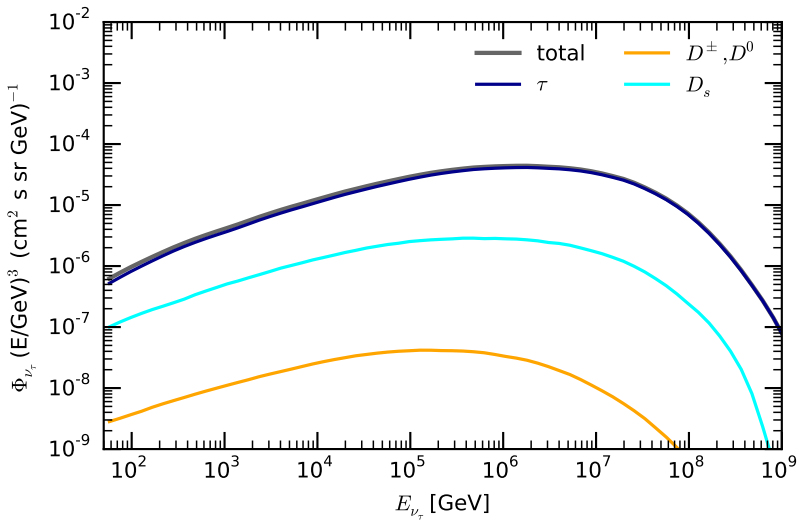


Figure 5.7: Tau neutrino ( $\nu_\tau + \bar{\nu}_\tau$ ) flux, split up into individual contributions of mother particles.

### 5.3 Studying hadronic interactions through cosmic ray observations

Inclusive fluxes of atmospheric muons were measured by many experiments at different depths, energy ranges and angles. As straight forward as it seems, these measurements are not as simple as one might expect. Many uncertainties have to be taken into account, like the composition of the overburden rock and the estimation of the muons' energy at the surface, instead of at the location of the detector. The spectrometric momentum measurement, especially at

high energies, requires high magnetic fields for bending the track by at least a small amount. The granularity of segmented or pixel detectors often limits the acceptance to energies around a few TeV.

In order to not "tune" a model to inconsistent data, we restrict ourselves to measurements from the last two decades, in particular the cosmic muon analyses by L3+c at CERN [12], the MINOS experiment near Fermilab [13], OPERA at the Gran Sasso laboratory [16] and CMS [132]. An extensive comparison between calculations and data can be found, for example, in [93].

Two observables are of special interest, the unfolded inclusive flux of muons at the surface and the muon charge ratio between tens of GeV and 10 TeV. The flux carries the information about pion and kaon production at higher  $x_F$ , while the muon charge ratio is a measure for the relative abundance of kaons relative to pions. This is motivated through the different charge ratios of pions and kaons, when produced in the projectile fragmentation region.

### 5.3.1 Phase-space

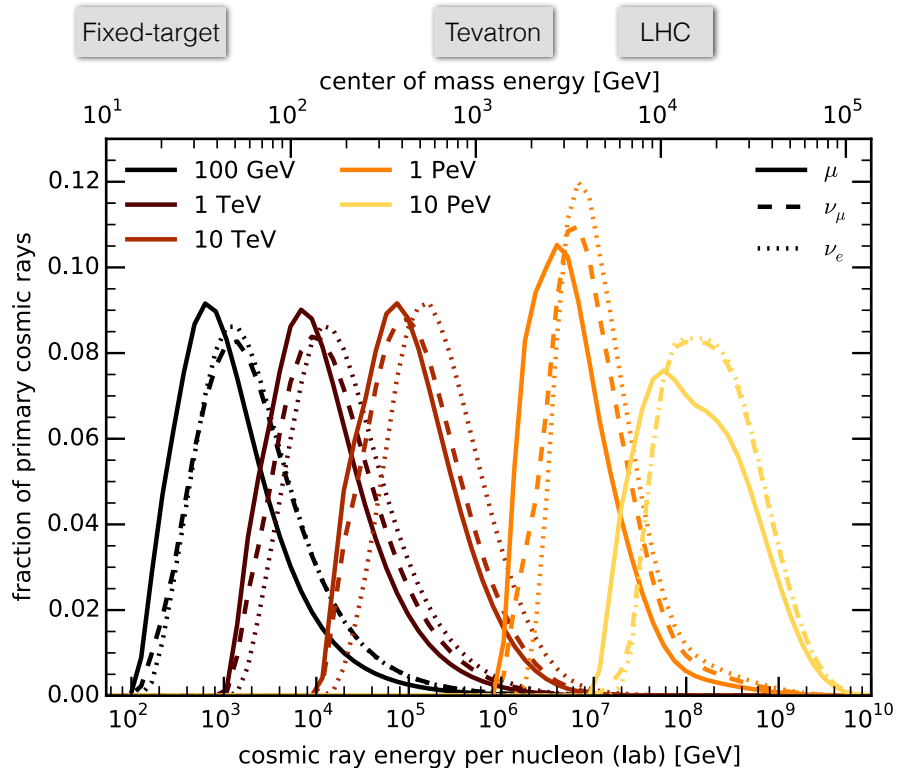


Figure 5.8: Distribution of primary cosmic ray nucleons, responsible for the production of leptons at discrete energy points, computed for H3a primary flux and SIBYLL-2.3.

First, let us evaluate at which primary interaction energies of cosmic rays with air nuclei we are looking at, when studying muons of a certain energy. These so called response functions are drawn in Figure 5.8. Muons at 100 GeV are mostly produced in interactions of 600 GeV cosmic rays with a long tail

up to PeV energies. Due to the less efficient decays, 100 GeV neutrinos are produced in interactions of TeV cosmic rays and require on average a twice as high primary energy. The upper x-axis relates the primary energies to equivalent center of mass energies and accelerator generations. Fixed-target experiments do not cover the relevant phase-space for muon and neutrino production at these energies. Colliders like the Tevatron at Fermilab and the LHC run at very high energies, which in the atmosphere are dominated by prompt fluxes. Unfortunately, the experiments at colliders are not instrumented in the small-angle scattering phase-space which is important for lepton production.

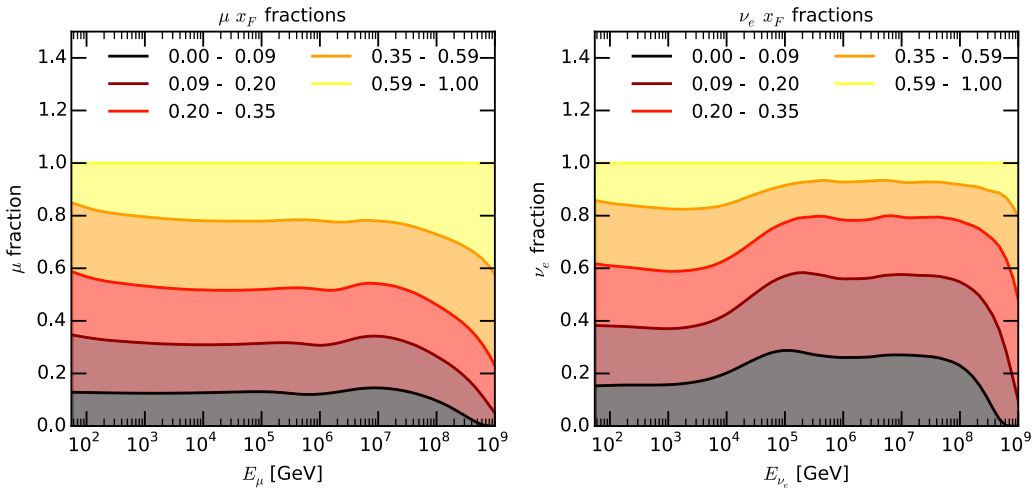


Figure 5.9: Feynman  $x_F$  ranges contributing to the inclusive flux of muons (left) and electron neutrinos (right).

By slicing the particle production matrices  $\mathbf{C}_{h \rightarrow l}$  in  $x_L$  or  $x_F$ , it is possible to study the relevance of phase-space regions for inclusive lepton production by calculating the fractional contribution of each slice to the total lepton flux. In Figure 5.9 the  $x_F$  cut is applied to all interaction products simultaneously. It is also possible to study cuts on individual hadron species independently, but for more clarity the current approach should be sufficient. In case of muons, which are dominated by pion, kaon and unflavored meson decay at all energies, more than 40% of inclusive leptons originate from mesons which have been produced at  $x_F > 0.4$ . The experimental techniques to study scattering at such high  $p_{\parallel}$  are only possible at fixed-target experiments. Because the beam-pipe at colliders has a certain extension, it is very difficult if not impossible to install detectors in locations where these particles can be measured. At the LHC the roman-pot experiments TOTEM and ALFA are only sensitive to (differently or elastically scattered) protons. The forward calorimeter LHCf only measures neutral particles ( $n$  and  $\gamma$ ). Very forward pion or kaon distributions are unknown at these energies, since the other detectors cover only a phase-space at roughly  $x_F < 0.1$ . These arguments are also valid for other colliders.

Therefore, by comparing our predictions with high-precision atmospheric

muon measurements, we are, in fact, sensitive to a yet unexplored phase-space and can adjust the interaction models accordingly.

### 5.3.2 Comparison with high-precision measurements of atmospheric muons

In Figure 5.10 MCEQ calculations are projected against the recent muon flux and muon charge ratio measurements. In the upper figure the primary model is fixed and the interaction model is varied. SIBYLL-2.1 does a remarkably well muon flux prediction, despite the disagreement in the charge ratio. This disagreement is related to a programming feature or bug, where too many  $K^+$  are produced in nuclear interactions. Therefore, one should avoid interpreting the result to strictly. The RC3a version of SIBYLL-2.3 describes the flux and the charge ratio reasonably good. Being one of numerous development versions, it describes the combination atmospheric muon flux together with its charge ratios best. There is a certain level of mismatch of the spectral shape, which can not only be attributed to the primary model.

One has to take into account, that during development the model is exclusively compared to fixed-target and collider observations, but not to higher-level observables like inclusive fluxes or  $X_{\max}$  distributions. It is therefore a great success, that a high-energy particle physics and cosmic ray model extrapolates to higher energies with such a precision. FLUKA has been found to reproduce the muon flux better [103], but the hadronic interaction model which is employed in this calculation does not work up to very-high energies. SIBYLL is at the primary energies not far away from QGSJET-II-04 gives a similar flux prediction but a wrong charge ratio. The results of DPMJET-III were omitted in the figures, since it produces a roughly 30% smaller flux and would reduce the graphical clarity. The reasons for this behavior are still under investigation.

The influence of the primary model is studied in the bottom panel of Figure 5.10. H3a and GST do not differ much, what should not come as a surprise since they are based on the same satellite datasets below the knee. The older GH model has a better description of cosmic ray data below  $\sim 1$  TeV, but the recently observed hardening of proton and helium spectra are not properly modeled (see section 2.5 for more information). In this model the power-law spectra are not broken at higher energies and it indeed shows a worse description of muon data. This fact can be seen as an additional indirect confirmation of the satellite observations.

### 5.3.3 What do we learn about hadronic interactions?

The method in the previous section compares (plain) predictions with muon measurements, where we designed and tuned hadronic interaction models to accelerators and then compared their predictions with muon data, with the aim to accept or discard a version. Sometimes this method yields simple

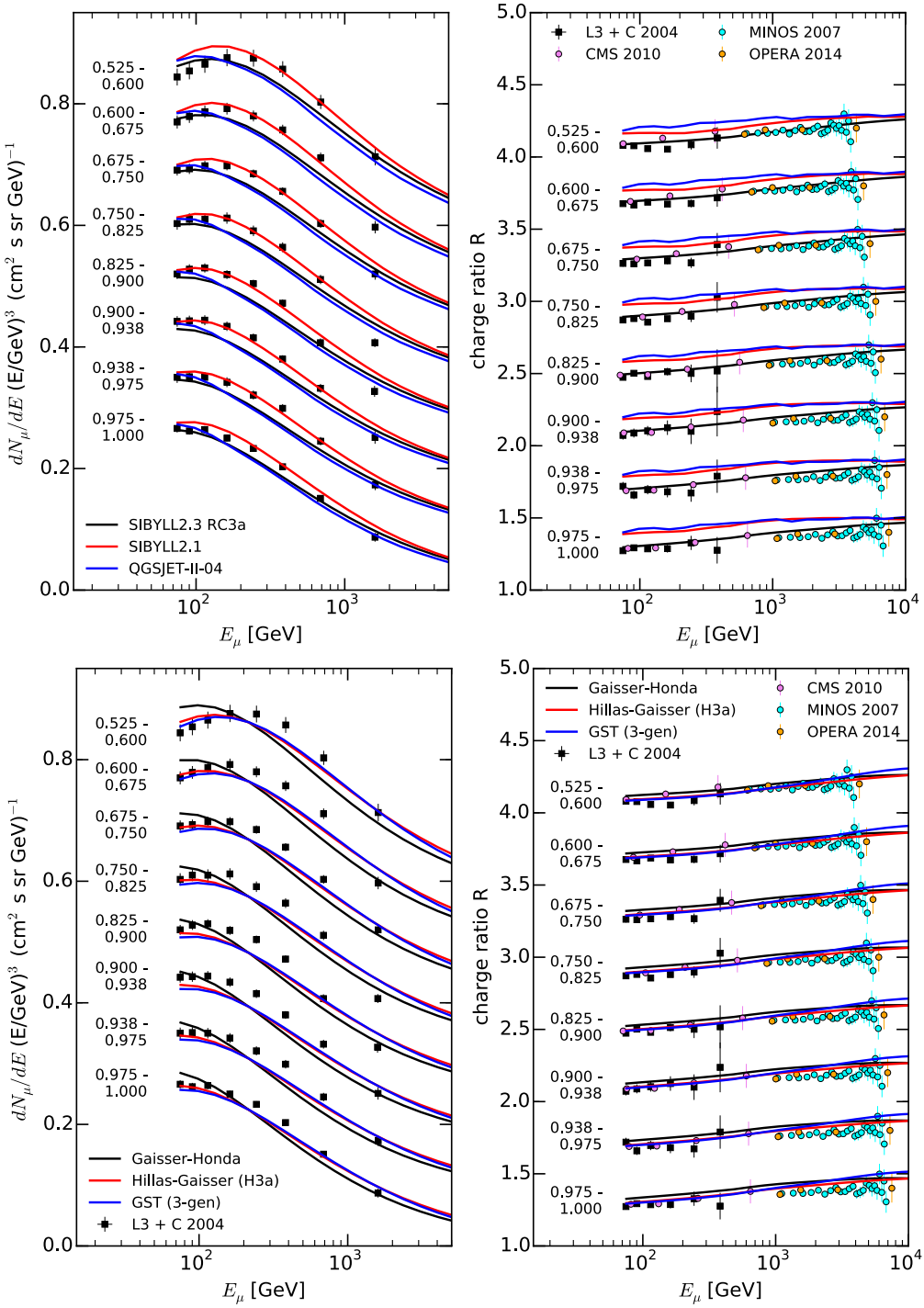


Figure 5.10: Atmospheric muon measurements vs MCEQ for different interaction models and H3a primary model (top) or for different primary flux models and SIBYLL-2.3 (bottom). Zenith bins in  $\cos \theta$  are given on the right hand side of each line with an offset of 0.08 for the flux in its units and 0.4 for the ratio. Data from [12, 13, 16, 132].

quantitative information, such as "too low" or "too high". This is already some sort of feedback. So, how can we improve the detail of this feedback such that it can be interpreted in terms of corrections for successor versions?

Let us take the previous combination of muon flux and charge ratio measurements in different angular and energy bins. The flux mostly resembles the charged pion production at high  $x_F$ . The angular binning at high energies is sensitive to the relative abundance of kaons with respect to pions ( $\pi/K$  ratio), because in more inclined showers pions are less attenuated due to the elongated density gradient, resulting in a higher contribution to muon production compared to vertical directions. And finally, the muon charge ratio, measured in angular bins, is below  $\sim 300$  GeV sensitive to the charge ratio of pions and above  $\sim 1$  TeV to the charge ratio of kaons in the projectile fragmentation zone.

By studying the correlations between these "channels" using minimization or Likelihood techniques, it should be possible to constrain inclusive particle production cross-sections and possibly their differential shapes. Adding atmospheric muon and electron neutrino measurements from large-volume neutrino telescopes, could constrain charged and neutral kaon production in addition. This technique is one of the few, if not the only one, which is sensitive to forward particle production at very high energies.

Previous theoretical frameworks were not capable to support such studies due to their simplifications. Semi-analytical calculations model particle production with a single number, the Z-factor, which can yield a scalar correction for the entire  $x_F$  range and dependent on the interaction model. In addition the approximations used to describe the atmosphere, propagation or secondary particle production introduce sources of uncertainties, which would smear out the results and make the studies questionable. Monte Carlo calculations are capable to model most of the details and reduce systematic uncertainties. But the requirements on computational time are too high for using template methods or other sophisticated unfolding techniques. On the other hand, MCEQ is precise and very fast. It can be used to produce thousands of predictions with parameter variations within a few hours.

The following case study has the goal to illustrate how simple it can be to feed back into interaction model development. Similar to studies carried out by experiments, like the pi-K model in MINOS [13], we attach a variable (fudge) factor to each partial flux originating from decays of positively and negatively charged pions and kaons, respectively. These factors are allowed to float during a minimization to the above mentioned datasets. One caveat is that all datasets, except L3+c, are either not unfolded individually for each angular bin or, if the unfolding has been performed, the data is not provided publicly in tables. Therefore the simple  $E_\mu \cos(\theta^*)$  parameterization is used for the angular dependence, which is based on the planar approximation in semi-analytical solutions. It should perform relatively well with respect to the covered range up to  $\theta < 56^\circ$ .

By fixing the primary model to either H3a or GST-3 and the interaction

model to SIBYLL-2.3 RC3a, the flux is computed for all angular bins and interpolated at energies of each experimental data point. Minuit<sup>17</sup> is used to minimize the global  $\chi^2$ . Table 5.1 contains the correction factors and Figure

Table 5.1: Table of correction factors obtained from global muon flux minimization.

primary flux model	$f_{\pi^+}$	$f_{\pi^-}$	$f_{K^+}$	$f_{K^-}$
H3a	+0.7%	+2.2%	+24.9%	+46.0%
GST-3	+5.6%	+6.1%	-2.8%	+7.7%

5.11 the graphical result for H3a.

The results are encouraging. There is some ambiguity between the primary models. The GST-3 model suggest to increase pion production by a few percent and keep kaon production at the same level, increasing only a bit the kaon charge ratio. But when using H3a the fit suggest to keep the pion production at the same level and increase kaon production significantly, but also with a small reducing charge ratio.

There is still some tension between the adjusted prediction and data, which should not come as a surprise. One one hand, the simple rescaling of partial fluxes at the surface, and not the differential production cross-sections, is not sophisticated enough. It can be also the shape (hardness) of the production spectrum and instead of the inclusive cross-section which needs adjustment. On the other hand, the muon charge ratio measurement at high energy is not available for separate angular bins and be therefore not precise enough. Note, that energy is not strictly conserved in this exercise. What one can hope to extract in a more complex analysis is guidance for the model parameters.

Let us now see, if we can recognize these "suggestions" by comparing with measurements at accelerators. In Figure 5.12 distributions obtained with the RC3a version of SIBYLL-2.3 are compared with differential cross-section measurements for charged pions and kaons. NA49 has also taken proton-carbon data, but it does not include kaon distributions and is limited to smaller  $x_F$ . The projectile fragmentation zone at high  $x_F$  will be mostly populated by mesons from interactions, which involve one or few target nucleons. Therefore comparisons with  $pp$  data are legitimate. SIBYLL describes the data remarkably well, given that the physics in the shown phase-space is mostly non-perturbative.

When comparing the correction factors in Table 5.1 obtained from the fit, we can acknowledge that the pion distributions do not need much adjustment. The acceptance of NA49 for kaons is much smaller ( $x_F < 0.5$ ) when compared to pions ( $x_F < 0.9$ ). Nonetheless, the suggested corrections by tens of percent upwards are reasonable. In particular the underproduction of  $K^-$  is clearly apparent.

Since we have compared to fixed-target collisions at 149 GeV, we can infer

---

<sup>17</sup>Original source <http://www.cern.ch/minuit>

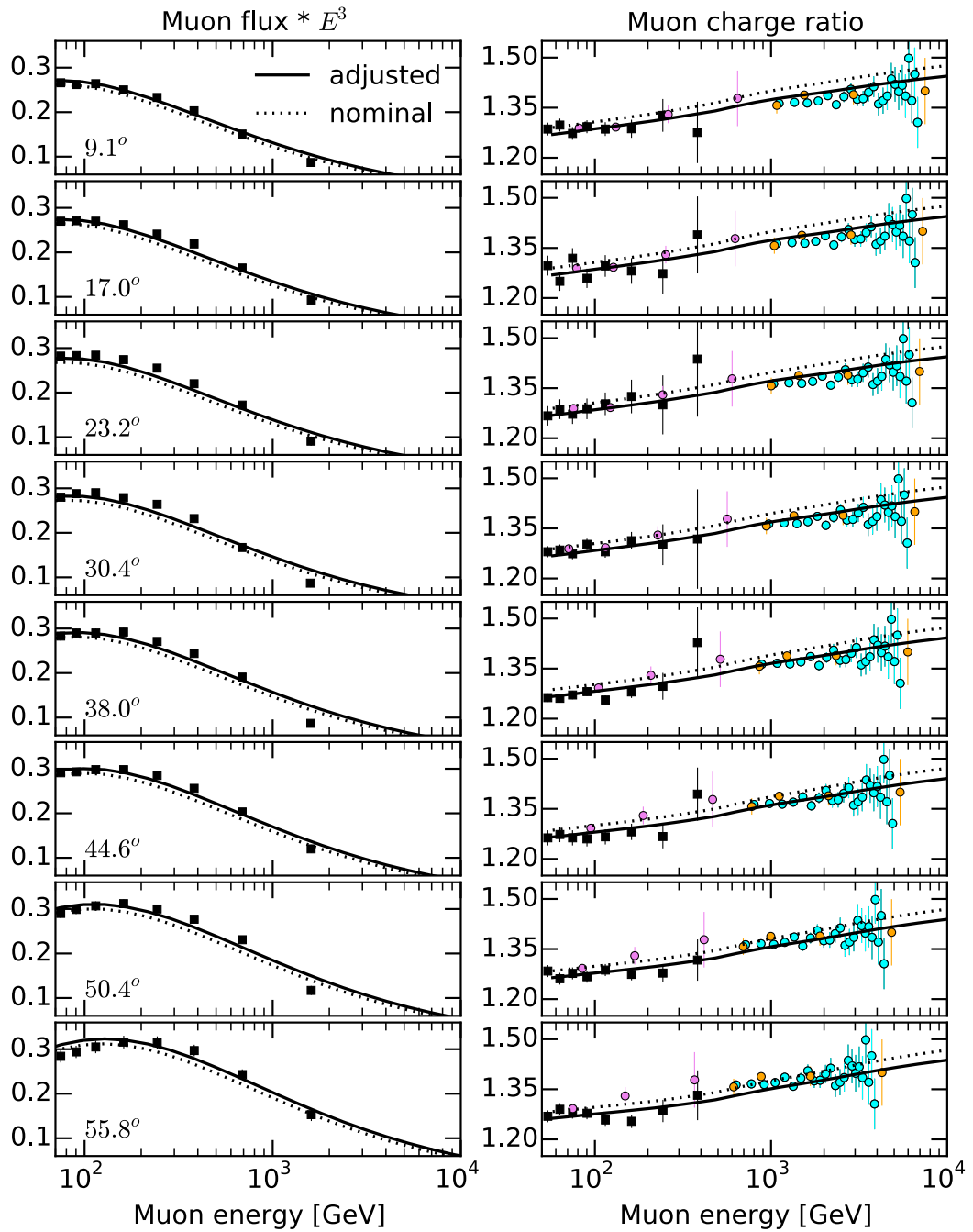


Figure 5.11: Global minimization to all shown data points, which are explained in the legend of Figure. The figure shows the result for the H3a primary model. 5.10.

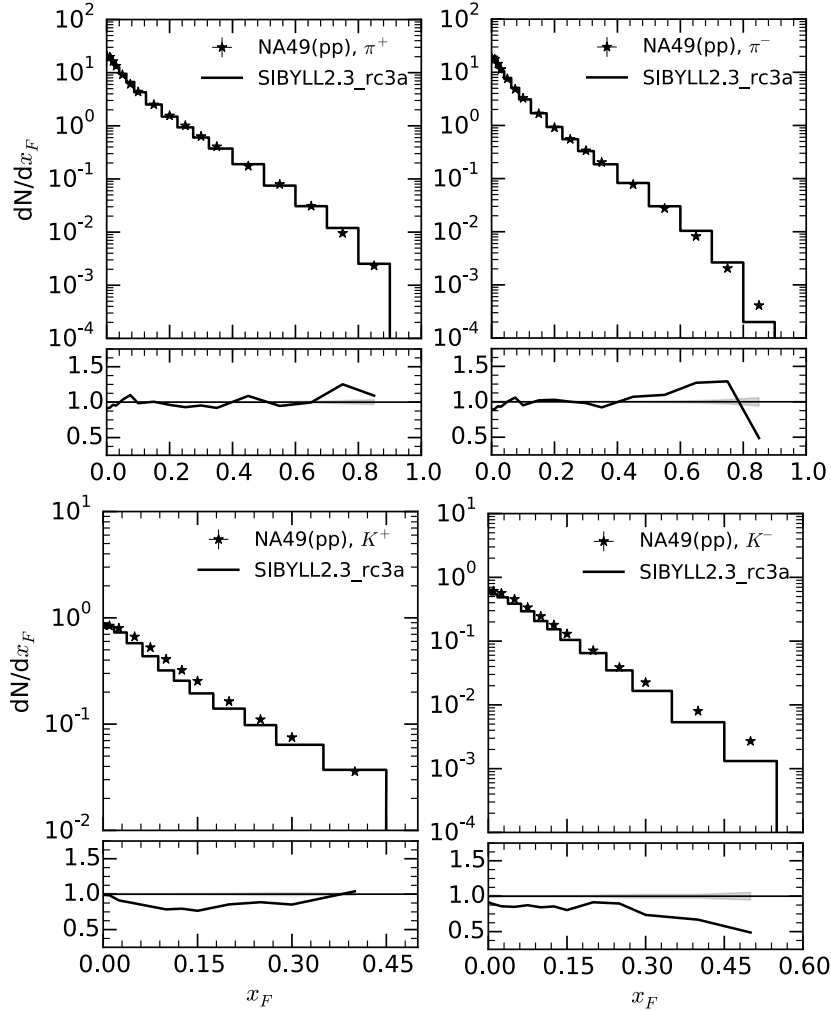


Figure 5.12: SIBYLL-2.3 RC3a compared with fixed-target data from NA49 [135, 134] in  $pp$  collisions. The small ("delta") panels under each plot show Monte Carlo divided by data, including the thin shaded error bands. The errors are included but they are smaller than the markers.

confirming arguments for Feynman scaling. Recall that the muon measurements are sensitive to a much higher primary interaction energy. This proof of concept and similar studies showed that by tuning the interaction model at low energies, we can indeed improve the description of muon data at higher energies.

I hope that by providing the tools and inspiration to experiments which are sensitive to atmospheric muons, they feel more encouraged to take and unfold high precision data with the aim to analyze and constraint non-perturbative physics of interaction models in a phase-space which is unaccessible to colliders.

## 5.4 The effect of the atmosphere on inclusive leptons

The knowledge about the influence of atmospheric variations on the flux of leptons is currently an active topic in neutrino oscillations research. Recent underground neutrino detectors and large volume neutrino observatories can determine some of the remaining oscillation parameters. IceCube has already demonstrated its sensitivity to neutrino oscillations [8, 7] by measuring muon neutrino disappearance. However, these methods need a careful evaluation of all systematic uncertainties in order to be competitive with accelerator based measurements.

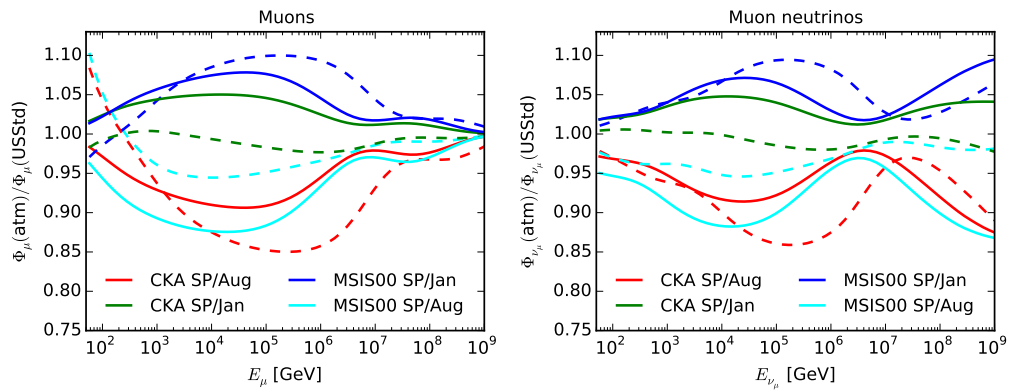


Figure 5.13: Seasonal variations of the muon (left) and muon neutrino (right) spectrum for January and August at the South Pole. CKA are parameterizations from CORSIKA and MSIS00 curves are obtained with the NRLMSISE-00 model. Solid lines are for vertical and dashed for horizontal zenith angles.

A large but controllable uncertainty is related to the modulation of the flux due to the atmosphere. At lower, Super-Kamiokande range, energies the atmosphere plays a secondary role, since the meson cascade seldom becomes interaction dominated, or in other words pions and kaons decay below their critical energy. Therefore, perturbations or changes to the atmospheric density rarely influence the flux of atmospheric neutrinos. Above 100 GeV the situation is very different. Figure 5.13 demonstrates the influence of seasonal variations of the atmosphere above the South Pole on the spectrum of muons and neutrinos. The flux varies up to  $\pm 15\%$  which is significant for an uncertainty which can be precisely taken into account through modeling. A group inside the IceCube Collaboration used MCEQ to estimate systematic uncertainties of their sterile neutrino analysis [86]. They interfaced the program with observations from the AIRS/AQUA satellite to get a precise estimate of the variations during the detector life-time.

In fact, this capability of MCEQ to use arbitrary atmospheric profiles is a unique feature. Section 2.2.2 describes more details of the implementation using splines. Semi-analytical or iterative methods could not be used in the

past. Monte Carlo calculations are too slow. Programs like CONEX should in theory be capable to allow such studies. But it is neither documented, nor published. But as a part of CORSIKA one can expect it to have a Linsley type parameterization.

MCEQ opens also new ways for specialized studies of atmospheric variations of the muon rate in IceCube [139, 53] and MINOS [14, 74], where the aim is to disentangle the pion, kaon and prompt components individually. In the current approach the modulation of the flux is attributed to the variation of an effective temperature  $T_{\text{eff}}$ , the first moment of the muon production spectrum with respect to  $T(X)$ . One hopes that by computing a correlation coefficient between flux and temperature variations, it is possible to measure the relative abundance of kaons with respect to pions. The current status is that, although this procedure works, the results are not consistent between spring and autumn gradients.

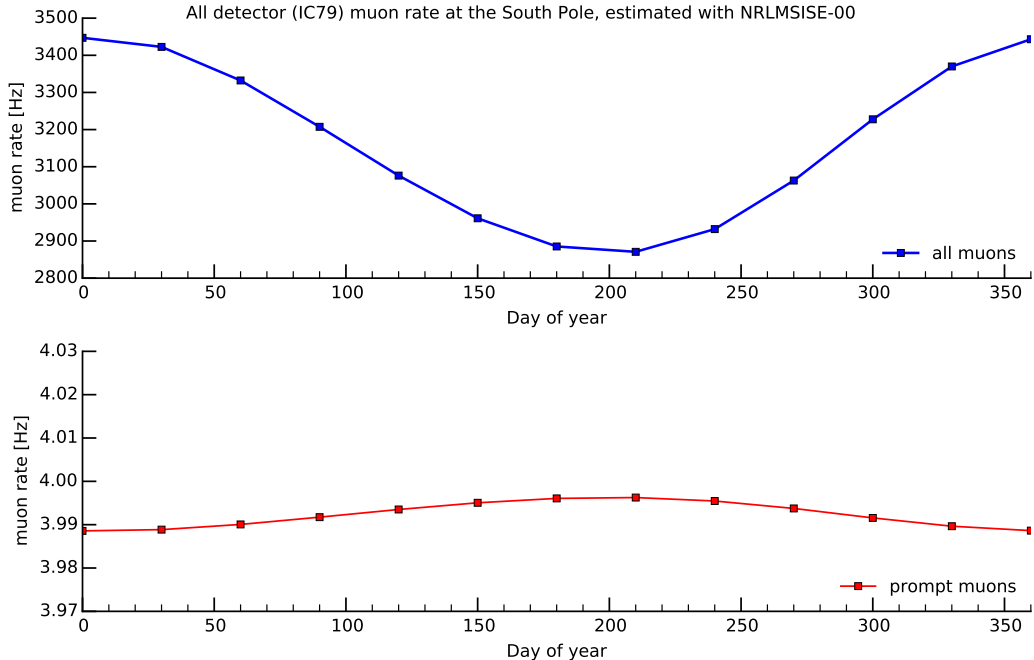


Figure 5.14: Single muon rate in IceCube, computed with effective area from the IC79 configuration.

MCEQ allows a different approach by computing directly the flux of muons with the daily observations from AIRS satellites and by correlating it with the trigger rates. One caveat is, that the trigger rate is proportional to the rate of muon bundles instead of the rate of single muons. The single muon rate, computed using muon effective areas from the 79-string (IC79) configuration of IceCube is located in Figure 5.14. The muon rate shows the expected variation of  $\pm 10\%$ . Prompt muons have a very small dependence  $< 1\%$  on atmospheric variations. Interesting to note that four prompt muons arrive per second in the detector which in principle should be a measurable signal, given some additional signature.

This study is still active research and results will follow in a later publication.

## 5.5 Predictions of conventional and prompt fluxes

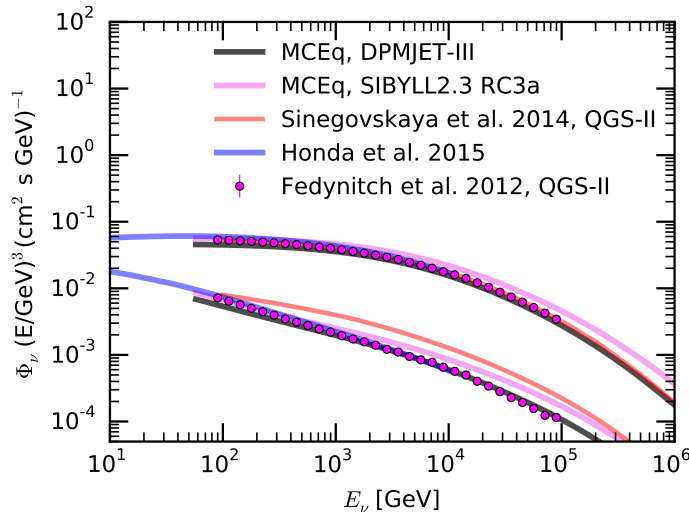


Figure 5.15: Conventional muon neutrino and electron neutrino fluxes, calculated with DPMJET-III, SIBYLL-2.3 RC3a, H3a primary model and US Standard atmosphere.

Fluxes of conventional muon and electron neutrinos are compared with recent calculations in Figure 5.15. Near 100 GeV the calculations match, implying that the "calibration" methods of hadronic interaction models indeed work. In the calculation by Honda [81] a custom version of DPMJET-III was calibrated to high altitude muon data by adjusting the particle production spectra or Z-factors according to high-altitude balloon measurements [80]. Our current development version of DPMJET-III produces a flux, which is lower for both species of neutrinos at lower energies, but it approaches the other models at higher energies, in particular the Honda et al. in the electron neutrino channel. This strongly suggest that the pion contribution is underestimated. This is in agreement with the findings in section 5.3. The Sinegovskaya et al. [123] and our previous Monte Carlo calculation [62] match for muon neutrinos because only the calculation method is different but the ingredients are the same (see section 5.1). The new SIBYLL predicts a slightly harder spectrum. Currently all of the predictions are within experimental uncertainties of IceCube. Recent progress on analysis techniques and increased statistics might yield a better discrimination in near future. For example, SIBYLL-2.1 is already disfavored by data [9].

Regarding prompt fluxes the situation becomes less clear. Figure 5.16 contains some of the modern predictions. The MRS [99] and the ERS [58] are

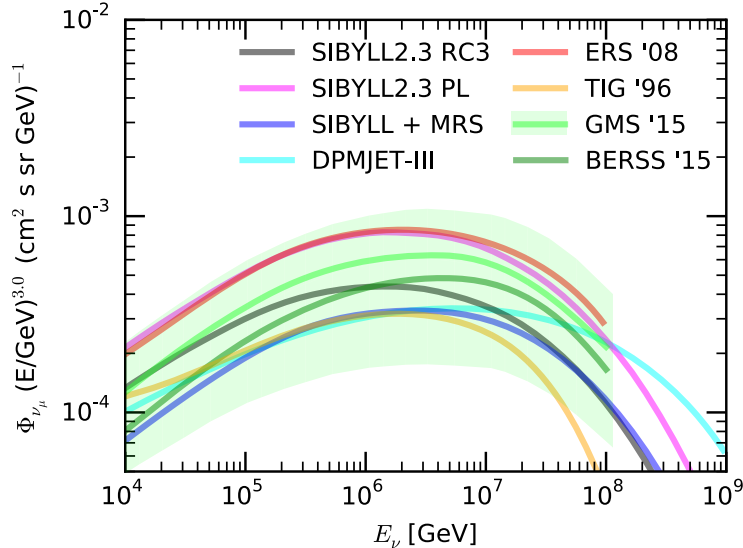


Figure 5.16: Different models of the prompt flux compared with weighted with a simple broken power-law primary spectrum.

both based on the dipole model and consider saturation effects at high energies. The line from TIG [138] is based on a perturbative approach using a version of PYTHIA. BERSS [38] and GMS [70] are NLO perturbative calculations. The latter is using a modern particle physics approach to derive theoretical uncertainties, including errors from parton distribution functions (PDF), factorization and renormalization scale variations. The authors obtain an error band which envelops all of the previous calculations, what should not come as a surprise, because current colliders are not sensitive to this phase-space. The uncertainties arise from unknown low-\$x\$ behavior of gluons in the proton and by how much non-perturbative processes contribute. The latter include the creation of charm quark pairs in fragmentation or remnants [118]. Both, DPMJET-III and SIBYLL-2.3 lie inside this uncertainty band. The charm model in the preliminary version of DPMJET-III shows a different shape, which presumably arises from a different energy behavior of the  $c\bar{c}$  cross-section and a larger contribution of  $\Lambda_C$  baryons that interact at much higher energies compared to  $D$  mesons.

A larger fraction of uncertainty comes from nuclear effects. To assess this uncertainty in a quantitative way, we make the assumption for the  $c\bar{c}$  nuclear modification factor

$$R_{p-air} = \frac{dN_{p-air}^{c\bar{c}}/dp_T}{\langle N_{coll} \rangle dN_{pp}^{c\bar{c}}/dp_T} \equiv 1. \quad (5.1)$$

In other words, there are no screening effects and the production of charmed quarks is a point-like process. Quantitatively this means for the inclusive  $c\bar{c}$  cross-section in proton-air collisions

$$\sigma_{c\bar{c},p-air} = A_{air} \sigma_{c\bar{c},p-p} = 14.5 \sigma_{c\bar{c},p-p}. \quad (5.2)$$

In calculations labeled SIBYLL-2.3 PL (PL for point-like) charm cross sections and inclusive particle spectra are taken from  $pp$  events and scaled according to Eq. (5.1). All of the other calculations use this approach to convert from nucleon-nucleon to nuclear cross-sections. One can say that all of the calculations, including the most recent ones, converge towards a band that is smaller than an order of magnitude.

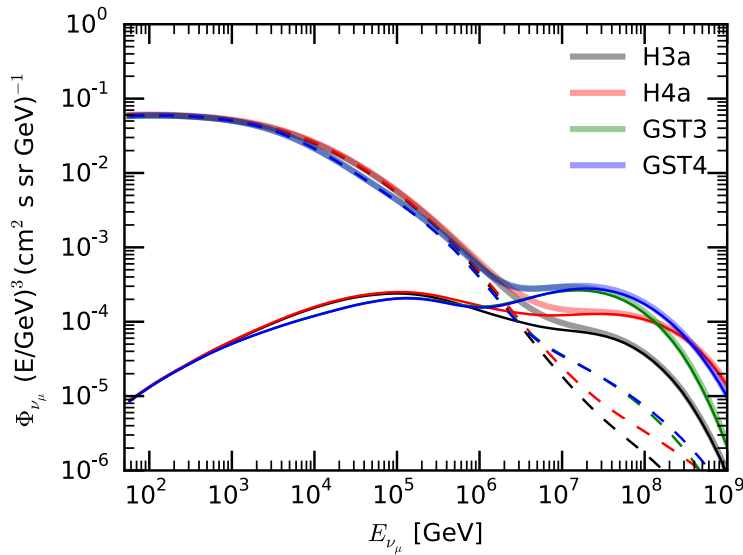


Figure 5.17: Prompt flux, calculated with different composition of cosmic rays beyond the knee. Thick lines show the total flux, dashed the conventional and thin the prompt flux.

An additional source of uncertainty is the primary spectrum, in particular the composition. As mentioned in section 2.2.1, the composition above the ankle is not well known. The models H3a and GST have a version, where at the highest energies the flux is only protons. Protons are more efficient in producing leptons, because the particle energy is not shared across the nucleons. The result, where the light model variants H4a and GST-4 are compared with their heavier counterparts is shown in Figure 5.17.

Both uncertainties, on the charm production and on the composition, are, in fact, of similar size. If at some point the prompt flux will be measured by experiments, one will still have to disentangle the ambiguity with the cosmic ray composition.



## Part II

# Aspects of hadronic interactions



# Chapter 6

## Has the LHC reached the black disk limit?

### 6.1 Introduction

In section 5.5 the hadronic interaction models were identified as one of the largest sources of uncertainty of inclusive flux calculations. Air shower measurements also point to a serious tension between measurement and model predictions [2]. To improve this situation it is not sufficient to just develop fast and precise calculation methods, but also it is crucial to enhance the model description of hadronic interactions at high energies and small scattering angles. One model, which is a very promising candidate for a universal description of minimum-bias and forward physics is DPMJET-III. It has a long history ranging back to the roots of the Dual Parton Model [46] and the analogous Quark-Gluon-String model [87]. Through several evolutionary generations of Monte Carlo programs it arrived at its current state, the nuclear interaction framework DPMJET-III built around the hadron-hadron, photon-hadron and photon-photon interaction model PHOJET. The latest changes to these models, dated to early 2000's, are more than 15 years ago. Since then only minor bug-fixing and adjustments have been performed, leaving the model behind in the Tevatron era.

For leveraging the capabilities of DPMJET-III in air shower simulations and for inclusive flux calculations, essentially two steps are necessary.

1. The cross-sections and minimum-bias distributions have to be validated and re-adjusted against the latest available measurements from the LHC.
2. The Monte Carlo code needs the technical capabilities to run particle cascade simulations up to very high energies and for various projectile-target combinations.

This chapter is about the first point, where minimum-bias measurements point to a deficiency in the description of multiple parton interactions, which are strongly related to the original ideas of the Dual Parton Model. The next

chapter includes more technical topics concerning point 1. and discusses the modifications corresponding to point 2.

## 6.2 Multiplicities at LHC energies

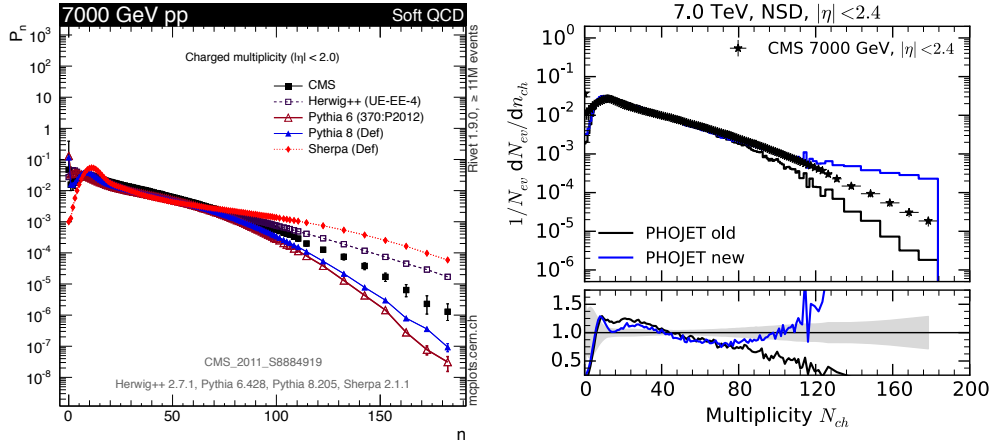


Figure 6.1: Charged-particle multiplicity distributions in  $pp$  collisions at 7 TeV compared to a measurement from CMS [90].

The old version of PHOJET suffered from a the lack of high-multiplicity events. After finding a technical origin of this problem (see section 7.7), the tail of charged particle multiplicity distributions showed a specific curvature at high energies (right panel in Figure 6.1), while at lower energies the distributions stayed normal. Variations of parameters or other tuning efforts modified the generator, but this high-multiplicity tail persisted. Further investigation revealed, that most, if not all, models which are based on an eikonal picture and a two-component pomeron, suffer from similar behavior (left panel of Figure 6.1).

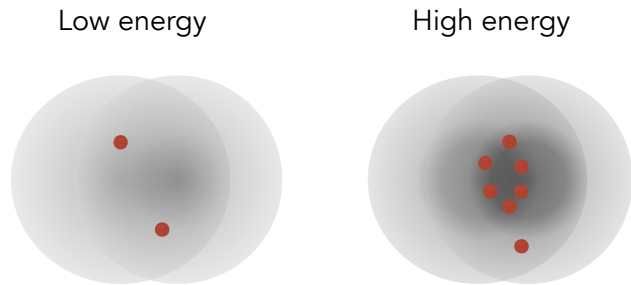


Figure 6.2: Sketch of multiple partonic interactions, viewed from the  $z$ -axis on the transverse impact parameter plane.

The striking difference between collisions at lower energies and the high energies of the LHC is size of the hard cross-section  $\sigma_{QCD}$ , to which the hard component of the pomeron amplitude is normalized. The growth of the hard

cross-section is one of the few ingredients in the model which is perturbatively well understood in QCD. So on one hand the steep growth has to be present in the model and on the other hand, data suggests that the picture of how multiple soft and hard partonic interactions are distributed in impact parameter space is incomplete (see Figure 6.2).

The event generator PHOJET as many other minimum-bias generators, incorporates ideas from Gribov's Regge Field Theory [75], together with a QCD enhanced parton model to form a consistent description of hadronic final states. Details of included practical concepts, the fundamental ideas and their success or failure in the description of observations have been discussed in great detail inside available literature, e.g. [46, 88, 107, 121]. It would be beyond the scope of this work to re-introduce all aspects of a half century of research, even in a short condensed form. Therefore, only a small subset of theoretical background is included in this chapter which is considered as the minimum to understand the motivation and procedure of the following study.

### 6.3 About $S$ -matrix theory and the pomeron

In the 1960's the  $S$ -matrix theory, a relativistic extension of potential scattering theory and the quantum mechanical scattering matrix, prevailed to be a promising approach to understand hadron scattering. Extensive literature has been published on this topic, such as the classic book by Collins [48] and more modern summaries [55, 33]. In fact, the theory became too complicated and never reached its goal to explain all details of hadronic interactions. The objects which it predicted based on its mathematical expressions, such as the leading Pomeranchuk pole or simply the pomeron, could not be unambiguously associated with observations of microscopic matter, the partons. It would be wrong to say, that there is no fundamental description or at least an imagination of what the pomeron is, since later, the BFKL pomeron has been theoretical explored by Lipatov [96] and other authors in perturbative QCD as a series of gluon ladders. However, the energy behavior of this BFKL pomeron was found to be sufficiently steeper with an intercept of around  $s^{0.3}$  rather than  $s^{0.08}$  as observed from cross-section measurements at colliders. So, either this object is not the same pomeron and there are multiple types, or it is the same one but the "bare" intercept is screened by non-perturbative corrections and appears therefore softer.

However it is still to early to give up and label this direction as wrong. Except the achievements during the  $S$ -matrix campaign of the last century, such as the Regge theory and the relativistic field-theoretical extension by Gribov, the Gribov-Regge Field Theory (GRFT) [75], no other theories have emerged which allow to predict total, elastic and diffractive cross-sections. A consistent non-perturbative QCD still needs to be formulated and numerical approaches, such as lattice QCD, are not yet capable to describe high-energy phenomenology from first principles.

## 6.4 Impact parameter representation

For the description elastic scattering [39, 60] of particle  $A$  with 4-momentum  $p_A$  off particle  $b$  with 4-momentum  $p_B$ ,  $A + B \rightarrow A + B$ , it is convenient to work with Mandelstam variables

$$s = (p_A + p_B)^2 \quad t = (p_A - p_{A'})^2 \quad u = (p_{A'} - p_{B'})^2, \quad (6.1)$$

where  $p_{A'}$  and  $p_{B'}$  denote outgoing momenta.

With  $\vec{k}$  being the momentum of the incoming particles in the center of mass system, the elastic scattering amplitude can be defined via its relationship to the differential elastic cross-section via

$$\frac{d\sigma_{el}}{dt}(s, t) = \frac{1}{64\pi s |\vec{k}|^2} |A(s, t)|^2 \approx \frac{1}{16\pi s^2} |A(s, t)|^2. \quad (6.2)$$

The optical theorem relates the total cross-section to the elastic scattering amplitude at  $t = 0$

$$\sigma_{\text{tot}} \approx \frac{1}{s} \Im m(A(s, t = 0)). \quad (6.3)$$

In general, the complex elastic scattering amplitude can be decomposed into a series of partial waves

$$A(s, t) = 16\pi \sum_0^\infty (2l + 1) a_l(s) P_l(\cos \theta). \quad (6.4)$$

The center-of-mass scattering angle  $\theta$  is given by

$$t = q^2 = -4k^2 \sin^2 \left( \frac{\theta}{2} \right), \quad (6.5)$$

where  $q$  denotes the transferred momentum. The impact parameter  $\vec{B}$  can be introduced and related to the angular momentum  $l$  in accordance to classical scattering as

$$k|\vec{B}| = kB = l + \frac{1}{2}. \quad (6.6)$$

The factor  $\frac{1}{2}$  is added for convenience [39]. At very high energies the number of contributing partial waves is high, so we can make the replacement  $\sum_l \rightarrow \int dl \rightarrow \int dB k$  in Eq. (6.4). Using a Bessel function to express the Legendre polynomials for large  $l$

$$P_l(\cos \theta) \xrightarrow{l \rightarrow \infty} J_0[(2l + 1) \sin^2 \left( \frac{\theta}{2} \right)], \quad (6.7)$$

and the analytic continuation of  $a_l(s)|_{l=kB} = a(s, \vec{B})$  for the impact parameter amplitude, Eq. (6.4) can be rewritten as

$$A(s, t) = 8\pi s \int_0^\infty dB Ba(s, \vec{B}) J_0(\sqrt{t}B). \quad (6.8)$$

To identify this equation as a Fourier transformation, we use the integral representation of  $J_0$

$$J_0(z) = \frac{1}{2\pi} \int_0^{2\pi} d\varphi \exp(iz \cos \varphi), \quad (6.9)$$

$\vec{q}\vec{B} = qB \cos \varphi$  and  $d^2\vec{B} = B dB d\varphi$  and obtain

$$A(s, t) = 4s \int_0^\infty d^2\vec{B} a(s, \vec{B}) e^{i\vec{q}\vec{B}}. \quad (6.10)$$

For  $\Re e A(s, t)^2 \rightarrow 0$

$$A(s, t) \approx |A(s, t)| = 4s\sqrt{\pi} \sqrt{\frac{d\sigma_{el}}{dt}(s, t)} \quad (6.11)$$

we can invert the Fourier-transform and get the prescription for the transformation of the differential elastic scattering cross-sections into the impact parameter amplitude

$$a(s, B) = \frac{1}{4\sqrt{\pi}} \int_0^\infty dt \sqrt{\frac{d\sigma_{el}}{dt}(s, t)} J_0(\sqrt{t}B). \quad (6.12)$$

## 6.5 Eikonal approximation and cross-sections in PHOJET

In GRFT the amplitude of a single (soft) pomeron exchange between particle  $A$  and  $B$  reads

$$A_{AB}^{\mathbb{P}_s} = is_0 g_{A\mathbb{P}}(t) g_{B\mathbb{P}}(t) \left(\frac{s}{s_0}\right)^{\alpha_{\mathbb{P}_s}(t)}, \quad (6.13)$$

where  $g_{i\mathbb{P}}$  denote the particle- $\mathbb{P}$  coupling and the  $t$ -dependent  $\alpha_{\mathbb{P}_s}(t)$  is the pomeron's Regge trajectory. The intercept at  $\alpha_{\mathbb{P}_s}(t=0)$  of the soft pomeron is supercritical ( $>1$ ). Neither the Regge trajectory nor the  $t$ -dependence of  $g_{i\mathbb{P}}$  are strongly fixed by theory and there are various possible choices, mostly motivated from comparisons with data [100, 85, 112]. In PHOJET the couplings have an exponential form in  $t$

$$g_{i\mathbb{P}}(t) = g_{i\mathbb{P}}^0(t) \exp\left(\frac{1}{2} b_{i\mathbb{P}}^0 t\right) \quad (6.14)$$

with the (soft) slopes  $b_{i\mathbb{P}}^0$ . The advantage of using this particular parametrization is that via the optical theorem and equations (6.11) and (6.12), one can compute the total soft cross section

$$\sigma_{AB}^{\mathbb{P}_s}(s) = g_{A\mathbb{P}}^0 g_{B\mathbb{P}}^0 \left(\frac{s}{s_0}\right)^{\alpha_{\mathbb{P}_s}(0)-1} = g_{A\mathbb{P}}^0 g_{B\mathbb{P}}^0 \left(\frac{s}{s_0}\right)^{\Delta_{\mathbb{P}_s}(0)}. \quad (6.15)$$

Since more components, such as additional reggeons or a hard pomeron contribution, behave additive on amplitude level, the Born graph cross-section can be approximated by

$$\sigma_{\text{Born}} = \sigma_{AB}^R + \sigma_{AB}^{\mathbb{P}_s} + \sigma_{AB}^{\text{hard}}. \quad (6.16)$$

Exponential forms of the  $t$ -dependence have the advantage that Fourier transformations between the  $t$ -space and the impact parameter space can be easily handled analytically.

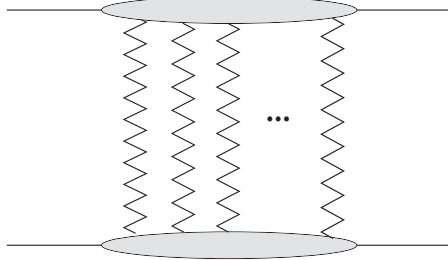


Figure 6.3: N-pomeron exchange graph. The blobs in the interaction region represent elastic and resonant intermediate states.

One possibility to derive the eikonal approximation is by summing over all  $n$ -pomeron  $\mathcal{IP}$  exchange amplitudes [60] (Figure 6.3). By assuming multiperipheral kinematics and that only elastic intermediate states are important, i.e. there is no ordering in time and space, or in other words all single exchange amplitudes refer to the same incoming and outgoing state, the  $n$ -pomeron amplitude can be approximated with the expression

$$A^{(n)} = -i(i)^n \frac{1}{n!} \left( \frac{1}{2s} \right)^{n-1} \prod_{i=1}^n \left( \int d^2 k_{\perp,i} A^{(1)}(s, k_{\perp,i}^2) \right) \frac{\delta^{(2)}(q_{\perp} - \sum_{i=1}^n k_{\perp,i})}{(2\pi)^{2(n-1)}}, \quad (6.17)$$

basically a product of one-pomeron exchange amplitudes and the alternating-sign factors from Abramovski-Gribov-Kancheli cutting rules, which take care of permutations and double counting of equivalent graphs.

The  $n$ -pomeron exchange amplitude can be obtained by transforming from  $t$  into impact parameter space amplitude

$$\begin{aligned} a^{(n)}(s, \vec{B}) &= \frac{1}{4s} \int \frac{d^2 q_{\perp}}{(2\pi)^2} A^{(n)}(s, q_{\perp}^2) e^{-i\vec{q}_{\perp}\vec{B}} \\ &= -\frac{i}{2}(i)^n \frac{1}{n!} \prod_{i=1}^n (2a^{(1)}(s, \vec{B})), \end{aligned} \quad (6.18)$$

where  $a^{(1)} = a^{\text{Born}}(s, \vec{B})$  denotes the impact parameter amplitude of the one-pomeron exchange. The summation of all  $n$ -pomeron amplitudes yields the eikonal approximation

$$a(s, \vec{B}) = \sum_{n=1}^{\infty} a^{(n)}(s, \vec{B}) = \frac{i}{2} \left( 1 - \exp \left[ -\chi(s, \vec{B}) \right] \right). \quad (6.19)$$

Some properties of the eikonal function  $\chi(s, \vec{B})$  are

$$\chi(s, \vec{B}) = -2ia^{(1)}(s, \vec{B}) \quad \text{and} \quad 2 \int d^2 \vec{B} \chi(s, \vec{B}) = \sigma^{\text{Born}}(s). \quad (6.20)$$

One consequence of writing  $a(s, \vec{B})$  using the eikonal function is that its upper bound becomes 0.5 in case of purely real  $\chi$ . The imaginary part of  $\chi$  can not be independently chosen, since the functions underly analyticity constraints [100]. The real part of the amplitude at small  $t$  can be either obtained from dispersion relations [39, 100] or by substitution of  $s^\alpha \rightarrow (s e^{-i\frac{\pi}{2}})^\alpha$ , for example in Eq. (6.15) where  $\Delta_{P_s} \sim 0.1$ .

Another consequence of eikonalized amplitudes is the conservation of unitarity [39, 60].

Using the definitions above one can derive the following expressions

$$\sigma_{\text{tot}} = 2 \int d^2 \vec{B} \Im m(a(s, \vec{B})) = 2 \int d^2 \vec{B} (1 + e^{-\chi_R} \sin \chi_I) \quad (6.21a)$$

$$\sigma_{\text{el}} = 2 \int d^2 \vec{B} |a(s, \vec{B})|^2 = \int d^2 \vec{B} (1 + 2e^{-\chi_R} \sin \chi_I + e^{-2\chi_R}) \quad (6.21b)$$

$$\sigma_{\text{inel}} = \sigma_{\text{tot}} - \sigma_{\text{el}} = \int d^2 \vec{B} (1 - e^{-2\chi_R}) \quad (6.21c)$$

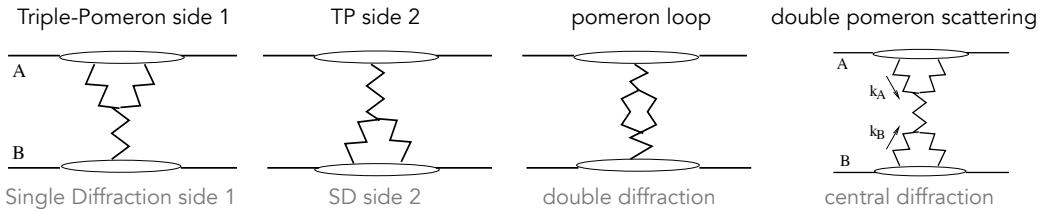


Figure 6.4: Enhanced graphs in PHOJET.

The unitarization scheme in PHOJET is based on the eikonalization on Born-level graph amplitudes of simple and enhanced graphs (see Figure 6.4)

$$\chi(s, \vec{B}) = \chi_S(s, \vec{B}) + \chi_H(s, \vec{B}) + \chi_{\text{TP}}(s, \vec{B}) + \chi_{\text{LP}}(s, \vec{B}) + \chi_{\text{DP}}(s, \vec{B}). \quad (6.22)$$

The subscripts refer to different types of (enhanced) graphs: S single-pomeron exchange, H "hard" (pQCD) pomeron exchange, TP the triple pomeron graph for high mass-diffraction, LP loop pomeron graph for central diffraction and DP the explicit double-pomeron exchange. Low-mass diffraction, the excitation of an initial hadronic state  $l$  into an excited state  $l^*$ , is implemented via a two-channel formalism, where the eikonal functions are represented as  $2 \times 2$  matrices. The possibility for the interaction of excited states is symbolized by blobs in Figure 6.4. The unitarization scheme is the basis for arbitrary complex event topologies. Each collision is allowed to have combinations of multiple exchanges of any of the above listed graphs.

Under the assumption of uncorrelated multiple exchanges of pomeron graphs which result in particle production, called (inelastic) cuts, the probability distribution is poissonian. This picture yields the cross-section for multiple cuts, or graph exchanges, by expanding Eq. 6.21c

$$\sigma(n_S, n_H, \dots) = \int d^2 \vec{B} \frac{(-2\chi_S)^{n_S}}{n_S!} \frac{(-2\chi_H)^{n_H}}{n_H!} \dots \quad (6.23)$$

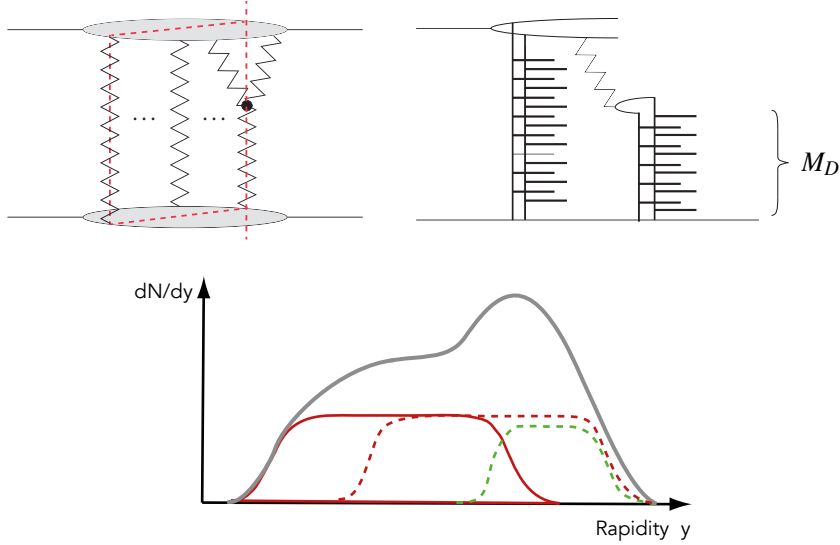


Figure 6.5: Particle production in an event with one cut pomeron and one cut triple-pomeron graph. The cut triple-pomeron graph results in a high mass diffraction with mass  $M_D$ .

One example for an event topology, consisting of multiple cut graphs, is given in Figure 6.5. The uncut graph in the middle of the upper right diagram is purely elastic and does not contribute to particle production.

## 6.6 Reconstructing the impact parameter amplitude from elastic scattering

The optical theorem (Eq. 6.3) relates the total cross-section to elastic scattering. By recovering the elastic scattering amplitude from measured differential cross-sections, it should be therefore possible to learn about the form of the amplitude and possible signatures of (scattering probability) saturation.

### 6.6.1 Interference structure of the complex scattering amplitude

To understand the dip structure of the elastic differential cross-section, the correspondence in Eq. (6.12) can be used. In a first step the experimentally measured  $\frac{d\sigma_{el}}{dt}$  is fitted in the momentum-transfer-space using the function

$$\frac{d\sigma_{el}}{dt} = \left| i\alpha(A_1 e^{-\frac{b_1}{2}\alpha|t|} + A_2 e^{-\frac{b_2}{2}\alpha|t|}) + iA_3 e^{-\frac{b_3}{2}\alpha|t|} \right|^2 \sim |A(s, t)|^2, \quad (6.24)$$

where the  $A_i$ 's are real normalization constants, the  $b_i$ 's are real valued slopes and  $\alpha$  is a complex constant. In the past, this function has been successfully applied in the analysis of ISR data [24]. Other parameterizations, for example from [104], were tested but Eq. (6.24) is found to be deliver superior performance and reliability.

The fitting procedure is performed for three proton-proton and proton-antiproton datasets, each chosen according to the following quality requirements:

- The data extends from very small  $t$  values near the coulomb-interference region/ optical point up to as large as possible  $t$  values.
- If a dataset is composed from different experimental publications and/or different collider runs, they have to be properly normalized and matched to each other (see e.g. procedure by Schubert [24]),
- The dip or shoulder region needs to be well measured, since it is the most crucial  $t$ -range for the determination the ratio between the real and imaginary parts of the fit function,
- A measurement of  $\rho(s) = \Re A(s, t = 0)/\Im m A(s, t = 0)$  is helpful to disentangle the ambiguity between real and imaginary part.

Investigated is data from three generations of colliders, ranging from the ISR (70's-80's) at 52.8 GeV [24], the SPS (80's-90's) at 540 GeV [35, 43] to the LHC at 7 TeV [137, 136]. At the SPS and the LHC the small and large  $t$  measurements have been merged without further normalizations, since they match smoothly.

The implementation of the Levenburg-Marquardt algorithm (least-squares) in the MINPACK package has been used to minimize the parameters. The covariance matrix contains several coefficients close to one, which should come at no surprise, since a complex function is only restricted by its modulus and the role of the three exponentials is to some extent interchangeable in the sense that any of them can be leading in a certain range of  $t$ .

## Fit results

The parameters are not restricted with the aim to fix the roles of the exponentials in certain  $t$  ranges, i.e. the third exponential representing small  $t$  and the others interference (dip) region and large  $t$ . The fit results are listed in Table

Table 6.1: Fit parameters for Eq. 6.24.

Dataset	$A_1$	$A_2$	$A_3$	$b_1$	$b_2$	$b_3$	$\Re e \alpha$	$\Im m \alpha$
ISR 52.8 GeV	5.11	12.61	0.02	43.37	17.97	1.06	0.54	-0.05
SPS 540 GeV	6.46	13.93	0.15	35.42	17.17	2.43	0.70	-0.13
LHC 7 TeV	7.86	38.38	1.15	22.16	41.15	4.63	0.51	-0.08

### 6.1.

The left panel of Figure 6.6 shows the excellent result of the fit. The functional form is compatible with the dip structure for both  $pp$  and  $p\bar{p}$  scattering. The breakdown plot in the right panel and the ration of real to imaginary part, demonstrate how the complex phase emerges from the superposition of

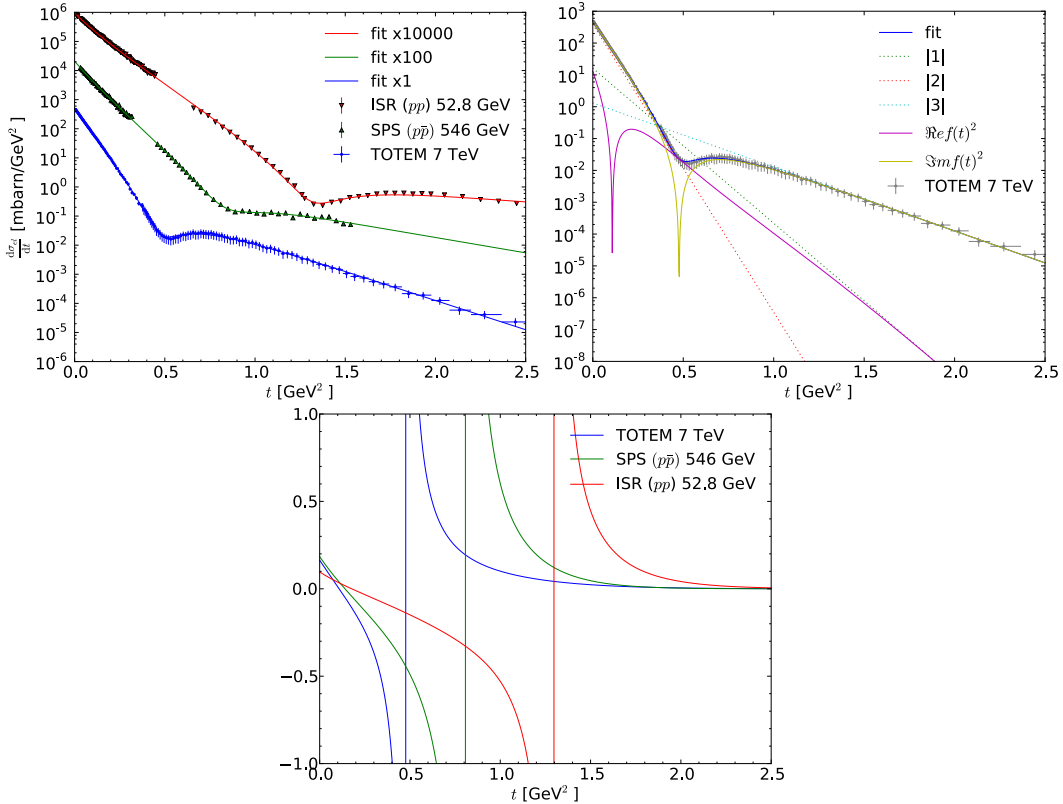


Figure 6.6: (left panel) Results of the fit using the parameters given in the text. The datasets and the fit multiplied by offset for clarity. (right panel) Ratio of real-to-imaginary part of  $A(s, t)$ .

the three functions. One one hand, the approximation of a purely imaginary amplitude in PHOJET and other generators seems adequate, since  $\rho(s)$  is indeed small, 0.1 at ISR and somewhat higher at Tevatron and LHC not exceeding 0.2. On the other hand, due to the Fourier correspondence between  $t$ -space and  $\vec{B}$ -space, large values of  $t$  notably contribute to  $a(s, \vec{B})$  for small values of  $\vec{B}$  and can become important when judging how close the amplitude approaches the black disk limit. Except for different values and positions of the breakdown, the fit it is very similar for the other energies.

### 6.6.2 Interpolation of the elastic amplitude

In section 6.6.1 some model dependence is involved into the derivation of the amplitude. Mainly it is the idea that the dip structure is a consequence of the complex interference of several exponential functions. In fact, we don't know how  $\Re A(s, t)/\Im A(s, t)$  evolves for other values of  $t$  except  $t = 0$ . The excellent quality of small- $t$  and large- $t$  data from the TOTEM experiment is suitable for an interpolation under the assumption that  $\rho$  is constantly zero over the entire range of  $t$ , i.e. the reconstructed amplitude is purely imaginary as it is in the models.

The TOTEM Experiment took several times data in  $pp$  collisions at 7 TeV at

the LHC. Two elastic scattering datasets, measured with different beam optics, span the ranges  $0.02 < -t < 0.33 \text{ GeV}^2$  (EPL96) [136] and  $0.36 < -t < 2.5 \text{ GeV}^2$  (EPL95) [137] of the momentum transfer squared. It is straight forward to stack both sets together since their normalizations match and appear consistent over the entire  $t$  range.

For a robust and smooth interpolation, the range of  $t$  is subdivided into three regions

- I) small- $t$   $0 < t \leq 0.25$ : fit using  $a_I e^{-B_I t + C t^2}$
- II) dip region  $0.25 \leq t < 1.0$ : fit and interpolation with cubic-splines
- III) large- $t$   $1.0 \leq t < 5.0$ : fit using  $a_{III} e^{-B_{III} t}$

By using a similar technique as in section 6.6.1, the fit parameters are found to be are  $a_I = 503.139 \pm 19.575 \text{ mbarn/GeV}^2$ ,  $B_I = 19.575 \pm 0.011 \text{ GeV}^{-2}$ ,  $C = -2.133 \pm 0.231 \text{ GeV}^{-4}$ ,  $a_{III} = 1.039 \pm 0.005 \text{ mbarn/GeV}^2$  and  $B_{III} = 4.519 \pm 0.003 \text{ GeV}^{-2}$ . In order to estimate the effect due to the dip and the harder

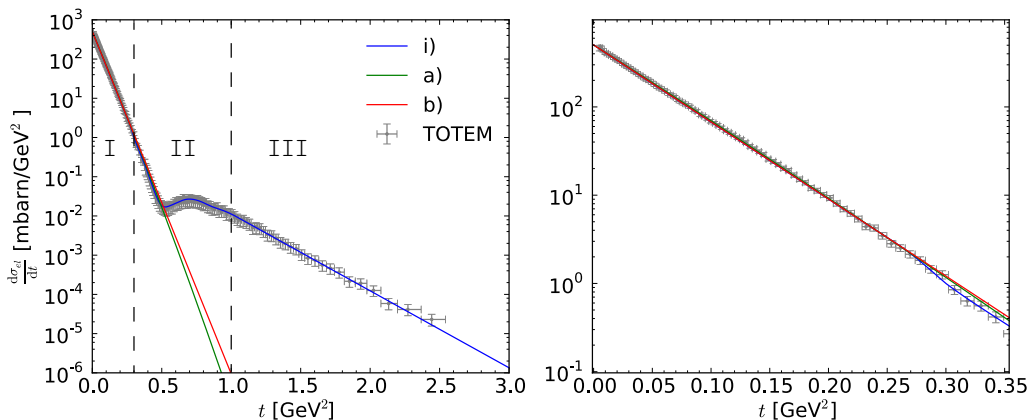


Figure 6.7: Fits and interpolations compared to the combined EPL95 and EPL96 TOTEM data. *i*) is the result of interpolation, *a*) the exponential fit with a curvature parameter and *b*) a simple gaussian fit using the  $B_0(t = 0)$  value from EPL96. The right pane enlarges the small  $t$  region.

large  $t$  behavior of  $d\sigma_{el}/dt$  on the impact parameter amplitude, alternative, simpler forms are also used:

- a) same as region I)
- b)  $\frac{d\sigma_{exp}}{dt}|_{t=0} e^{-B_{exp}t}$  with fit parameters obtained by TOTEM as listed EPL96
- c) gaussian impact parameter amplitude  $a(s, B) = \frac{\sigma_{tot,exp}}{8\pi B_{exp}} e^{b^2/(2B_{exp})}$  using  $\sigma_{tot,exp}$  from EPL96

The fit regions as well as the result of the interpolation is shown in Fig. 6.7. The right panel demonstrates that at  $t = 0$  the different parameterizations are indistinguishable, leading to the same value of  $\sigma_{tot}$ .

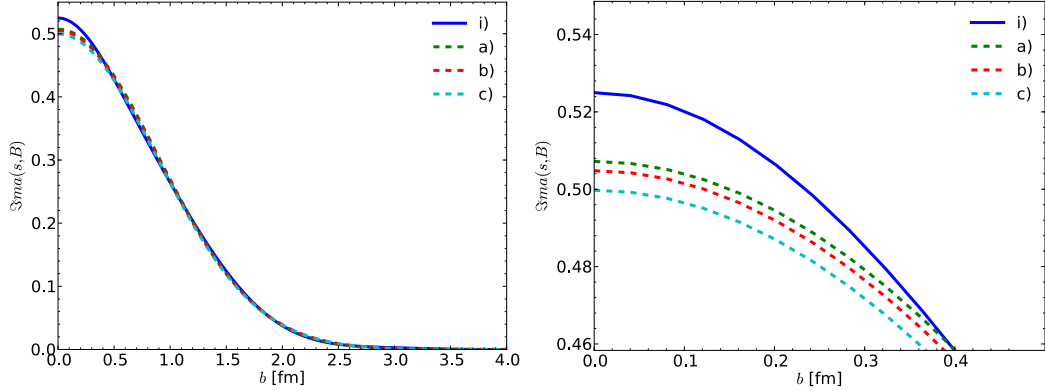


Figure 6.8: Impact parameter amplitudes, obtained by transformation from  $t$ -space using Eq. 6.12. The right panel zooms into the important region around the black disc value  $\Im m a(s, \vec{B}) = 0$ .

The numerical transformation from  $t$ -dependent into impact parameter amplitudes with Eq. 6.12 requires accurate numerical work. Several cross-checks and parameter studies were performed to gain confidence in the numerical result.

## 6.7 Results and discussion

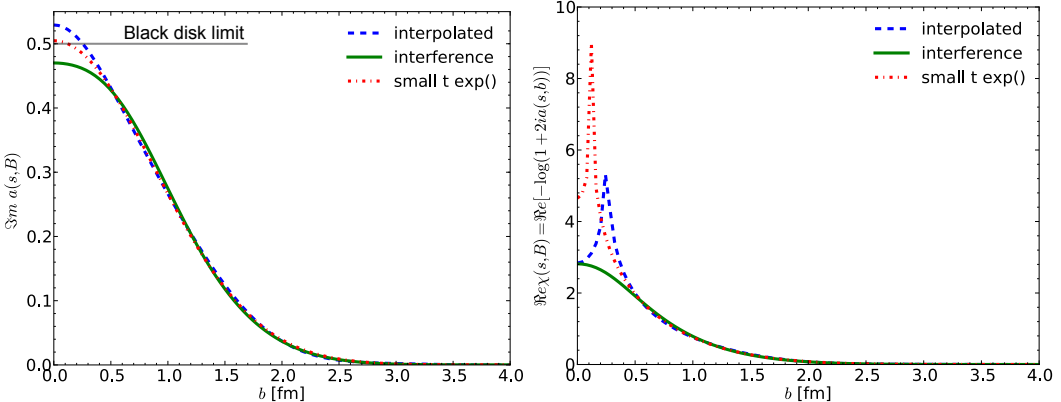


Figure 6.9: (left panel) Imaginary part of impact parameter amplitude at 7 TeV. (right panel) Eikonal function naïvely calculated by inverting 6.19.

Figure 6.9 shows the imaginary part of the impact parameter amplitude, reconstructed using different functional forms. The *interference* line is the transformation of the complex amplitude fit from section 6.6.1 into impact parameter space using Eq. (6.8). The *interpolated* line is obtained using techniques from section 6.6.2 where the *small t exp()* line corresponds to case a). Both assume a purely imaginary amplitude and are transformed using Eq. 6.12.

The result is that in the case where the real part of the amplitude is neglected, the black disk limit would have been exceeded, violating unitarity and

also analyticity. In the case where the complex amplitude is explicitly recovered from data, the black disk limit is not exceeded and there is still a sizable margin to get there. Also, the amplitude shows some widening. The attempt to naively calculate an eikonal function by inverting Eq. (6.19) is shown in the right panel of Figure 6.9. The *interference* model, the only one not exceeding the black disk limit, gives some guidance how a possible eikonal function can look like. Event generators typically use gaussian or electrical dipole form factors. In the other two attempts, the eikonal changes its complex phase at small values of the impact parameter, producing discontinuities.

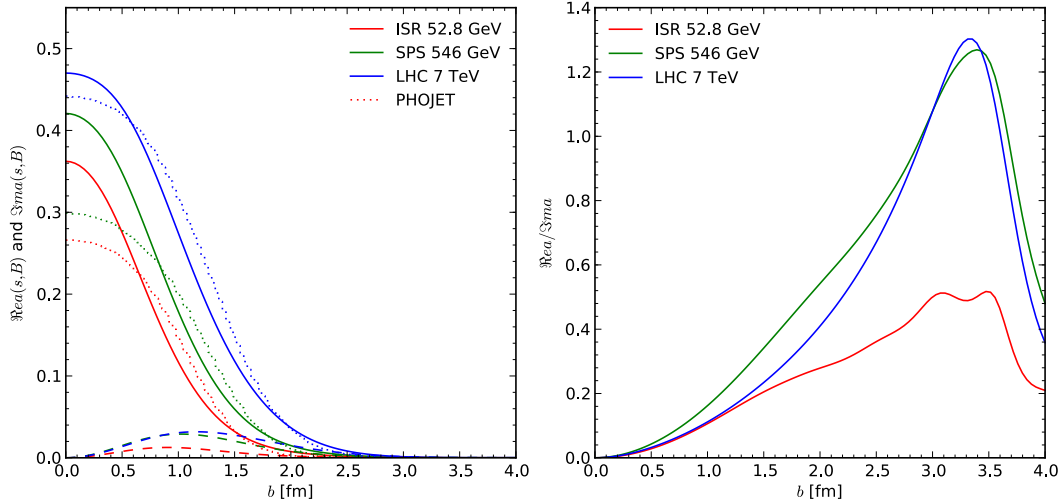


Figure 6.10: (left panel) Energy dependence of  $a(s, \vec{B})$  obtained from *interference* type fits and eikonalized amplitudes from PHOJET. (right panel) Ratio of real and imaginary part of  $a(s, \vec{B})$ .

What if we mitigate the question and instead of asking for exceeding the black disk limit, what is certainly not the case at the LHC, formulate the question in the following way: Does the proximity of the black disk limit introduce qualitative changes in the form of the impact parameter amplitude?

Looking on Figure 6.10 the answer is definitely not no. While the amplitude at low ISR energies has a nearly gaussian shape, it flattens for small  $b$  at high energies. The amplitudes in PHOJET are flatter and wider what is not necessarily a problem, since only the integral  $\sim \int db b a(s, b)$  is constraint by cross-section data, not its shape. In addition the amplitude is a superposition of various higher order graphs and contains diffractive and inelastic topologies. This large difference between the shapes could raise other questions in future studies.

## 6.8 Returning to multiplicity distributions at the LHC

The framework from section 6.5 allows us to construct a toy-model for the study of the dependence of multiple cuts as a function of energy, which directly

relate to the number of multiple parton interactions in a more complete model.

The simplest model, which replicates the multiplicity behavior, includes a two-component pomeron, with a soft and hard component. Diffractive topologies can be neglected, since they only contribute to a small fraction of the cross-section at high energies. For a more accurate description at lower energies an effective reggeon (intercept  $\alpha_{IR} < 1$ ) is also included.

Using Equations (6.15), (6.16), (6.19) and (6.20), we can write down the following model for the scattering of two equal particles

$$\chi_{IP}(s, b) = \frac{g_{IP}^2 s_0}{16\pi B_{IP,eff}(s)} \left( \frac{s}{s_0} \right)^{\Delta_{IP}} \exp \left( \frac{-b^2}{4B_{IP,eff}(s)} \right). \quad (6.25)$$

The soft  $IP_S$  and hard  $IP_H$  component only differ by the choice of parameters. The effective slope is traditionally parameterized as

$$B_{IP,eff}(s) = B_{IP,0} + \alpha'_{IP} \ln \frac{s}{s_0}, \quad (6.26)$$

where the slope of the pomeron-trajectory  $\alpha'_{IP}$  describes the transverse growth of the hadron. Since the equations (6.21) enable direct calculations of cross-sections, several parameters can be obtained from a fit to data. The hard

Table 6.2: Model parameters.

component	$\Delta_{IP}$	$\alpha'_{IP}$	$g_{IP}$	$B_0$
soft	0.111	0.27	6.143	3.2 GeV <sup>2</sup>
hard	0.2	0.0	1.6	2.0 GeV <sup>2</sup>
reggeon	-0.455	0.9	17.33	0.7 GeV <sup>2</sup>

cross-section intercept is adjusted and fixed to be similar to the minijet cross-section. The parameter  $s_0 = 1.0$  GeV<sup>2</sup> is fixed.

The results are shown in Figure 6.11. The *full* label stands for the full eikonal model (soft + hard + reggeon), while curves labeled *soft* only show the contribution of the soft component. The result of the fit to the total cross-section in the upper left panel proves a reasonable description of data. The energy evolution of the impact parameter amplitude is demonstrated in the upper right panel, where the 100 TeV line reaches the black disk limit and flattens for small  $b$ . The bottom left panel shows that this effect starts above a few TeV and becomes very strong above tens of TeV. This particular model closely approaches the black disk limit at 30 TeV.

The distribution of the cross-section for multiple cuts calculated with Eq. (6.23) is located in lower right panel. When energy increases, the probability distribution for multiple hard interactions becomes flatter at higher  $n_H$ . This effect is responsible for the multiplicity distributions in PHOJET at 7 TeV and most probably in some of the other event generators in Figure 6.1 as well, which use eikonalization as the basis for the modeling of multiple parton interactions and for the conservation of unitarity.

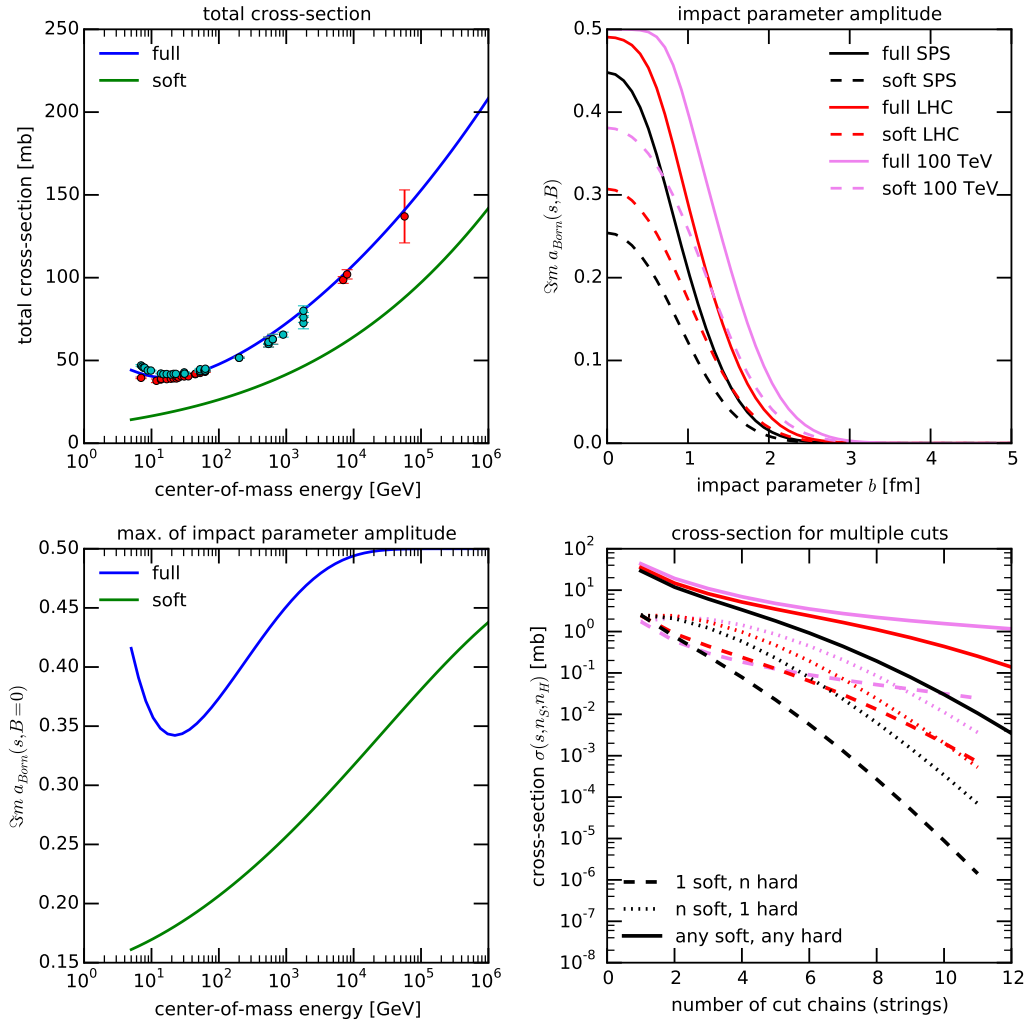


Figure 6.11: Results obtained with the simple eikonal model using the parameters from Table 6.2. The colors in the lower right panel represent energies as in the upper right one.

PYTHIA [124] has an alternative method to restore unitarity by using "Sudakov" form factors, see Eq. (2.26) in [49]. With this method, the shape of the impact parameter amplitude is not deformed by unitarity corrections as in Eq. (6.19). It adds an additional level of control with respect to the shape of the multiplicity distribution by free choice of the transverse overlap function. Some cosmic ray generators employ various phenomenological, often non-perturbative, ideas to control the behavior at very high energies. EPOS [114] handles high parton densities with a hydronodynamical concept. Even in proton-proton collisions, the energy density between two colliding particles can produce a Quark-Gluon-Plasma, which stochastically expands and fragments into hadrons. Additionally it includes energy sharing, a strong force exchange between interleaved scattering partners. In QGSJET-II [108] absorptive corrections are recursively inserted into each pomeron graph, using self-interaction of pomerons employing vertices of higher order than three.

Strongly influenced by Gribov's Reggeon field theory the authors had to take several phenomenological decisions to make it work.

The disagreement in multiplicity distributions is certainly a fundamental drawback of the eikonal model as it is formulated now. The assumption of multiperipheral kinematics and that in the construction of the n-pomeron amplitude only elastic graphs contribute seem too strong. Expecting that all partons in a hadron could be potential scattering partners seems to be not realistic enough for modeling interactions at energies of the LHC. On the other hand, the unitarization scheme via eikonization performed very well in the past and it even produced robust predictions for the LHC, often better than models based on other schemes [52]. A new central question has also to include the purpose of the model, since there are a number of models for a specific application one can choose from. For cosmic ray applications, the ability to extrapolate robustly far beyond collider energies is one of the most crucial aspects. PYTHIA and other high-energy physics generators didn't show good results when the energy was increased by a factor of three between the Tevatron and the LHC. However after some time and retuning effort, the models, in particular PYTHIA, were able to match better. Nowadays every experiment at the LHC produces a personalized tune of a general purpose generator, which describes their low level distributions in the best way, technically. Asking a more provocative question, what the physical difference between  $pp$  interactions at LHCb and CMS is, can be passed to the interested reader.

If the eikonal model does not need global overhaul, what can be done instead to repair the behavior?

It could be sufficient to expand the view of the collision into (geometrical) longitudinal space, taking some ideas from dipole models as it is implemented in the Monte Carlo generator DIPSY [77]. In this picture the effect of partonic "screening" naturally emerges by considering the (longitudinal) transport of a color dipole through dense partonic matter. Sketched in Figure 6.12 is the collision of two Lorentz-contracted hadrons, viewed from the  $(y, z)$ -plane. One driving idea could be to modify the expressions of elementary parton-parton interactions and accommodate the possibility that not all partons are located on a plane surface but instead on a disk with some extension in  $z$ . The number of partons seen from each hadron's side would be effectively reduced the denser the matter becomes. The elaboration of these ideas and possible ways to merge them with the current framework has to be part of a future study.

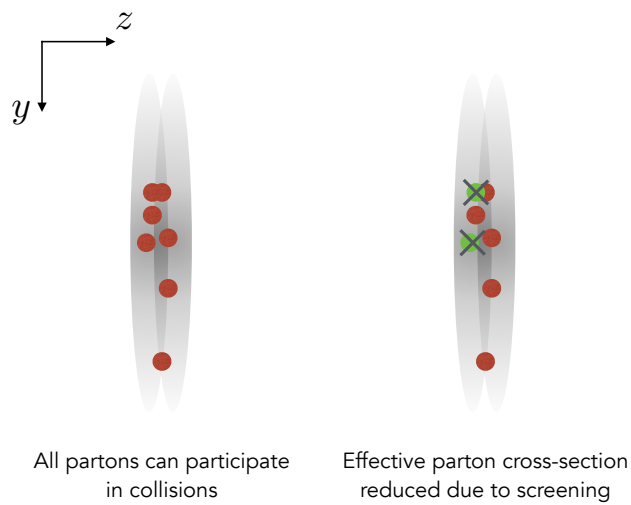


Figure 6.12: (Longitudinal) screening of partons. The red dots symbolize individual parton-parton interactions. Those in green are screened by a preceding interaction in time and space.



# Chapter 7

## A new revision of PHOJET and DPMJET

PHOJET is a minimum-bias Monte Carlo event generator [60, 59, 61] for hadron-hadron, photon-hadron and photon-photon interactions. The basis of the model is the two-component Dual Parton Model [46], which integrates the ideas of Regge theory [75, 76], non-perturbative and perturbative expansions of QCD within a common framework. Generally accepted arguments, such as unitarity or duality [48, 33], support the self-consistency of the model and should allow to make relatively robust extrapolations up to very high future collider or cosmic ray energies. Historically the model DTUJET-93 [30] contained an almost complete description of soft processes and a model for gluon-gluon scattering as the hard component. PHOJET superseded it in the second part of the 1990’s with a complete (source code) rewrite, a new model for photon-hadron and photon-photon interactions and a full set of leading-order QCD processes, an interface to parton distribution function libraries and many more features. For fragmentation, as the last step in the generation of an event, PHOJET interfaces with PYTHIA, or JETSET in the older versions.

DPMJET-III [119] is a generator for hadron-nucleus, photon-nucleus and nucleus-nucleus collisions. It uses PHOJET to generate individual hadron-hadron and photon-hadron collisions. I.e. calling DPMJET for a proton-proton collision is identical to calling PHOJET for the same setup. DPMJET provides a realization of the Glauber model for nuclear collisions, photo-nuclear interactions, intranuclear cascade models, spectator fission and fragmentation, and it includes models for low energy interactions. DPMJET-III is released as a public version and also as part of the FLUKA particle physics simulation package [63, 41].

This project makes use of the influx of fresh LHC data to revise the models for recent and future collider development and on the other hand to integrate them deeper into the astroparticle physics community.

## 7.1 Technical state of the programs at the beginning of the project

The last author modifications to PHOJET are dated to 2001. At this time the generator described in high detail proton-antiproton collisions up to the energy of 1.96 TeV of the Tevatron and also multi-particle production at HERA.

### 7.1.1 PHOJET

Several versions of the source code are circulating:

- a public stand-alone version 1.12-35,
- a development version, including a few more recent modifications, C pre-processor directives for conditional compilation and common block includes,
- the FLUKA version, based on 1.12-35, separated into individual files for each subroutine, containing FORTRAN style includes of common blocks.

PHOJET 1.12-35 comes bundled together with the complete source code of the PYTHIA 6.1 package [124]. PYTHIA's routines are used for running the Lund-fragmentation scheme on partonic states, final state radiation and for the decays of short-lived particles.

The format is standard fixed-format FORTRAN 77 with only very few features taken over from F90 extensions to the standard. The only extensions used are

- mixed use of old-style `DO-CONTINUE` and new-style `DO-ENDDO` loop definitions,
- some variable names are longer than 6 characters and contain underscores,
- at one location dynamic array memory allocation is used in a bundled PDF library.

The style of the code has some visible tension in the coding style and formatting between old parts of the code, including routines ported from its predecessors, and the more recently written parts, making the code somewhat inhomogeneous. Some functionality was added later on top, for example the routines for resolved pomeron interactions in the Ingelman-Schlein picture [84] require a recursive "interaction-within-an-interaction-approach". Since FORTRAN 77 does not support recursive subroutine calls, the author added management structures to dump and restore the state before and after the "recursive" iterations. This modification increased the complexity of the program flow and introduced problems for debugging.

The state of documentation is not exceptional. The global ideas and formulas are contained in the main author's PhD thesis [60]. Another document `phoman112.pdf` is an excerpt of the thesis plus additional user documentation, explaining some of the common block variables, parameters and particle/status codes. Since on top of that a developer documentation or a complete reference manual do not exist, the most valuable sources of information are personal discussions with the main author and the explanations in the headers of subroutines.

Differences between the source code versions listed above are purely technical. Although there is no possibility to compare the versions using tools like `diff`, the comparison of the results and of detailed debug output yielded no divergence between them.

Apart from these rather minor deficiencies, the program contains many helpful features, detailed debugging output and cross-check routines for all kinds of special purposes. An integer array with up to 100 elements controls the verbosity of the output in a very fine-grained way. In general, the code is in a manageable and debugged state as long as the execution follows proven code paths.

### 7.1.2 DPMJET

The source of DPMJET III circulates in several flavors

- latest public release as version 3.0-6 in a single file,
- older minor releases, which have been integrated into experimental frameworks or cascade programs
- the version bundled with FLUKA

All versions are written in FORTRAN 77 and, although identical in high-energy behavior, they differ in several aspects as summarized in Table 7.1.

A severe problem is that there is no possibility to detect differences between the versions apart from comparing physical distributions on a "macroscopic" scale. Due to many modifications between the FLUKA version and the latest release `diff` can not be applied in a meaningful way. The comparison of random number sequences is mostly effective in detecting a divergence in behavior between technical changes which should not affect the physics.

In contrast to PHOJET the differences between the DPMJET versions are not just technical. As listed in Table 7.1 the standalone version lacks several models which have been either merged with the core functionality of FLUKA or introduced later in the second part of the 2000's. For these reasons the two versions have to be maintained separately and, in fact, treated as two different programs. In case of the standalone version, there is neither a source version control nor any kind of change-log available.

The style of the source is very inhomogeneous. Some code parts are visibly taken over from very old versions of the predecessors DTUNUC and BAMJET

Table 7.1: Differences between the standalone and the FLUKA version of DPMJET III version 3.0-6.

DPMJET standalone	DPMJET in FLUKA
<ul style="list-style-type: none"> <li>• source code in one file</li> <li>• no preprocessor directives</li> <li>• public single-file PHOJET version</li> <li>• nuclear cross-sections calculated at initialization</li> <li>• distribution via e-mail to authors</li> <li>• no fission/evaporation module</li> <li>• no chain fusion/color reconnection</li> <li>• no verbosity control</li> </ul>	<ul style="list-style-type: none"> <li>• each subroutine in own file</li> <li>• <code>include</code> directives for common blocks</li> <li>• bundled version with modified source</li> <li>• nuclear cross-sections pre-tabulated</li> <li>• distribution as part of FLUKA</li> <li>• evaporation when linking with FLUKA</li> <li>• chain fusion/color reconnection for nuclei with <math>A \geq 12</math></li> <li>• verbosity control via LPRI variable</li> <li>• bug-fixes and additional checks</li> <li>• less compiler warnings</li> </ul>

[120], including FORTRAN 66 features such as Hollerith characters. Other parts of the program contain routines ported from PHOJET but instead of extending PHOJET and linking it as a library the code has been copied and branched off from the PHOJET development. The general coding style and variable naming suggest that several developers worked on the code. Although several code paths became obsolete, the work to refactor and clean-up the traces has never been accomplished, making the code bloated with its 40k lines (excluding the bundled PHOJET and PYTHIA programs).

Although modifications to DPMJET were not the main goal of this project, the deep interrelation with PHOJET required updating both versions of DPMJET as soon as PHOJET underwent significant technical changes. The lack of detailed or "non-author" debugging information resulted in long development and bug-fixing cycles.

The state of documentation is inadequate. The models for photon-nucleus interactions are described in [120] and the references therein. The user-interface is meant to be driven by ASCII control cards containing a sequence of keywords and parameters. Apart from short descriptions of the keywords, a few in-line comments and the rare occurrence of descriptions in subroutine headers, no documentation is available.

There was some granularity control of the output verbosity foreseen, but never properly implemented. Sometimes physical cross-check routines can catch inconsistencies, but their level of output is insufficient to understand the error without understanding the full mechanism of the cross-check first

and then the exact state of the program flow before the occurrence of the error. At least, the long life-cycles of the versions and broad usage by the community helped to reach a state, where the program runs stable in typical usage scenarios.

## 7.2 Goals for the new version

At the time of writing the LHC just restarted with Run-II at 13 TeV center-of-mass energy. For the previous run at 0.9, 2.36, 7 and 8 TeV the majority of minimum-bias results is already published. A natural goal is to compare the physics performance between PHOJET and data and, in a first step, locate the distributions which are insufficiently described. In a later step the model can be updated, tuned or changed to achieve a better agreement with the experiment.

Astroparticle physics is currently a popular field with strong requirements on the quality of hadronic interaction models, in particular regarding the extrapolation into unexplored energy regimes and the prediction of very forward distributions. For studies on LHC upgrades or on future hadron colliders, such as Future Circular Collider (FCC) project at CERN, the requirements are similar. In hadron collisions at 100 TeV center-of-mass (as it is foreseen in FCC), secondary particles travel at energies not far from cosmic rays and deposit energy in machine elements.

Several publicly available event generators are specialized on these applications, in particular on extensive air shower simulations and particle cascades in matter at very high energy. Recently the high-energy physics community discovered that these models perform very well as general purpose Monte Carlos in collider applications [52] and they tend to have a good predictive power (see for example the first 13 TeV results [29, 92, 28]). The community calls these models cosmic ray Monte Carlos or generators. Typical requirements include:

- the simulation of collisions up to ultra high energies  $\leq 10^{21}$  eV,
- strict energy and momentum conservation,
- model for meson-nucleon and hadron-nucleus interactions
- multiple projectile target combinations in one run initializing just once in the beginning, e.g. in a cascade program
- detailed microscopic model for forward and diffractive physics,
- nuclear interaction model supporting at least projectiles with  $A_p \leq A_{\text{Fe}}$  and targets with  $A_T \leq A_{\text{air}}$ ,
- consistent and smooth behavior of total and partial process cross-sections over the entire energy range.

DPMJET together with PHOJET fulfill several of these requirements, but other features are missing. The first shortcoming is PHOJET’s model for the total and partial process cross sections. It tops out at several tens of TeV in center-of-mass frame, because some of the diffractive cross-sections become negative. The second shortcoming is the lack of the possibility to handle multiple projectile-target combinations simultaneously. Although the models always supported meson-hadron or meson-nucleus interactions, they only kept one set of tables in memory. The application for particle cascades requires that the model accepts different projectile-target combinations in the same run (see section 7.3).

By implementing the necessary modifications and by bringing DPMJET, which is at this moment mostly used across the particle physics community, into astroparticle physics will result in mutual benefits. On the astroparticle side, a new model with a detailed underlying microscopical picture will allow for novel types of studies in air-shower physics. Further, the model can be employed for much more sophisticated calculations of astrophysical cascades at the location of the sources of ultra high energy cosmic rays, since it works down to threshold energies and can also handle interactions with nuclei and real or virtual photons. The benefit for the collider community is that the model will be tested and improved in a much wider range of the phase-space. Since it is capable to handle center-of-mass energies across six orders of magnitude it can be used in detailed cascade codes with many generations of secondary interactions. Radiation protection or energy deposition calculations will profit from a consistent treatment of all particle interactions on the same footing and at the same level of detail.

Another aspect is the technical improvement and quality assurance, i.e. finding and correcting bugs, refactoring of the source code, ensuring compatibility with modern compilers and higher optimization levels.

## 7.3 Multi-particle modification

PHOJET supports effectively only one projectile-target combination per initialization. Multiple calls to the initialization routines are not supported and not recommended. The initialization sequence in PHOJET is

1. general parameter initialization in `PHO_INIT(...)` (static parameters),
2. initial calculation of cross-section, process probabilities for a single projectile-target combination in a call to `PHO_EVENT(-1,...)`,
3. per-event initialization, like resetting counters and stacks, updating statistics metrics during subsequent calls to `PHO_EVENT(>0,...)`.

The most time consuming part, taking seconds on modern computers, is the calculation of the hard cross-section as a convolution of leading-order QCD matrix elements with parton densities over the entire phase-space. Therefore

it is crucial to avoid repetitions of this step when switching between different projectiles.

The question how to implement the desired functionality is accompanied by several constraints. Due to the close relationship with DPMJET and FLUKA the data structures for storing cross-section tables and counters can not change significantly. Otherwise, motivated by the complexity of the event generation program flow, one would have to face significant effort when ensuring correct functionality after the modifications are in place. The other constraint is to keep initialization time reasonably short, since in most applications the generator will be used for single projectile-target combinations.

An on-demand scheme for the initialization appeared as the most reasonable, i.e. inserting additional initialization steps if a different projectile is requested. The minimal modification to the data structures is the extension by one dimension which index points to an unique projectile-target combination. The advantage of a dimensional extension is that the compiler will detect all indexing mismatches and reliably locate the places which need modification.

A set of routines is responsible for the switching between particle combinations. A new common block `POBEAM` contains tables and variables which keep track of the currently active particle combination, the maximum initialization energy and the status of mapping. Some projectiles for which cross-sections or other details of the interaction are not known can be "mapped" to known particle combinations. For example, neutral kaon  $K^0$  interactions are treated in the same way as  $K^+$  interactions, substituting its quark content  $u\bar{s}$  with  $d\bar{s}$ . To retain the compatibility with the DPMJET interface, this multi-projectile extension does not involve changes of the user interface. The typical initialization chain

1. `CALL PHO_INIT()`, initialize default parameters
2. `CALL PHO_SETPAR(1, ...)`, set particle on side 1
3. `CALL PHO_SETPAR(2, ...)`, set particle on side 2
4. `CALL PHO_EVENT(-1, ...)`, calculate cross-sections
5. `CALL PHO_EVENT(>0, ...)`, generate event

is therefore unaltered, but the responsibilities of the subroutines have shifted. Instead calculating the cross-section up to the energy of the current projectile-target combination when calling `PHO_EVENT(-1, ...)`, only the global maximum of  $\sqrt{s}$  is stored. Later the cross-sections are calculated during the first event generation call `PHO_EVENT(>0, ...)` for the current projectile-target particle combination. If during the event generation loop an external program calls `PHO_SETPAR` to change the projectile, the event generation call detects the change and checks if the tables for this particular combination exist in memory in the subroutine `PHO_SETPCOMB` (set particle combination). If yes, the common block variable `IDXMPAR`, the current combination index, is set to the appropriate value and the event generation continues. In the contrary case the code

locates a free index, loads parameters and writes the cross-sections in the common blocks which depend on `IDXMPAR`. This approach has the advantage, that switching between the particle combinations after they have been initialized is instantaneous and there is no need to change external interfaces. The changes are propagated into DPMJET by including the `POBEAM` common block and by extending the dimension of the directly accessed arrays.

## 7.4 Modifications for cascades and very high energies

### 7.4.1 Proton-proton cross-sections

As outlined in section 7.2, a Monte Carlo generator for cascade codes is subject to certain requirements. A stricter requirement is the ability to extrapolate to ultra-high energies above hundreds of TeV in center-of-mass. Figure 7.1 shows a comparison of total, elastic, inelastic and diffractive cross-sections between the old and the new PHOJET versions. The same result applies to DPMJET since it uses PHOJET tables.

The internal cross-section model is fitted to data using a modified version of the D507 least-squares minimization routine from the CERNLIB program library<sup>18</sup>. The free parameters of the fit are a set of Regge theory parameters, such as the pomeron and the reggeon intercept, the couplings and the slopes. Although the old fit program has performed relatively well, it can not compete with the flexibility and the performance in simultaneous fitting of multiple parameters of a true minimizer, such as Minuit<sup>19</sup>. The main advantage is that the minimization function, the individual weights and the graphical representation of the results can be viewed and modified in a single work-flow, instead of the classical approach of creating textual input control cards, running the fit, saving the output and parsing the file with some graphical tool. The modifications of importance weights and the inclusion or exclusion of experimental data can be set during run-time.

The goal of the fit is not meant to find the global minimum. It can be seen more as a method to weight the importance of various, more complex, interdependencies inside the full model according to trends and the absolute measures in their appropriate units. For example, assume that the parameters of the hard (QCD) cross-section are fixed. Theory predicts that the energy behavior of this minijet cross-section is steeper than the observed power-law behavior of the total and inelastic cross-sections. Due to the conservation of unitarity in the eikonal approach, the steep rise is compensated by higher-order corrections, such as multiple partonic interactions or multiple soft pomeron exchanges. By fitting the free model parameters to data, the amount of these

---

<sup>18</sup><http://cernlib.web.cern.ch/cernlib/>

<sup>19</sup>Original source <http://www.cern.ch/minuit> and its PYTHON wrapper iMinuit <https://github.com/iminuit/iminuit>

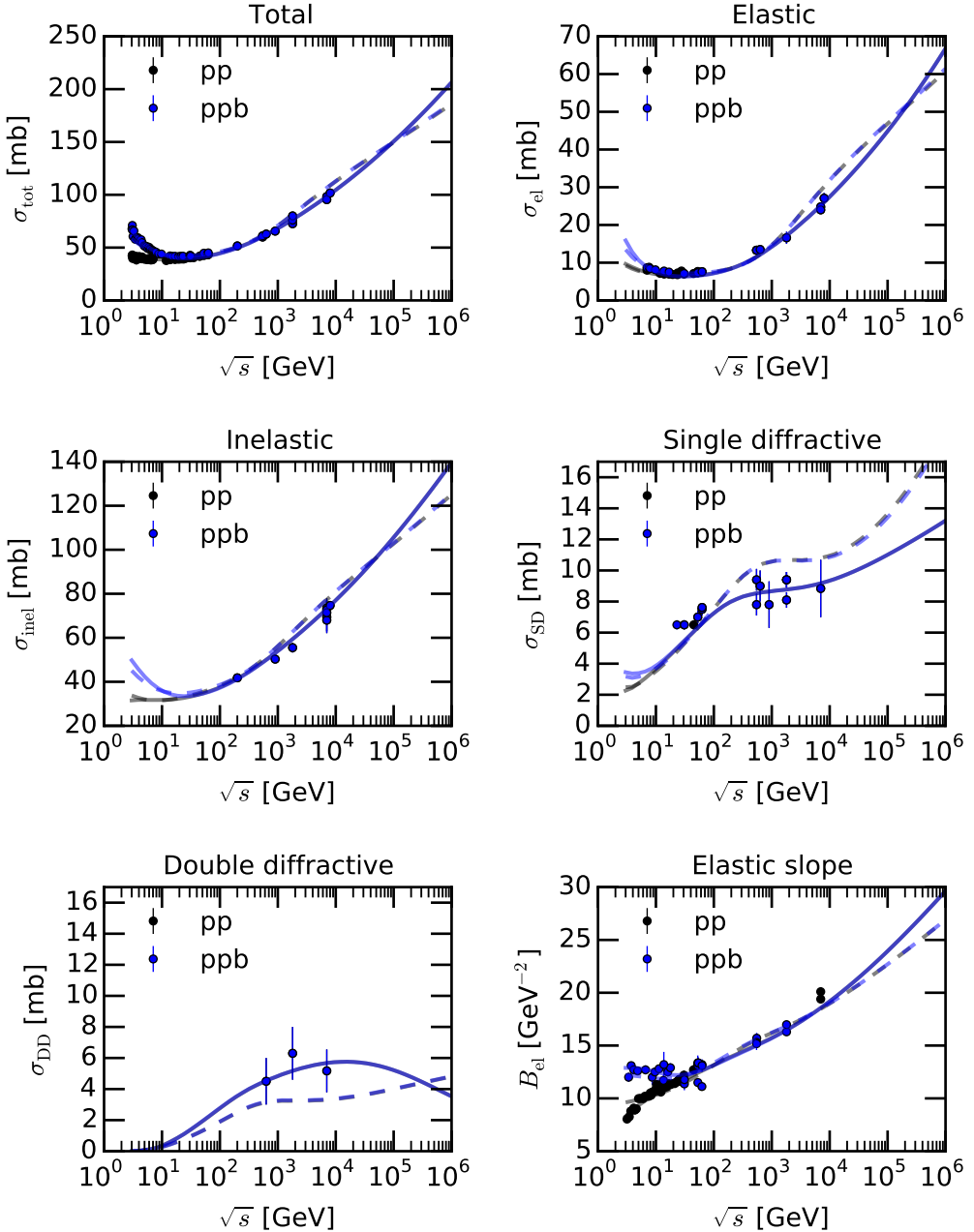


Figure 7.1: Total, elastic, inelastic, diffractive cross-sections and the elastic slope. Solid lines correspond to the new model and dashed to the old PHOJET. Lower energy data are taken from a compilation published in [50]. Data points at LHC energies are from [136, 25, 131, 11, 91]

corrections is fixed for one certain set of non-free parameters, in this case the QCD parameters. There is therefore typically more than one minimum. Due to complexity of the Monte Carlo program, these corrections must necessarily propagate to the relevant final state distributions since constraints, such as phase-space limitations, are only effective during event generation.

The fit result in Figure 7.1 reveals the following information:

- the behavior of the cross-sections is smooth and is compatible with Regge-type power-law behavior,
- the total cross-section, returned by the model's subroutines, is properly normalized to measures in millibarn and fits into experimental trends,
- the abundance of the contributing scattering processes, such as the various diffractive topologies, the elastic or the inelastic scattering is realistic.

After each change of model components concerning either the QCD part or formulas involved in cross-section calculations, a new set of parameters has to be obtained through fitting.

#### 7.4.2 Meson-nucleon cross-sections

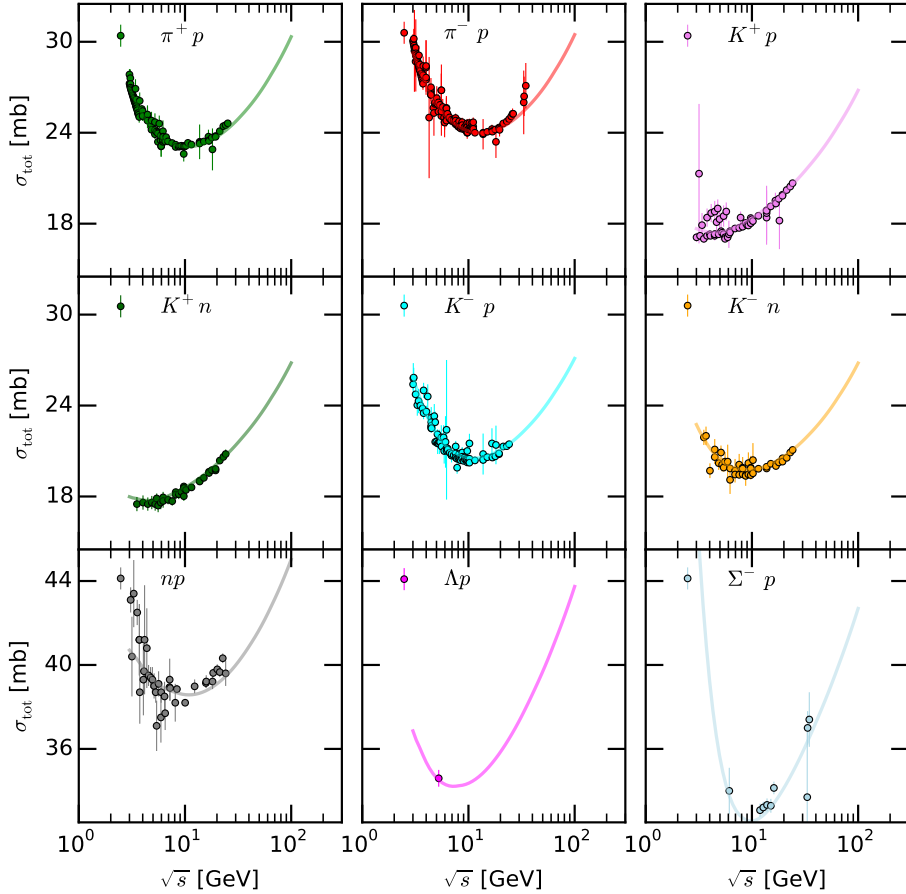


Figure 7.2: Total cross-sections of supported projectile-target combinations in PHOJET. Data points are taken from a compilation published in [50].

The original version of PHOJET does not ship with parameter sets for pion-proton or kaon-proton interactions. DPMJET contained a work-around type of implementation, where mesons behave according to the proton parameters with

the exception of a modified valence quark content. The FLUKA code does not make use this feature and instead falls back to its internal two-string model, which is insufficient to describe particle interactions at very high energies above 10 - 100 TeV in laboratory frame.

Together with the multi-particle extension, PHOJET and DPMJET contain new sets of parameters for the following projectile-target combinations:  $pp$ ,  $np$ ,  $nn$ ,  $p\bar{p}$ ,  $\pi^\pm p$ ,  $K^\pm p$ ,  $K^\pm n$ ,  $K^0 p$ ,  $K^0 n$ ,  $\Lambda p$ ,  $\Sigma^- p$ . The Figure 7.2 shows a compilation of the fit results. Since high-energy data are not available for most of the projectiles, the parameter sets are derived from the results of the  $pp$  and  $p\bar{p}$  fits with a modified low-energy part. At low energies the highest contribution to the total cross-section comes from effective Reggeon exchanges. Fitting just the pomeron-particle coupling  $g_{P,0}$  and the reggeon-particle coupling  $g_{R,0}$  on the non-proton side plus the Reggeon intercept  $\alpha_R$  turned out to be sufficient in most cases.

For obtaining good fits to pion-nucleon cross-sections without running into issues with negative eigenvalues of the two-channel matrix, the effective resonance mass in the two-channel low-mass diffraction formalism has to be lowered from 1.1 GeV to 0.5 GeV.

## 7.5 New parton density functions

The calculation of the QCD (see Eq. (7.2)) cross-section relies on parameterizations of the longitudinal momentum distributions of the partons inside the hadron. These functions are called parton density functions (PDFs). For the calculation of inclusive cross-sections, such as  $\sigma(pp \rightarrow c\bar{c})$ , they are a key ingredient for the determination of shapes and normalizations. Typically the codes return  $f_{q_f}(x, Q)$  the probability to find a gluon or quark with flavor  $q_f$ , the fraction of the total hadron momentum  $x$  at a virtuality scale  $Q$ . PHOJET contains QCD matrix-elements only at leading order, as all of the general purpose Monte Carlo programs. Higher-order radiative corrections are approximated with virtuality ordered parton showers as in PYTHIA 6.x.

PDFs exhibit constraints by experiment only in limited kinematical domains. These domains depend on the type of the experiment, the projectile and target combination and the capability of the detectors to resolve certain inclusive processes. The small- $x$  region, probed by HERA and LHC, can only be observed through the measurement of the exclusive  $J/\Psi$  production at high rapidities [51]. In cosmic-ray applications, where interaction energies can reach  $10^{21}$  eV, very small  $x$  become important. Figure 7.4 shows the range of partonic  $x$  values as a function of the interaction energy, calculated using the inequality  $\hat{s} = x_1 x_2 s \geq 4p_\perp^2$ . At very high energies the PDF library has to extrapolate down to values  $x \sim 10^{-9}$ , seriously restricting the choice of suitable sets. A review on the topic of parton distributions can be found in [51].

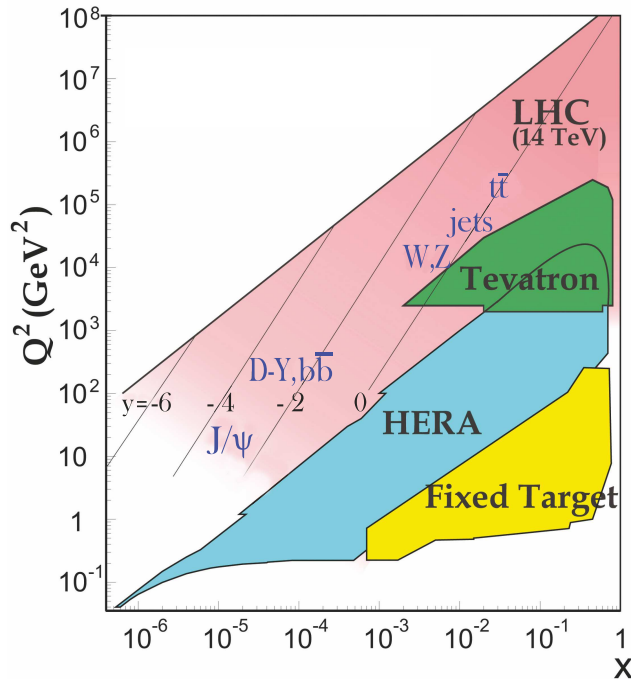


Figure 7.3: Kinematical domains in  $x$  and  $Q^2$  produced by collider and fixed target experiments [106].

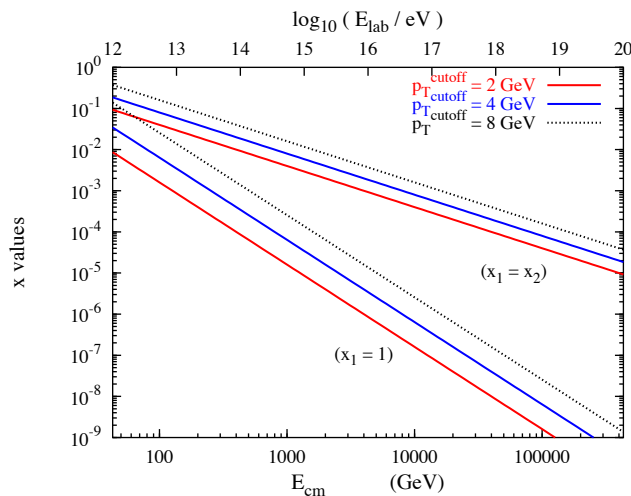


Figure 7.4: Domains of  $x$  relevant for the minijet cross-section calculation for different values of  $p_T^{\text{cutoff}}$ . Figure by R. Engel.

### 7.5.1 Choosing a PDF for very high energy applications

In the current landscape of particle physics dozens of different PDF sets and libraries are available. Typically PDFs are distributed as a numerical grid file and an interpolation program, such as the popular LHAPDF 5<sup>20</sup>. At the time of writing LHAPDF lists 480 different sets for download<sup>21</sup>. Although many

<sup>20</sup><http://lhapdf.hepforge.org/lhapdf5/>

<sup>21</sup><http://lhapdf.hepforge.org/lhapdf5/pdfsets>

of these sets are variations within the same family, there is still a remarkable number of distinct set families available and it is not a priori clear how to choose a good set for cosmic ray event generators. The PDF set has to fulfill the following criteria:

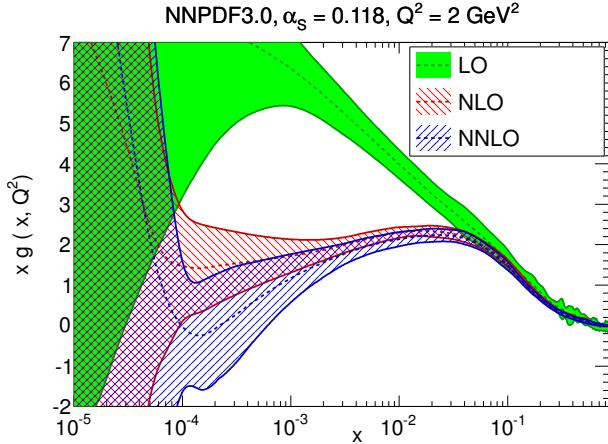


Figure 7.5: Comparison of the gluon distribution in NNPDF3.0 for different perturbative orders of the evolution [32].

- I) The multiplicity of minimum-bias events at LHC is already dominated by  $gg$  interactions at  $x$  values between  $10^{-4} - 10^{-6}$  [89]. At higher energies where the differences between the sets are becoming larger even smaller values down to  $10^{-9}$  are probed. The grid files and the interpolators have to be capable to extrapolate smoothly down to smaller  $x$  as far possible, even if no constraints from data exist.
- II) Since the QCD calculations in the Monte Carlo are using leading-order (LO) matrix-elements, the PDF needs also to be at LO, i.e. evolved using LO DGLAP splitting functions. This argument originates from the approach how the parton densities are obtained from fits to data using DGLAP evolution at a certain fixed order [122]. The fit relies on the fact that the higher order matrix elements are present in the calculation, meaning that the minimization is strictly valid only in this case. In practice the differences between using LO or NLO in a general purpose Monte Carlo might be not large, since an event generator can be often re-tuned to reproduce minimum-bias or underlying event distributions. Various tuning experiments for the evaluation of PDFs with the PYTHIA 8 Monte Carlo are summarized in [89]. Another counterintuitive consequence of higher-order PDFs is that densities can become negative as demonstrated in Figure 7.5. NLO or NNLO matrix-elements compensate this fact due to alternating signs of corrections, while in a LO interpretation this behavior is unphysical and certainly produces unexpected behavior in Monte Carlo generators.

III) A purely technical requirement is the availability of the interpolation program as a stand-alone code. In case the event generator is embedded in a larger framework, such as FLUKA or CORSIKA, linking with e.g. LHAPDF would introduce additional dependencies and version conflicts. The additional effort for maintenance over a typical major version lifetime of ca. 10 years should therefore be avoided where possible.

After filtering the list of available post-Tevatron models according to the above criteria, only four suitable PDF sets remain:

1. CTEQ-TEA (CT) 14 LO [57]: successor of CT09, includes LHC data,
2. CTEQ-TEA (CT) 09 MCS [94]: successor of popular CTEQ6 PDFs, uses pseudo-data from NNLO calculations,
3. GJR 08 VF (LO) [72]: successor of GRV98, specially designed for small- $x$  applications, uses latest HERA and Tevatron data,
4. GRV 98 LO [71]: dynamical parton distributions with emphasis on small- $x$  physics, achieved good prediction of  $J/\Psi$  production at HERA
5. NNPDF 3.0 (LO) [32]: flexible parametrization, derived from neural-network minimization, high attention to error bands and statistics.

There is a surprisingly high competition between researchers in providing PDF sets and deriving uncertainties. The sets listed above have slightly different goals. The neural-network PDF Collaboration (NNPDF) attempts to be "free of model bias" as far as possible by using cubic Hermite polynomials for interpolation instead of assuming more model motivated functional forms. In the CTEQ family of PDFs the traditional parameterization for each flavor is

$$x f_a(x, Q_0) = x^{a_1} (1-x)^{a_2} P_a(x). \quad (7.1)$$

$P_a$  is smooth and slowly varying, chosen as an exponential of a polynomial in  $x$  or  $\sqrt{x}$  in previous analyses or as polynomial in  $\sqrt{x}$  in the more recent analyses. This approach is guided by Regge behavior for  $x \rightarrow 0$  and by quark counting rules for  $x \rightarrow 1$ . On the other hand, the parametrization in NNPDF does not impose such strict constraints on smoothness and gains the advantage to achieve a better global goodness of fit. Outside of experimentally covered domains this approach can lead to some sort of substructure (wiggles), which are neither expected nor excluded by theory. When the total uncertainty of the sets is taken into account the differences between the sets diminish and all sets tend to produce smooth bands. Although NNPDF3.0 significantly improved the smoothness of the central value compared to NNPDF2.3, it is still not as smooth as the CT family. Since PHOJET calculates a numerical integral over the entire phase-space of the PDF's central value during each initialization, it can lead to problems with precision due to the fixed integration step-size on the relatively coarse, performance optimized grid. PHOJET and similar generators

do not make use of PDF uncertainties, thus preference should be given to a set with a robust central value prediction rather than sophisticated error band estimations.

Concluding from the arguments above, the CT14 leading-order PDF set is well suited for application in general purpose Monte Carlo generators at very high energies, such as LHC, FCC and cosmic rays.

### 7.5.2 A comment on Generalized Parton Densities

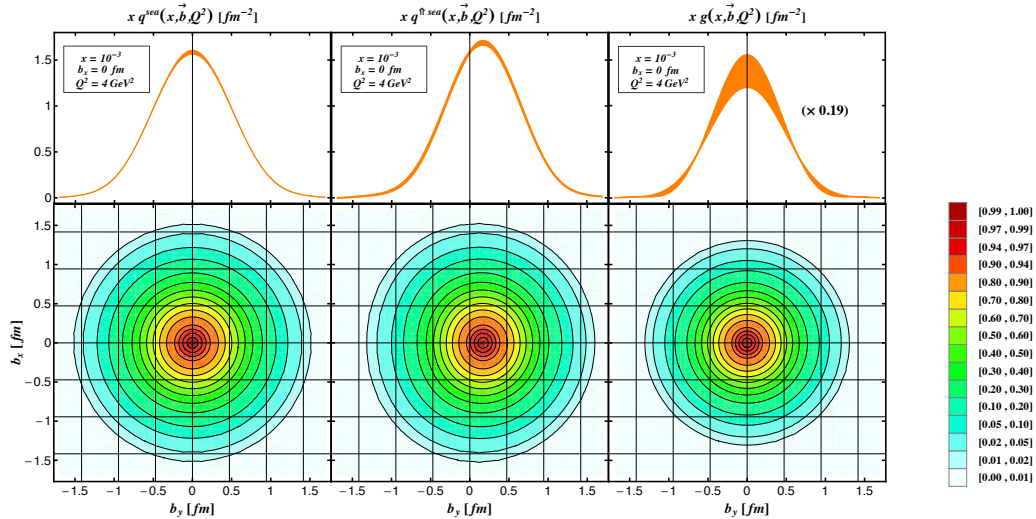


Figure 7.6: Parton densities at  $x = 0.001$  and  $Q^2 = 4 \text{ GeV}^2$  versus impact parameter  $b$  were obtained from a combined least-squares fit to the HERA collider and EIC pseudo data in LO approximation: relative densities (lower row) and their values at  $b_x = 0$  for the unpolarized sea quark parton densities of a unpolarized proton (left), a transversely polarized proton (middle), and the unpolarized gluon parton density of a unpolarized proton (right), its value is rescaled by a factor 0.19. Figure is taken from [102].

In the recent years some significant progress has been made in determining the transverse partonic structure of nucleons in deeply virtual Compton scattering (DVCS) and deeply virtual meson production (DVMP). This research is guided by two main branches of interests [102]:

- understand the spin decomposition of the proton in partonic degrees of freedom and
- understand the partonic density in the transverse degree of freedom.

Traditional PDFs, in the so called infinite momentum frame, describe only the distributions of longitudinal parton momenta. They apply only in the case where  $\hat{p}_\parallel \gg \hat{p}_\perp$  and lack the detail in the description of soft, peripheral partons. This picture implies that the proton in perturbative QCD is point-like

and has no transverse extension. As we know from elastic scattering or angular correlation studies this is at all energies not true. This approximation is sufficient if an inclusive hard high- $p_T$  process is of interest, such as the creation of Higgs-bosons in  $gg$  fusion or weak boson production. To be able to simulate realistic final states with multiple partonic interactions or nuclei involved, all minimum-bias and cosmic ray generators assume a functional form for the transverse extension of the nucleon as a function of energy. Motivated from elastic scattering experiments, these functional forms resemble either the electrical appearance of the nucleon by using dipole form factors or some strong matter blob by using gaussian or exponential shapes. Until now, an unambiguous partonic picture of elastic or diffractive scattering has not yet emerged.

Compared to the history of traditional PDFs, the GPD theory and experiments are very new. On the theoretical site, sufficient model understanding and working mathematical frameworks seem present. However, their model character requires a much larger set of data in more kinematical domains, before any competitive global GPD analysis can be carried out. As a vision and the hope to be able to describe exclusive states, finally bridging perturbative and non-perturbative QCD, GPDs are prominent candidates but they are not yet there.

### 7.5.3 New standard PDF for PHOJET

Before the start of the LHC Run-II several groups released updated sets incorporating LHC Run-I data. As argued above, minimum-bias events do not depend very strongly on the absolute choice of the PDF and many of its features can be absorbed into parameter retuning. First of all, because the absolute value of hard QCD cross-section strongly depends on the free  $p_T^{\text{cutoff}}$  parameter and second, because details of partonic final states are smeared out by hadronization and final state radiation in later steps of event generation. Choosing a high-quality PDF is still not meaningless, since the behavior of the energy-dependent  $p_T^{\text{cutoff}}$  strongly influences the multiplicity of minijets at cosmic-ray energies. In this sense, incorporating the latest PDF can be seen as additional guidance by data.

After the CTEQ-TEA group published the CT14 LO set, the choice fell strongly in favor of it. The equivalent competitor NNPDF3.0, although suitable for this application, produced numerical inaccuracies using the central value. The GJR sets were not yet exposed to LHC data and could therefore be of smaller value. As it can be seen in Figure 7.7, the up-quark distributions are vastly similar. Down-quarks in CT14 gained some substructure at  $x \sim 10^{-2}$  and are significantly lower compared to its predecessor CT09 and the dynamical PDFs. The CTEQ-TEA group argues that to a large extent the measurements of the  $W$ -boson's charge asymmetry lead them to this result [57].

Another advantage of the CT sets is the smaller gluon density at very small  $x$  when compared with GJR. Although the accuracy of both results is ques-

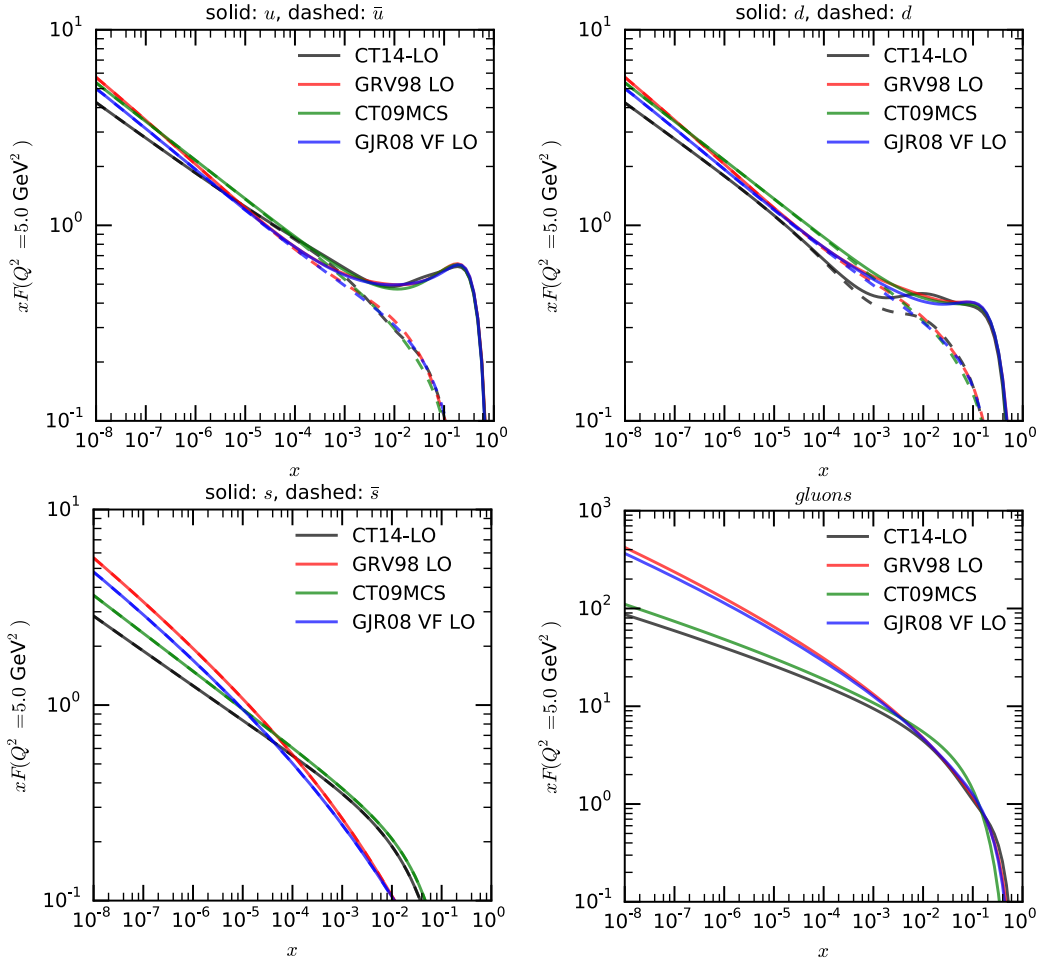


Figure 7.7: Candidate parton densities at low  $Q^2 \sim \hat{p}_{T,min}^2$ .

tionable without appropriate data, fewer soft gluons are an advantage when extrapolating to high energy, since the model needs to correct less for phase-space limitations and realizable final states.

At higher virtualities  $Q^2$  the differences between the CT14 and CT09 or GJR08 and GRV98 vanish, respectively. This is due to the fact, that at higher virtualities perturbation theory fully applies and the DGLAP equations become exact. The similarity between GRV98 or GJR08 stems from the way how the dynamical PDF is constructed. Its behavior is determined by the choice at a small initial virtuality scale  $Q_0 = 0.5$  GeV and then evolved using DGLAP.

The net effect on minimum-bias distributions at LHC is demonstrated in Figure 7.8. Charged particle pseudo-rapidity distributions in the central part of the detector show an increase in multiplicity by more than 10% when going back from CT14 to CT09. On the other hand the average transverse momentum as a function of multiplicity does not show any significant change. These and other observations confirm what has been already claimed by the PYTHIA 8 group [89], that although the differences can be big, in most cases, they can be absorbed by re-tuning of parameters.

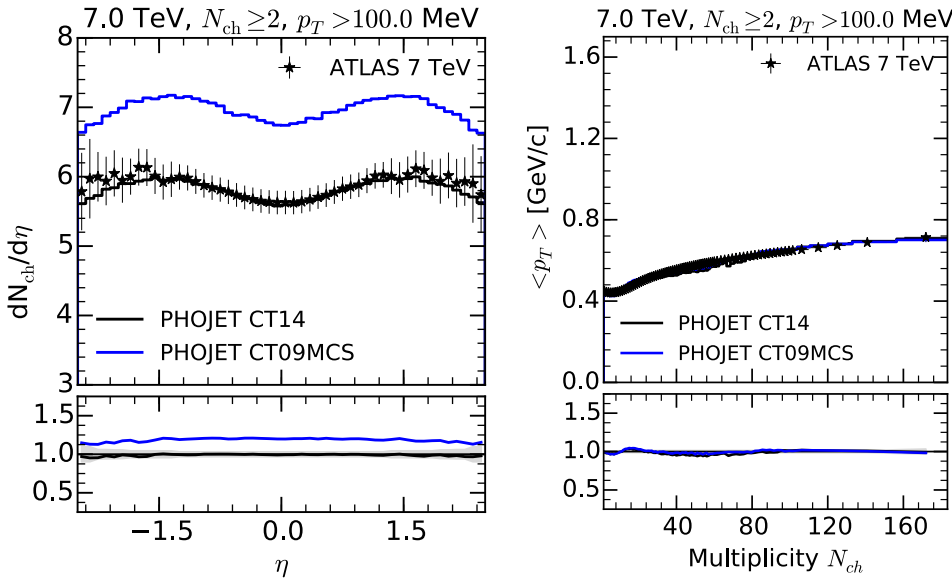


Figure 7.8: Effect due to the change of PDF on charged particle minimum-bias distributions in PHOJET using a tune for CT14. The CT09MCS distributions are generated with parameters of the CT14 tune. Measurements performed by ATLAS [3].

## 7.6 Insight in the energy dependence of the hard cross-section through LHC data

In the old version of PHOJET the  $p_T^{\text{cutoff}}$ , defining the perturbative scale, grows with energy as a function of  $\log \sqrt{s}$ . This purely phenomenological parametrization is motivated by the fact, that at very high energies at tens or hundreds of TeV in center-of-mass frame, the dense partonic matter in the interaction region prevents the scattered partons from escaping without re-scattering or additional interactions. It is not clear anymore that scatterings resulting in a  $p_T \sim 2.5$  GeV can be considered as perturbative processes. In fact, there is no unambiguous guidance from theory what is a sufficiently high transverse momentum and where the separation between the technical terms "soft" and "hard" lies.

### 7.6.1 Hard cross-section and multi-parton interactions

The need to find a robust approach to this question stems from the energy dependence of the  $2 \rightarrow 2$  QCD cross-section

$$\sigma_{\text{QCD}} = \sum_{i,j,k,l} \frac{1}{1 + \delta_{kl}} \int dx_1 dx_2 \int_{Q_{\min} \propto p_{\perp}^{\text{cutoff}}} dQ^2 f_i(x_1, Q^2) f_j(x_2, Q^2) \frac{d\sigma_{i,j \rightarrow k,l}}{dQ^2}, \quad (7.2)$$

where  $x_1, x_2$  are the longitudinal momentum fractions of the incoming partons  $i, j$ ,  $Q$  the virtuality or the momentum transfer of the process,  $\sigma_{i,j \rightarrow k,l}$  the leading-order QCD matrix elements, and  $f_i, f_j$  the density (PDFs) of flavor  $i$

partons in the incoming particle on side 1 and  $j$  for the other particle, respectively. This equation makes use of the factorization theorem, since the density of partons is independent of the process and since there are no correlations between side 1 and 2 (no convolution of  $f_i$  with  $f_j$ ). Clearly, since there is no dependence on the impact parameter, the partons are assumed to be localized in a point-like region.

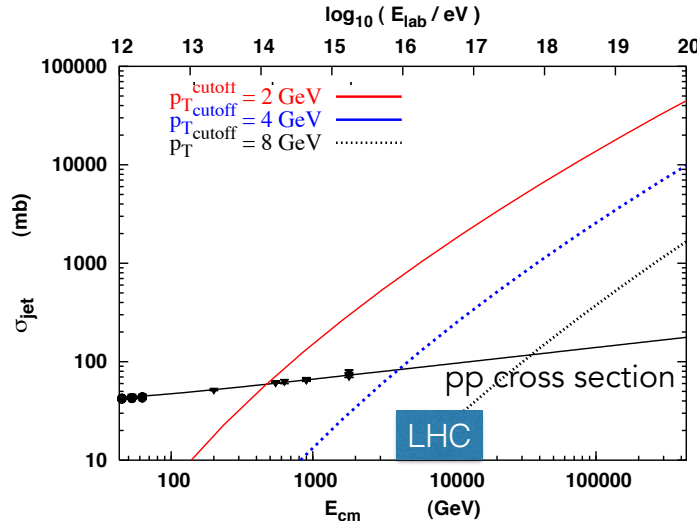


Figure 7.9: QCD cross-section compared with  $\sigma_{\text{tot}}$  in  $pp$  collisions for different values of  $p_T$  cutoff.

When looking at Figure 7.9 the next question is obvious: Why does the cross-section for a subset of scattering processes in a fraction of the phase-space exceeds the total interaction cross-section  $\sigma_{\text{tot}}$ ?

The most common explanation for this behavior are multiple partonic interactions with one hadronic collision (MPI). The integral (7.2) returns the cross-sections for the sum over all initial and final state pairs of partons. The simplest estimate for the average number of simultaneous partonic scatterings is

$$\langle n_{\text{di-jet}} \rangle = \frac{\sigma_{\text{QCD}}}{\sigma_{\text{ine}}} \quad (7.3)$$

This number emerges from a very simplified picture and can be considered at most as an upper limit for the case where all scatterings occur uncorrelated. From the theoretical point of view, there is still no unified description since the transverse structure of the nucleon at high energies is not well understood. Models in Monte Carlo generators, although based on the ideas above, achieve a higher detail due the direct influence on energy conservation and phase-space limitations. Shifting to explicit impact parameter dependence allows them to predict experimentally observable quantities, such as the jet-pedestal effect in the underlying event of hard collisions [127, 126, 34].

Although significant progress has been achieved in the past years, the event generator tunes obtained from comparisons with Tevatron data, were not performing too well and needed significant re-tuning to be able to describe LHC

underlying event data.

In PHOJET the number of multiple interactions is derived from the expansion of the exponential series of the eikonal (see chapter 6). The absolute value of  $\sigma_{\text{QCD}}$ , governed by the free choice of PDFs and the energy dependence of  $p_T^{\text{cutoff}}$ , is therefore a crucial ingredient for describing LHC data where MPI are evident.

### 7.6.2 New energy dependence of transverse momentum cutoff

Due to the lack of guidance on the value of  $p_T^{\text{cutoff}}$  from first principles, the choice for a new parametrization fell on predictions from the phenomenological dipole-model. In their studies of small- $x$  physics and saturation effects the authors of [73] propose that the transition between the "soft" and the "hard" regime has an energy dependence proportional to

$$Q_{\min} \propto p_T^{\text{cutoff}} \sim p_{T,0} \sqrt{s}^{\lambda_{\text{eff}}}. \quad (7.4)$$

The new energy dependence of the cutoff in PHOJET contains more degrees of freedom but keeping the idea of the Regge motivated power-law behavior

$$p_T^{\text{cutoff}} = p_0 \left( \frac{\sqrt{s} + p_1}{p_2} \right)^\lambda. \quad (7.5)$$

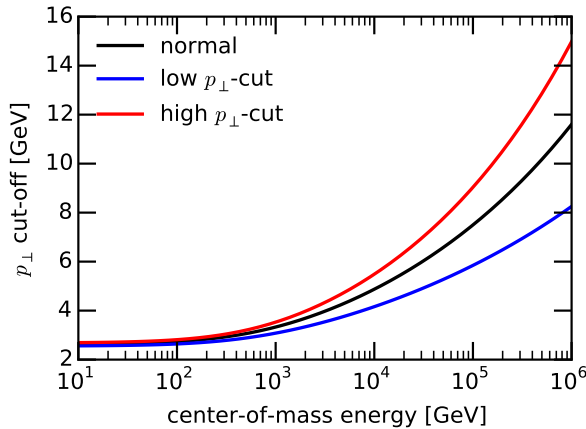


Figure 7.10: Three different choices of the  $p_T^{\text{cutoff}}$  in a Golec-Biernat-Wusthoff type parametrization.

The following study demonstrates the effect of parameter variations inside Eq. (7.5). For three different choices of the cutoff behavior, illustrated in Figure 7.10, PHOJET has been retuned by fitting the cross-section model to data. All three cases in Figure 7.11 represent satisfactory descriptions of data. Most differences appear at very high energies and in single diffraction at SPS energies. Another feature is the behavior of the total cross-section for a small

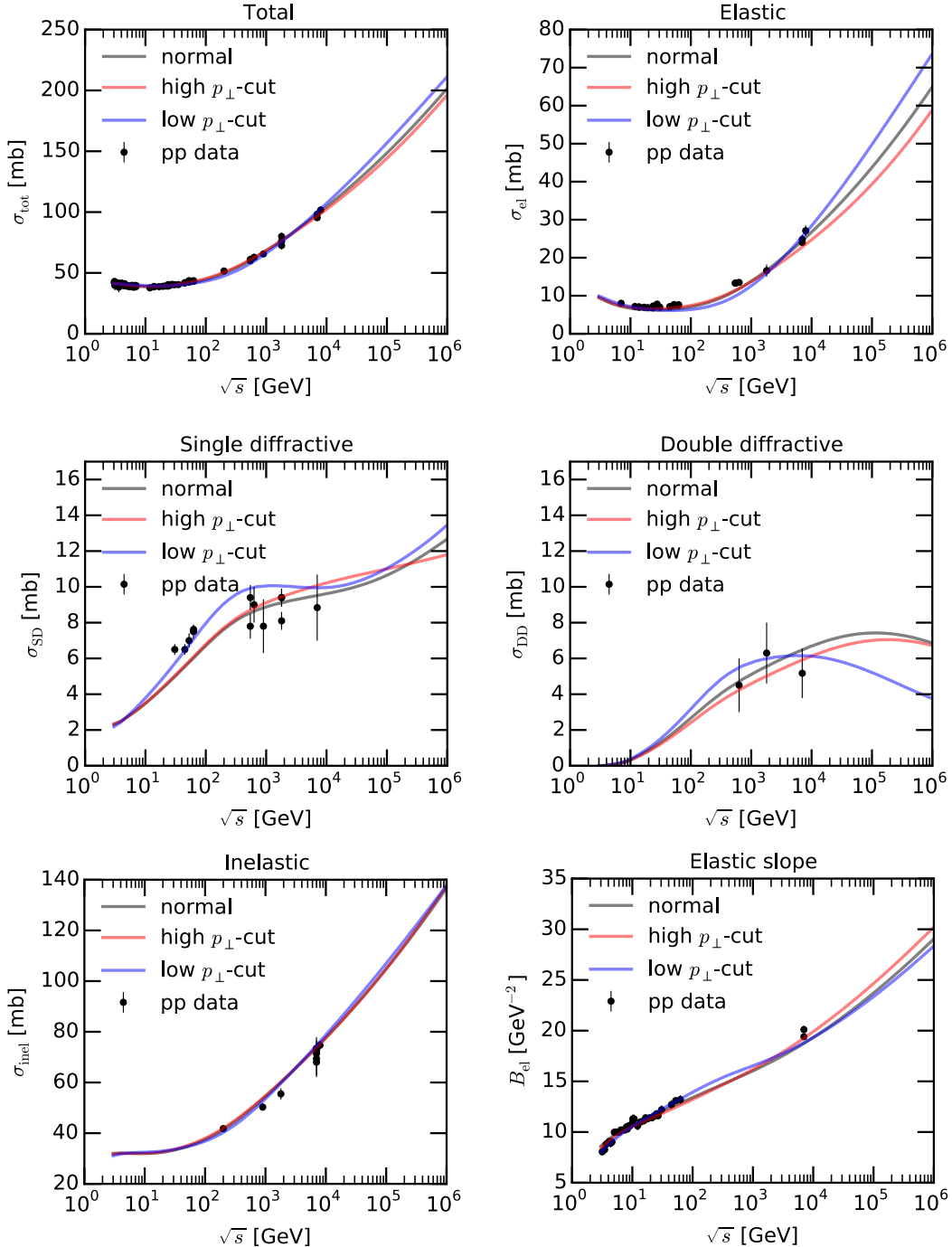


Figure 7.11: Cross-section fits in PHOJET according to three choices of the  $p_T^{\text{cutoff}}$  behavior. See Figure 7.1 for data references.

cutoff in the upper left panel of Figure 7.11. The functional form approaches a straight line rather than a curved power-law. Related to the  $\ln^2(s)$  expectation of the Froissart bound [39], the model becomes guided by unitarity constraints. The most obvious effect of MPI activity is the growth of the pseudo-rapidity plateau, sketched in Figure 7.12. At LHC energies one can therefore expect significant change of pseudo-rapidity distributions due to the violation of Feynman scaling in the central region.

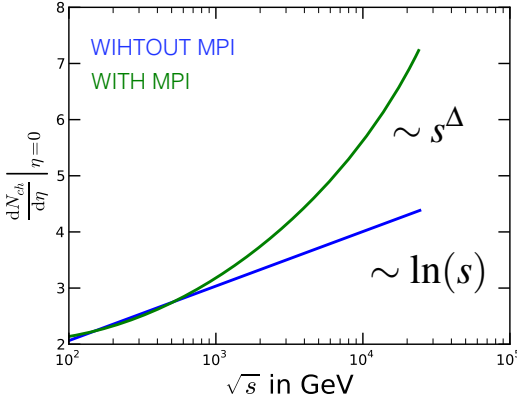


Figure 7.12: Higher values of  $\sigma_{\text{QCD}}$  should produce a higher MPI activity and therefore a stronger increase of multiplicity in the central region.

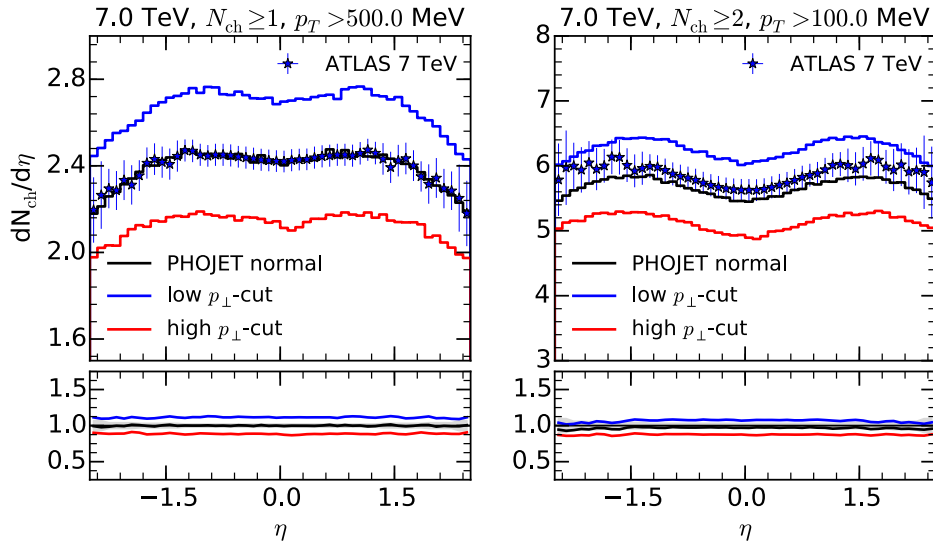


Figure 7.13: Charged particle pseudo-rapidity densities at 7 TeV for two different phase-space cuts. Measurement by ATLAS [3].

Figure 7.13 confirms the expectation, that the variation of the  $p_T^{\text{cutoff}}$  produces different scaling behaviors of the pseudo-rapidity plateau. With the higher cut on  $p_T > 500$  MeV, the left panels emphasize the role of hard interactions. In the right panels, where the lower cut on  $p_T$  permits more particles from the fragmentation of soft strings to contribute, the effect is milder.

The distributions in Figure 7.14 include very forward scattered particles. They confirm that the effect from the variation of hard cross-section is indeed limited to the central phase-space. In the left panel the particle density at TOTEM rapidities is practically unchanged. The measurement in the right panel, the range in rapidity without particles (gap) counted from the edge of the detector acceptance, is sensitive to various classes of diffractive scattering, in particular single diffraction. Although the diffractive cross-sections in the three model version slightly differ (central left panel in Figure 7.11), PHOJET doesn't show any statistically significant differences. The complexity of diffrac-

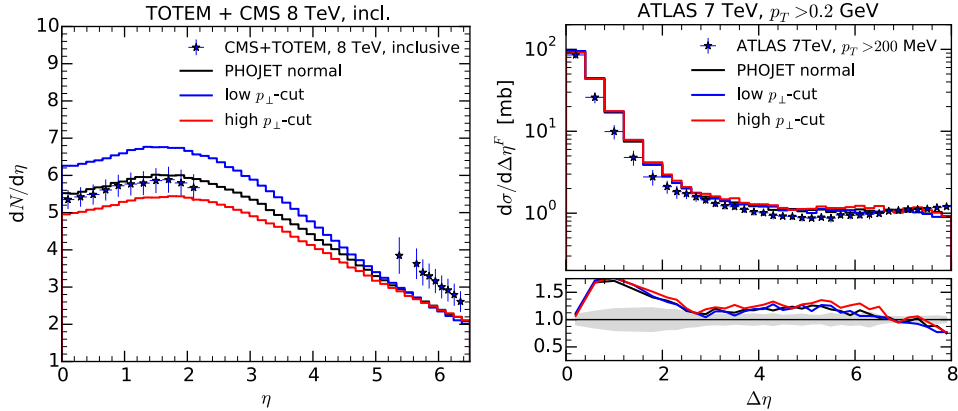


Figure 7.14: Examples of more forward distributions: (*left panel*) Combined CMS+TOTEM measurement over 7 units of pseudo-rapidity [47] and ATLAS measurement of forward gap size in diffractively enriched events [4].

tive final states in the model can easily smear out subtle parameter variations. Together with new cross-section fits and the new energy behavior, PHOJET

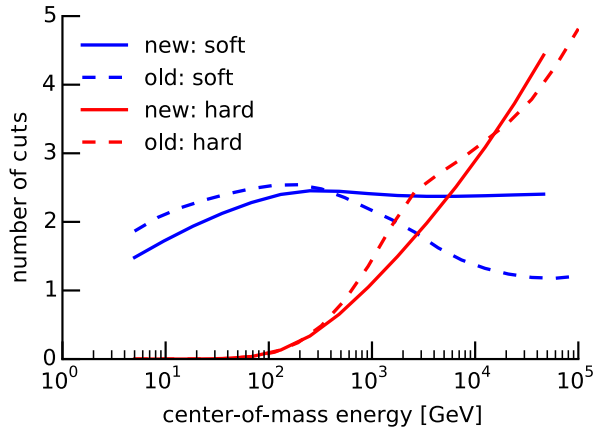


Figure 7.15: Distribution of the number of soft and hard pomeron cuts with new  $p_T^{\text{cutoff}}$  model and updated cross-section fits.

obtains a new distribution of MPI as shown in Figure 7.15. In addition, a more balanced choice of other parameters, in particular of those related to the triple-pomeron vertex, resulted in a smoother, feature-less behavior.

## 7.7 DPMJET vs. LHC data

For an event generator which was not maintained for more than 12 years, PHOJET (and DPMJET) performed very well in comparisons with LHC minimum-bias data at 0.9, 2.3 and 7 TeV. In this section, PHOJET and DPMJET were used as synonyms, since all data comparisons are made for  $pp$  collisions.

The two major problems were a low particle multiplicity in the central region

and the lack of very high multiplicity events ( $N_{ch} > 100$ ). A longer investigation revealed a truncation of the MPI probability distribution as the origin of the multiplicity deficit. A mechanism in PHOJET's subroutine PHO\_SAMPRB prevented the program running from out of array dimensions by rejecting states with too many soft and hard pomeron cuts. However, the arrays were dimensioned too little for very high energies. Increasing array dimensions repaired most of the distributions and revealed a "black disk like" curvature of the multiplicity probabilities (see chapter 6).

Very extensive comparisons with the majority of LHC minimum-bias data taken by all of the experiments have been performed. The program Monte Carlo ValiDation (MCVD) (see section A.7), generates a 40-page PDF file, with up to 8 comparison graphs per page. It gives more detailed comparisons of the models performance with respect to the various phase-space cuts of the experiments. Here, only a few a small selection of graphs can be discussed and it is beyond the scope of this chapter to present an extensive comparative study.

Transverse momentum related distributions are shown in Figure 7.16. The relatively high cut on  $p_T > 500$  MeV focuses the particle selection more on those which come from hard scatterings. At smaller multiplicities the average  $p_T$  in the upper plots is well described by the old and new models. In the old model, the lack of high multiplicity events decreases the average  $p_T$  because events with a high number of MPI are cut away. The lower plots show the  $p_T$  distribution in the whole pseudo-rapidity acceptance of ATLAS  $|\eta| < 2.5$ . The measurement has an impressive dynamic range of 9 orders of magnitude. The generators describe sufficiently well the  $p_T$ . The performance of the old model is remarkable and it took some effort to reproduce it with the updated model, since the updated version tends to overshoot at higher  $p_T$  when used with CT14 PDFs.

More forward distributions, as those in Figure 7.17, could be improved by re-adjusting the hard cross-section, the PDFs and MPI probabilities. In terms of cascade physics, the LHCb experiment is still rather central. The cut  $p_T > 200$  MeV biases the selection towards events containing hard scatterings. Therefore, the improved central multiplicities influence positively the forward distributions as well.

The pseudo-rapidity distributions in the left panels of Figure 7.18 are reasonably well described by both versions. Since ALICE' time-projection-chamber (TPC) can efficiently measure down to very low transverse momenta. This measurement is very sensitive to the production of particles with very small  $p_T$ , since the cross-section for higher transverse momenta is exponentially suppressed (compare with Figure 7.16). In this slice of the phase-space the old and the updated model perform very similarly. A significant deviation is visible at the tail of multiplicity distributions for previously discussed reasons. The multiplicity zero-bin is very difficult to describe. It incorporates information about diffraction, gap survival probability and in addition to the width of the  $p_T$  distribution.

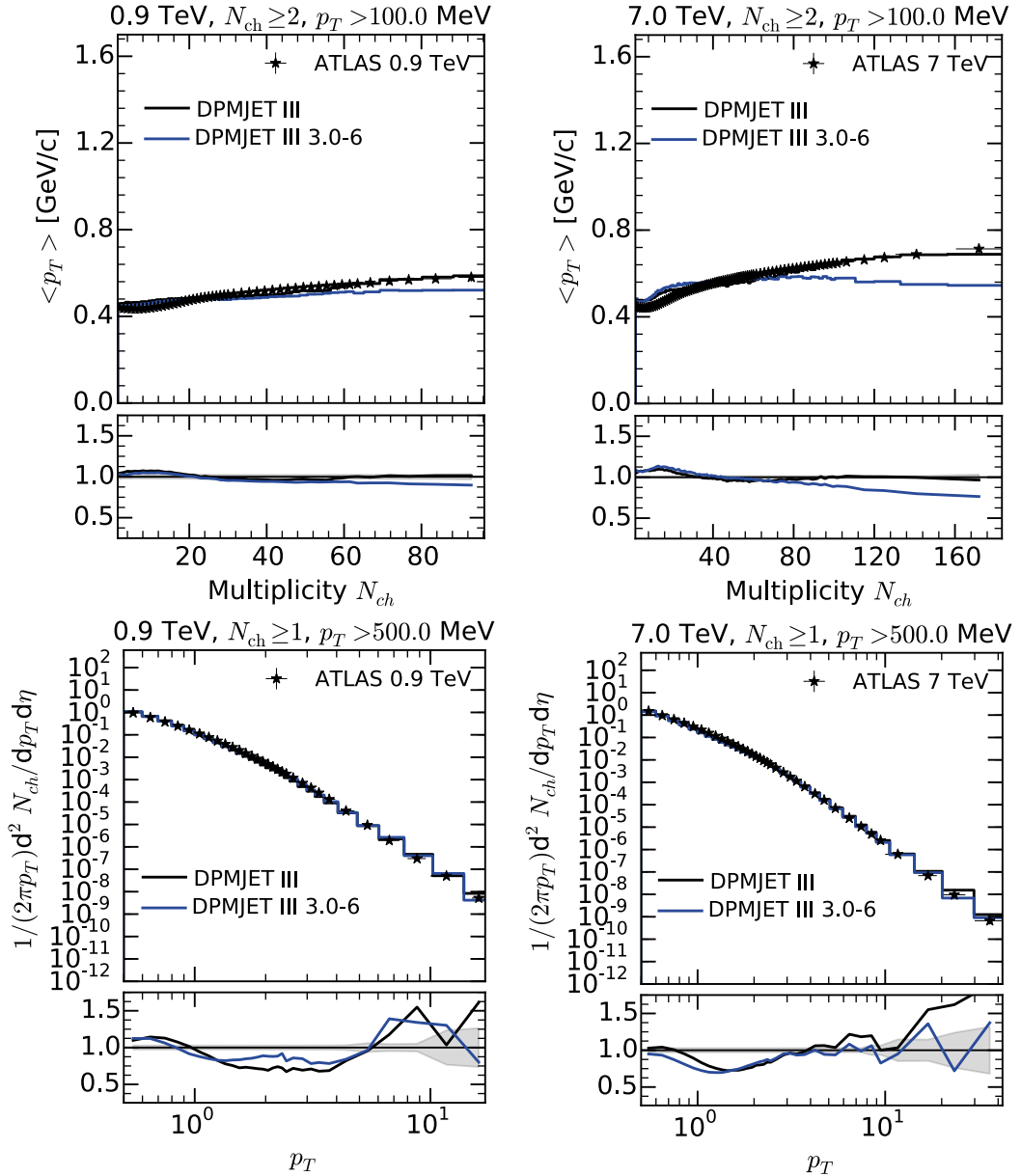


Figure 7.16: (top) Average transverse momentum vs multiplicity and (bottom) charged-particle transverse momentum distributions. DPMJET III 3.0-6 is the last public version and the other is the new version. ATLAS data [3].

Figure 7.19 demonstrates the qualities of this family of generators. Lorentz-invariant cross-sections are an important quantity. They combine the precision of the cross-section model together with soft and hard ranges of the transverse momentum distributions, instead of just the shapes. The data on this plot spans four generations of colliders, from ISR to the LHC. PHOJET and DPMJET both manage to describe the general features, however at higher  $p_T$ , both models tend to over-estimate the cross-section. If this is corrected for, by e.g. increasing the  $p_T^{\text{cutoff}}$  or by reducing the  $k$ -factor, than it is not possible to do it without sacrificing the precision in other places. On the other hand, the

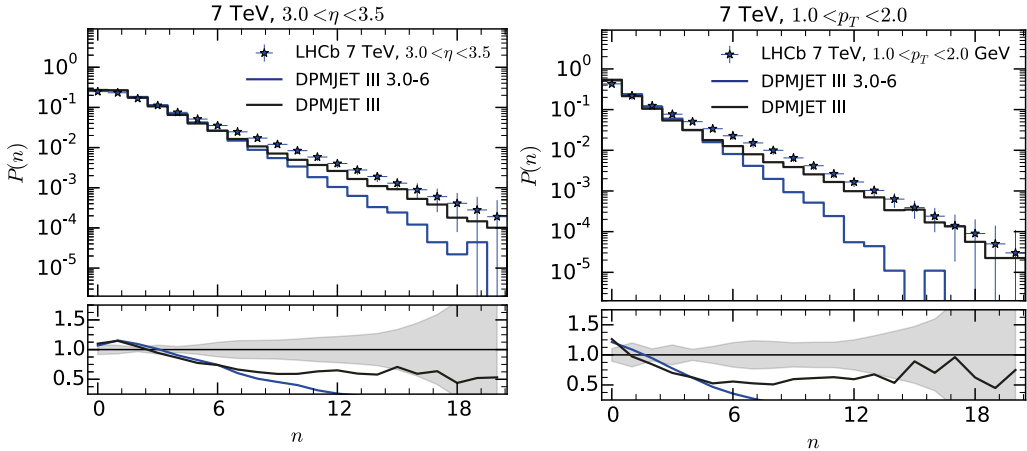


Figure 7.17: Comparison with forward multiplicity distributions at LHCb [133] for a pseudo-rapidity bin and for a  $p_T$  bin.

"soft" model parameters, like the width of the  $p_T$  assignment or the critical tension parameter in string fragmentation, are constant over the entire energy range. Other models, where these parameters are constant suffer from similar difficulties in the description across the entire energy range. In models like SIBYLL and EPOS many of these parameters are energy dependent, which make the model more elastic, but also less predictive. PHOJET and DPMJET are in this regard more conservative.

## 7.8 Discussion

Due to technical issues and model features the Monte Carlo event generators PHOJET and DPMJET could not be used recommended for calculations at very high energies beyond several tens of TeV in center-of-mass frame. Cascade and air-shower simulations for astroparticle physics were either limited by the covered energy range or by the lack of the possibility to treat secondary interactions within the same run of the program. The limitation of a single projectile-target combination per program initialization has been removed by modifying the way how cross-section tables and counters are stored. The new on-demand initialization scheme, or multi-particle extension, can store up to 20 particle combinations, switching between them in run-time without performance impact.

In light of new LHC data, the high energy behavior of the model has been reviewed. The new experimental results helped to find an unphysical, technical limitation, which was the origin of the lack of high multiplicity events. The availability of results in various phase-space cuts simplified the choice for the energy behavior of the  $p_T$  cutoff. Precise measurements of the total and elastic cross-section reduced the extrapolation ambiguity. The choice of a new standard PDF took a significant fraction of time, since many parameters needed to be re-tuned when going from the old GRV94 to the more modern CT09 and

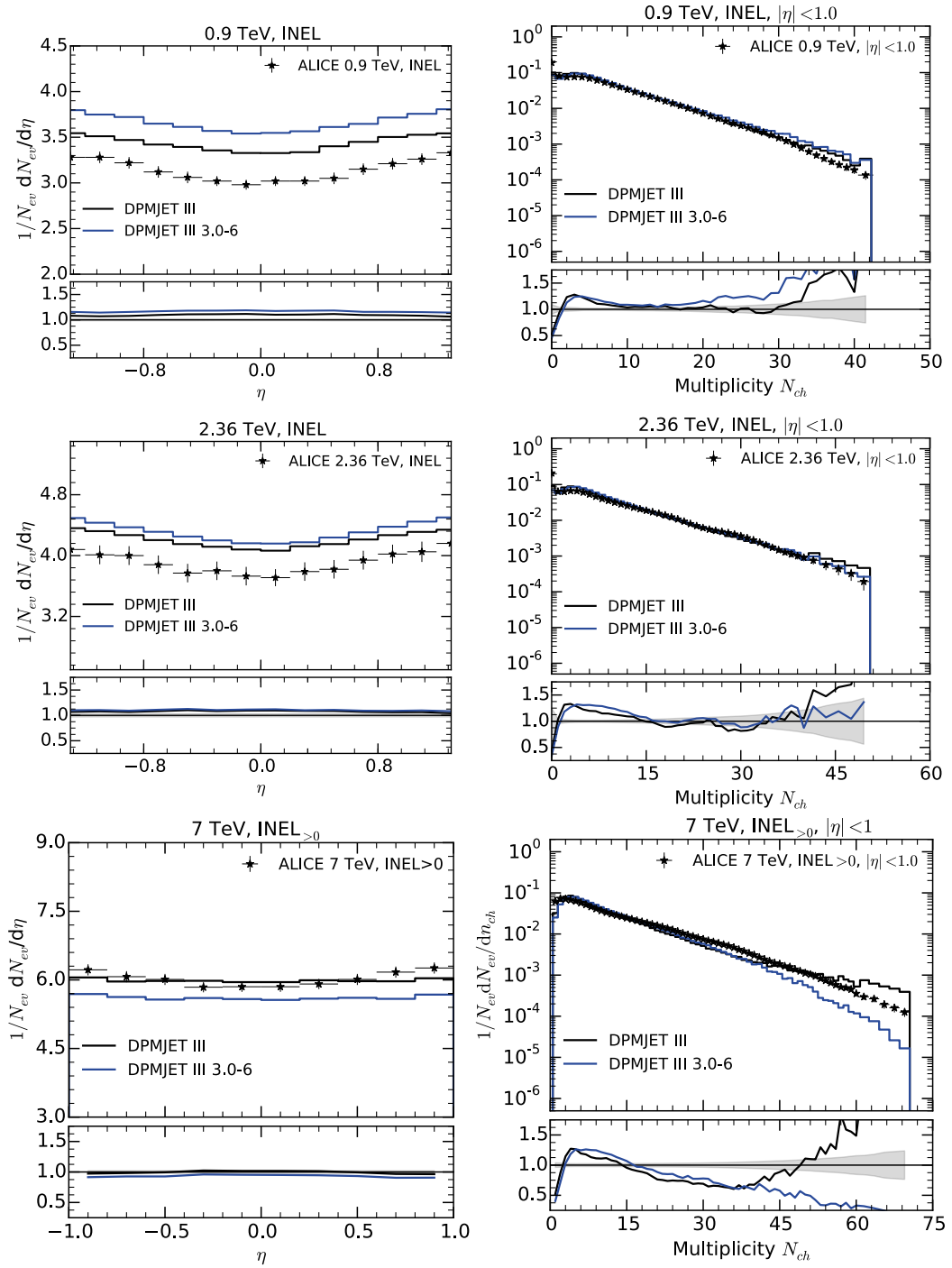


Figure 7.18: (Left) Charged-particle pseudo-rapidity and (right) multiplicity distributions for the INEL(astic) event selection. This measurement is for  $p_T > 0$  MeV by ALICE [6, 5].

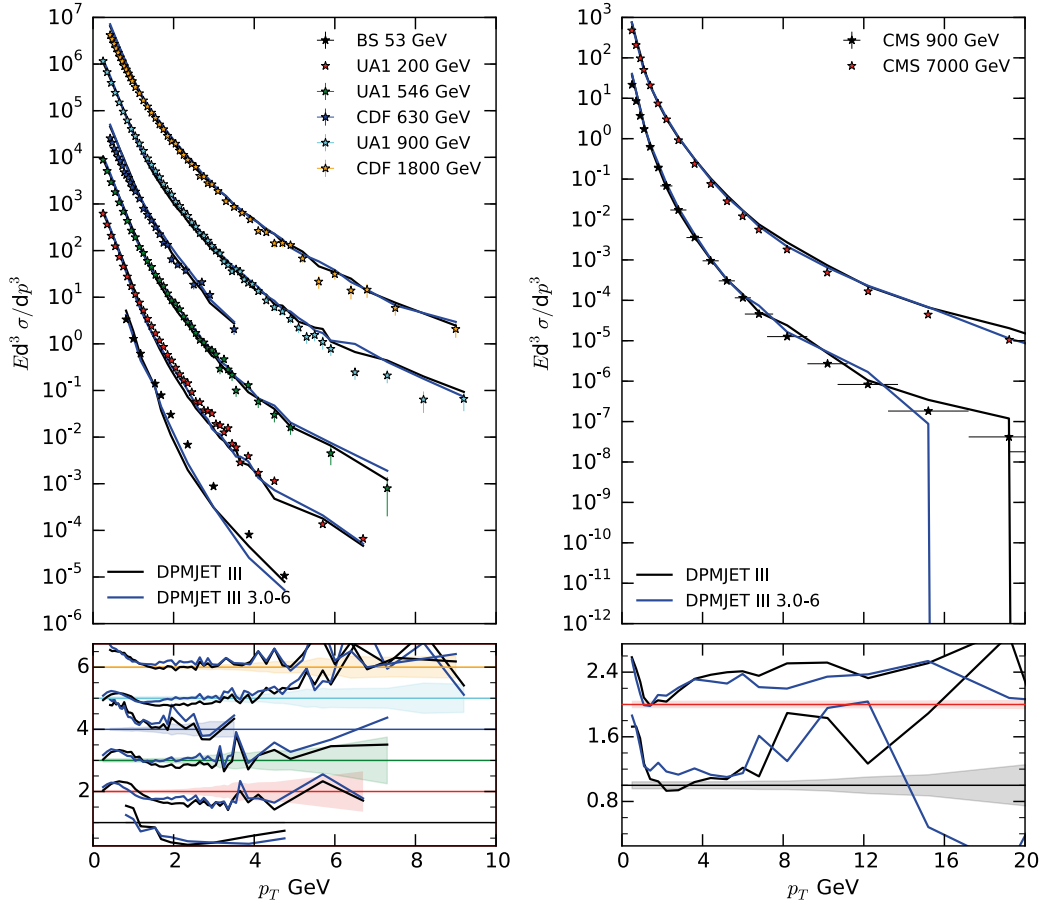


Figure 7.19: Lorentz-invariant differential cross-section in  $\text{mb}/\text{GeV}^{-2}$ .

later to CT14. Some additional tuning of fragmentation was also performed to improve the description of NA49 data.

DPMJET profited from all developments in PHOJET. The model in its recent state can be used in LHC, FCC and extensive air-shower simulations and, in principle in all kinds of cascade codes. The modifications produced no penalty on the execution speed. A crucial advantage of DPMJET, compared to EPOS for example, is the possibility to go as low as a few GeV per nucleon in the simulation of hadronic and nuclear collisions.

Of course, like all hadronic interaction models, PHOJET and DPMJET are far from being perfect. In particular DPMJET would need a major overhaul of the source code. This time the model was not rigorously tested against hadron-nucleus and nucleus-nucleus data, but it was done after 2006 when data from RHIC became available. There are still several unsolved questions regarding the energy behavior of the hard cross-section, screening and saturation effects (chapter 6). General tuning according to NA49 and NA61 fixed-target data on vector mesons and nuclear targets has also to be performed. The baryon Feynman- $x_F$  distributions are not as flat in the model as in the data. A model of remnant excitation which improved the baryon distributions has been implemented in the new SIBYLL-2.3 [117]. It could be realized in DPMJET

without excessive effort. Some features which are in the FLUKA version of the generator, such as chain fusion (color reconnection), could be ported back into the standalone version.



# Chapter 8

## Summary and outlook

This thesis discussed particle cascades in the atmosphere of the Earth and hadronic interactions of relevance for these cascades. The two central problems are an accurate simulation of the complex physics of particle cascades and a reliable description of particle production in high-energy interactions.

The traditional semi-analytical approach suffers from a number of approximations. To avoid these shortcomings a new framework, based on a matrix form on cascade equations, has been developed in this thesis. It gains several advantages compared to the integro-differential form of coupled cascade equations by

- preserving all couplings between individual particle species,
- not requiring approximations regarding the density profile or the geometry.

From studying the numerical stability, it was shown that under certain circumstances the equation system becomes stiff and the numerical integration requires very small step-sizes. This happens when processes with very different (time-) scales are coupled, i.e. when short-lived heavy flavor (prompt) hadrons are explicitly treated as particle species of the atmospheric cascade.

A generic method for the reduction of stiffness, the resonance approximation, has been developed and implemented as part of this high-performance solver of the matrix equations in a public open-source program MCEQ. When comparing the results to detailed Monte Carlo calculations, MCEQ achieves similar precision in inclusive flux calculations in a tiny fraction of time and with no statistical errors.

The solver has been applied to study several aspects of hadronic interactions in atmospheric cascades. We could confirm, that aside from the species which were discussed in the literature, no additional species contribute significantly to the flux. Conventional fluxes of leptons are dominated by decays of charged pions and charged or neutral kaons, while at high-energies promptly decaying particles are the main source of the fluxes. For neutrinos those include charged and neutral charmed  $D$  mesons, but also  $\Lambda_C$  baryons and charmed strange  $D_s$  mesons. Muons can in addition originate from rare decays of unflavored

mesons, mainly  $\eta$  and  $\phi$ . The competition between their small branching ratio, short-life time and abundant production results in a higher flux compared to the channels including charmed mesons. The flux of atmospheric  $\tau$  neutrinos is purely prompt and originates from decays of  $D_s$  and mostly secondary  $\tau$  leptons.

By exploring the relevant phase-space for inclusive lepton production, it was found that more than 40% of leptons originate from decays of particles which have been produced at high Feynman  $x_F > 0.4$ . The distribution of primary cosmic ray energies that contribute to the production of leptons with a certain energy is peaked at one order of magnitude higher energies with a long tail towards higher values. Inclusive neutrinos require typically a twice as high primary energy when compared to muons.

Precise atmospheric muon measurements were used to evaluate the calculation method using development versions of SIBYLL-2.3. It has been shown, that it is not only possible to obtain model corrections from studying accelerator data, but also from atmospheric muon measurements. By fitting model predictions to a large set of data, it was possible to obtain comparable correction factors for pion and kaon distributions, to those obtained from comparisons with fixed-target data at lower energies.

By carrying out predictions for conventional atmospheric neutrinos using different hadronic interaction models, large differences between the models were confirmed. Depending on the energy, the predictions differ by up to 10-30%.

Calculations of the prompt flux with DPMJET-III and SIBYLL-2.3 lie within error bands of actual perturbative calculations. The variation between the models is large, not exceeding an order of magnitude. However it has to be accounted for an additional, similarly sized uncertainty from the composition of the cosmic ray flux at ultra-high energies.

These large uncertainties motivated to improve the landscape of hadronic interaction models that can be employed in simulations of particle cascades. In this thesis DPMJET-III, an event generator with sophisticated microscopic models for hadronic and nuclear interactions, has been modified to fulfill the missing requirements for cascade physics, including

- the possibility to switch between different projectile-target combinations in run-time,
- smooth extrapolation proton-proton and meson-nucleon up to 1 PeV center-of-mass using the internal models.

The model has been validated against an extensive set of data from accelerators, including the LHC. After applying corrections to the source code, including a new behavior of the hard QCD cross-section and updating the parton density functions, it was found that the generator can describe a large fraction of LHC minimum-bias data with reasonable precision. However, a deviation from data persisted in charged-particle multiplicity distributions, i.e.

the model produced too many high-multiplicity events while average particle numbers were normal, pointing to a problem with the elastic impact parameter amplitude. The question, if possibly the black disk limit has been reached at the LHC, has been answered through an investigation using recent data from the TOTEM experiment. A numerical analysis revealed that

- the black disk limit is not exceeded if the amplitude function is complex and it respects the dip structure in elastic scattering,
- a purely real or simplified functional form for the amplitude would exceed the black disc limit at the LHC,
- even if the limit is not exceeded, its proximity influences the multiplicity distributions in the observed way.

This fact points to a general problem with multi-component eikonal models that include a perturbatively calculated hard partonic cross-section. A solution on a microscopic level would require drastic changes to fundamental physical models of DPMJET-III. As a central (detector) phenomenon this feature has no significant influence on cascade related forward particle distributions, and has to remain as an open question for a future investigation. Although some general re-tuning was performed, nuclear data has been left out and will require further parameter and model optimizations. A few issues can be found at energies of fixed target experiments, in particular regarding baryon production spectra. A deficit in inclusive muon calculations needs additional studies, as well.

When the new version of DPMJET-III is completed, it will be used in calculations extending to lower energies and it can serve as full model in cascade packages, such as FLUKA or CORSIKA. Calculations for FCC and LHC will profit from the improved high-energy behavior and proper treatment of secondary meson-nucleon interactions in the same theoretical framework. In more precise astrophysical multi-messenger predictions of neutrino and photon fluxes, DPMJET-III can serve as a possibility to simulate nuclear interactions in combination with photo-hadronic processes consistently.

The solution of atmospheric cascades using the matrix approach is to large extent completed and the code is public. The applicability to other domains, for example in efficient solvers for cosmic ray acceleration and transport problems, need to be investigated in detail by populating the energy loss terms.



As the person who deeply shaped my scientific reasoning, I would like to express my deep gratitude to my supervisor Dr. Ralph Engel. His guidance through the subtleties and pitfalls of the difficult subject of hadronic interactions was crucially important for acquiring not only factual knowledge, but also for developing the appropriate state of mind when facing topics where a "correct" solution does not exist.

I would like to thank Prof. Dr. Dr. h.c. Johannes Blümer and Priv.-Doz. Dr. Stefan Gieseke for accepting me as doctoral student in their institute, for their prompt replies to my mails and for supporting me financially with traveling funds over the years.

I am expressing the deepest possible gratitude to my best friend and mentor Arno Caspelherr, who unfortunately deceased shortly before the completion of this thesis and can not experience in person the results of the seeds he planted over the past decade of my life. He acted in the background of my scientific career, constantly regenerating my curiosity and enthusiasm for science. By demonstrating humility and wisdom, he succeeded in pointing me and others to the aspects of life which really matter.

Thanks to my CERN supervisor Dr. Alfredo Ferrari, who supported me with his professional advice and his readiness to help. He, together with Dr. Francesco Cerutti, hosted me for more than three years in the EN-STI-EET section at CERN in optimal working conditions.

I am grateful to Prof. Dr. Thomas K. Gaisser who provoked my wish to work on hadronic interactions and to improve atmospheric cascade calculations.

My friends and colleagues from CERN, in particular Dr. Thiago Viana Miranda Lima, Letizia Di Giulio, Elvis Fornasiere, Christelle Gaignant and Leonel Morejon Hernandez, I would like to thank for the amazing time, the tasty barbecue sessions and for plenty of inspiring interdisciplinary discussions.

To my friends and colleagues in Karlsruhe, especially Colin Baus, Felix Riehn, Igor Katkov and Daniela Mockler, I am very grateful for succeeding to always give me the feeling of being at my home institute despite the short stays and for helping me out with the bad sense of orientation in the center of Karlsruhe.

My special thanks goes to my friends Stefanie Moser, Katharina Caspelherr, Jan Stodt and particularly to my parents who supported me practically and mentally in every possible way.

I gratefully acknowledge the support from by the Wolfgang Gentner Programme of the Federal Ministry of Education and Research (BMBF) at CERN.



# Bibliography

- [1] A. Aab et al. “Depth of maximum of air-shower profiles at the Pierre Auger Observatory. II. Composition implications.” *Phys. Rev. D*, volume 90(1) 122006, December 2014.
- [2] A. Aab et al. “Muons in air showers at the Pierre Auger Observatory: Mean number in highly inclined events.” *Physical Review D*, volume 91(3) 032003, February 2015.
- [3] G. Aad et al. “Charged-particle multiplicities in pp interactions measured with the ATLAS detector at the LHC.” *New J. Phys.*, volume 13(5) 3033, May 2011.
- [4] G. Aad et al. “Rapidity gap cross sections measured with the ATLAS detector in pp collisions at  $\sqrt{s} = 7$  TeV.” *The European Physical Journal C - Particles and Fields*, volume 72(3) 1, March 2012.
- [5] K. Aamodt et al. “Charged-particle multiplicity measurement in proton–proton collisions at  $\sqrt{s} = 0.9$  and 2.36 TeV with ALICE at LHC.” *The European Physical Journal C - Particles and Fields*, volume 68(1-2) 89, 2010.
- [6] K. Aamodt et al. “Charged-particle multiplicity measurement in proton–proton collisions at  $\sqrt{s} = 7$  TeV with ALICE at LHC.” *The European Physical Journal C - Particles and Fields*, volume 68(3-4) 345, 2010.
- [7] M. G. Aartsen et al. “Measurement of Atmospheric Neutrino Oscillations with IceCube.” *Phys. Rev. Lett.*, volume 111(8) 081801, August 2013.
- [8] M. G. Aartsen et al. “Determining neutrino oscillation parameters from atmospheric muon neutrino disappearance with three years of IceCube DeepCore data.” *Phys. Rev. D*, volume 91(7) 072004, April 2015.
- [9] M. G. Aartsen et al. “Development of a general analysis and unfolding scheme and its application to measure the energy spectrum of atmospheric neutrinos with IceCube.” *Eur. Phys. J. C*, volume 75(3) 116, March 2015.

- [10] R. Abbasi et al. “Indications of Intermediate-scale Anisotropy of Cosmic Rays with Energy Greater Than 57 EeV in the Northern Sky Measured with the Surface Detector of the Telescope Array Experiment.” *The Astrophysical Journal Letters*, volume 790(2) L21, August 2014.
- [11] B. Abelev et al. “Measurement of inelastic, single- and double-diffraction cross sections in proton-proton collisions at the LHC with ALICE.” *Eur. Phys. J. C*, volume 73 2456, June 2013.
- [12] P. Achard et al. “Measurement of the atmospheric muon spectrum from 20 to 3000 GeV.” *Physics Letters B*, volume 598(1) 15, September 2004.
- [13] P. Adamson et al. “Measurement of the atmospheric muon charge ratio at TeV energies with the MINOS detector.” *Phys. Rev. D*, volume 76(5) 52003, September 2007.
- [14] P. Adamson et al. “Observation of muon intensity variations by season with the MINOS far detector.” *Phys. Rev. D*, volume 81(1), January 2010.
- [15] O. Adriani et al. “PAMELA Measurements of Cosmic-Ray Proton and Helium Spectra.” *Science*, volume 332(6025) 69, March 2011.
- [16] N. Agafonova et al. “Measurement of the TeV atmospheric muon charge ratio with the complete OPERA data set.” *The European Physical Journal C - Particles and Fields*, volume 74(7) 1, July 2014.
- [17] M. Aguilar et al. “Precision Measurement of the Proton Flux in Primary Cosmic Rays from Rigidity 1 GV to 1.8 TV with the Alpha Magnetic Spectrometer on the International Space Station.” *Phys. Rev. Lett.*, volume 114(17) 171103, April 2015.
- [18] E.-J. Ahn. “Cosmic ray interaction event generator SIBYLL 2.1.” *Phys. Rev. D*, volume 80(9) 094003, June 2009.
- [19] E.-J. Ahn et al. “Sibyll with charm.” Technical Report arXiv:1102.5705, February 2011.
- [20] H. S. Ahn et al. “Energy Spectra of Cosmic-ray Nuclei at High Energies.” *ApJ*, volume 707(1) 593, December 2009.
- [21] H. S. Ahn et al. “Discrepant Hardening Observed in Cosmic-ray Elemental Spectra.” *The Astrophysical Journal Letters*, volume 714(1) L89, May 2010.
- [22] J. Alcaraz et al. “Protons in near earth orbit.” *Physics Letters B*, volume 472(1–2) 215, 2000.
- [23] G. Altarelli, R. Kleiss and C. Verzegnassi (eds.). *Workshop on Z Physics at LEP1 : General Meetings, vol. 1 : Standard Physics*. CERN, 1989.

- [24] U. Amaldi and K. R. Schubert. “Impact Parameter Interpretation of Proton Proton Scattering from a Critical Review of All ISR Data.” *Nucl.Phys.*, volume B166 301, 1980.
- [25] G. Antchev and others. “Luminosity-independent measurements of total, elastic and inelastic cross-sections at  $s = 7$  TeV.” *Europhys. Lett.*, volume 101 21004, 2013.
- [26] W. D. Apel and others. “Kneelike structure in the spectrum of the heavy component of cosmic rays observed with KASCADE-Grande.” *Phys. Rev. Lett.*, volume 107 171104, 2011.
- [27] ATLAS Collaboration. “ATLAS Computing.” Technical Report CERN-LHCC-2005-022, CERN, 2005.
- [28] ATLAS Collaboration. “Charged-particle distributions in  $\sqrt{s} = 13$  TeV p p interactions measured with the ATLAS detector at the LHC.” Technical report, Geneva, July 2015.
- [29] ATLAS Collaboration. “Measurement of the Inelastic Proton-Proton Cross Section at  $\sqrt{s} = 13$  TeV with the ATLAS Detector at the LHC.” Technical report, Geneva, August 2015.
- [30] P. Aurenche et al. “DTUJET-93: Sampling inelastic proton-proton and antiproton-proton collisions according to the two-component dual parton model.” *CPC*, volume 83(1) 107, 1994.
- [31] M. Ave et al. “Composition of Primary Cosmic-Ray Nuclei at High Energies.” *ApJ*, volume 678(1) 262, May 2008.
- [32] R. D. Ball et al. “Parton distributions for the LHC run II.” *Journal of High Energy Physics*, volume 2015(4) 1, April 2015.
- [33] V. Barone and E. Predazzi. *High-Energy Particle Diffraction*. Springer Science & Business Media, Berlin, Heidelberg, March 2013.
- [34] P. Bartalini et al. “Multi-Parton Interactions at the LHC.” *arXiv*, November 2011. [1111.0469](#).
- [35] R. Battiston et al. “Proton-antiproton elastic scattering at four-momentum transfer up to  $0.5$  GeV $^2$  at the CERN SPS collider.” *Physics Letters B*, volume 127(6) 472, August 1983.
- [36] P. Berghaus, T. Montaruli and J. Ranft. “Charm production in DPM-JET.” *J. Cosmol. Astropart. Phys.*, volume 2008(06) 003, June 2008.
- [37] T. Bergmann et al. “One-dimensional hybrid approach to extensive air shower simulation.” *Astroparticle Physics*, volume 26(6) 420, January 2007.

- [38] A. Bhattacharya et al. “Perturbative charm production and the prompt atmospheric neutrino flux in light of RHIC and LHC.” *JHEP*, volume 1506(6) 110, February 2015.
- [39] M. Block and R. Cahn. “High-Energy  $p\bar{p}$  and  $pp$  Forward Elastic Scattering and Total Cross-Sections.” *Rev.Mod.Phys.*, volume 57 563, 1985.
- [40] J. Blümner, R. Engel and J. R. Hörandel. “Cosmic rays from the knee to the highest energies.” *Progress in Particle and Nuclear Physics*, volume 63(2) 293, October 2009.
- [41] T. T. Böhlen et al. “The FLUKA Code: Developments and Challenges for High Energy and Medical Applications.” *Nuclear Data Sheets*, volume 120 211, June 2014.
- [42] G. Bossard et al. “Cosmic ray air shower characteristics in the framework of the parton-based Gribov-Regge model NEXUS.” *Phys. Rev. D*, volume 63(5) 054030, February 2001.
- [43] M. Bozzo et al. “Elastic scattering at the CERN SPS collider up to a four-momentum transfer of  $1.55 \text{ GeV}^2$ .” *Physics Letters B*, volume 155(3) 197, May 1985.
- [44] E. V. Bugaev et al. “Prompt Leptons in Cosmic Rays.” *Nuovo Cim.*, volume C12(1) 41, 1989.
- [45] E. V. Bugaev et al. “Atmospheric muon flux at sea level, underground, and underwater.” volume 58(5) 54001, September 1998.
- [46] A. Capella et al. “Dual parton model.” *Phys.Rept.*, volume 236 225, 1994.
- [47] S. Chatrchyan et al. “Measurement of pseudorapidity distributions of charged particles in proton–proton collisions at  $\sqrt{s} = 8 \text{ TeV}$  by the CMS and TOTEM experiments.” *The European Physical Journal C - Particles and Fields*, volume 74(10) 1, 2014.
- [48] P. D. B. Collins. *An Introduction to Regge Theory and High-Energy Physics*. Cambridge Monographs on Mathematical Physics. Cambridge Univ. Press, Cambridge, UK, 2009.
- [49] R. Corke and T. Sjöstrand. “Interleaved parton showers and tuning prospects.” *Journal of High Energy Physics*, volume 2011(3) 1, March 2011.
- [50] J. R. Cudell, A. Lengyel and E. Martynov. “Soft and hard Pomerons in hadron elastic scattering at small  $t$ .” *Phys. Rev. D*, volume 73(3) 034008, February 2006.

- [51] A. de Roeck and R. S. Thorne. “Structure functions.” *Progress in Particle and Nuclear Physics*, volume 66(4) 727, October 2011.
- [52] D. d’Enterria et al. “Constraints from the first LHC data on hadronic event generators for ultra-high energy cosmic-ray physics.” *Astroparticle Physics*, volume 35(2) 98, September 2011.
- [53] P. Desiati and The IceCube Collaboration. “Seasonal variation of atmospheric neutrinos in IceCube .” In “ICRC 2013,” .
- [54] M. Dobbs and J. B. Hansen. “The HepMC C++ Monte Carlo event record for High Energy Physics.” *CPC*, volume 134(1) 41, February 2001.
- [55] S. Donnachie et al. *Pomeron Physics and QCD*. Cambridge University Press, November 2002.
- [56] H.-J. Drescher and G. Farrar. “Air shower simulations in a hybrid approach using cascade equations.” *Phys. Rev. D*, volume 67(11) 116001, June 2003.
- [57] S. Dulat et al. “The CT14 Global Analysis of Quantum Chromodynamics.” June 2015. 1506.07443.
- [58] R. Enberg, M. H. Reno and I. Sarcevic. “Prompt neutrino fluxes from atmospheric charm.” *Phys. Rev. D*, volume 78(4) 43005, August 2008.
- [59] R. Engel. “Photoproduction within the two-component Dual Parton Model: Amplitudes and cross sections.” *Z. Phys. C - Particles and Fields*, volume 66(1) 203, March 1995.
- [60] R. Engel. *Hadronic Interactions of Photons at High Energies* . Ph.D. thesis, April 1997.
- [61] R. Engel and J. Ranft. “Hadronic photon-photon interactions at high energies.” *Phys. Rev. D*, volume 54(7) 4244, October 1996.
- [62] A. Fedynitch, J. Becker Tjus and P. Desiati. “Influence of hadronic interaction models and the cosmic ray spectrum on the high energy atmospheric muon and neutrino flux.” *Phys. Rev. D*, volume 86(11) 114024, December 2012.
- [63] A. Ferrari et al. *FLUKA: A multi-particle transport code (program version 2005)*. CERN, Geneva, 2005.
- [64] R. Fletcher, P. Lipari and T. Stanev. “SIBYLL: An Event generator for simulation of high-energy cosmic ray cascades.” *Phys.Rev.*, volume D50 5710, 1994.
- [65] T. K. Gaisser. *Cosmic rays and particle physics*. Cambridge Univ Pr, 1990.

- [66] T. K. Gaisser. “Spectrum of cosmic-ray nucleons, kaon production, and the atmospheric muon charge ratio.” *Astroparticle Physics*, volume 35(12) 801, July 2012.
- [67] T. K. Gaisser and M. Honda. “Flux of atmospheric neutrinos.” *Annual Review of Nuclear and Particle Sciences*, volume 52 153, 2002.
- [68] T. K. Gaisser and S. R. Klein. “A new contribution to the conventional atmospheric neutrino flux.” *Astroparticle Physics*, volume 64 IS - 13, September 2014.
- [69] T. K. Gaisser, T. Stanev and S. Tilav. “Cosmic ray energy spectrum from measurements of air showers.” *Front. Phys.*, volume 8(6) 748, 2013.
- [70] M. V. Garzelli, S. Moch and G. Sigl. “Lepton fluxes from atmospheric charm revisited.” July 2015. 1507.01570.
- [71] M. Glück, E. Reya and A. Vogt. “Dynamical parton distributions revisited.” *The European Physical Journal C - Particles and Fields*, volume 5(3) 461, September 1998.
- [72] M. Glück et al. “On the role of heavy flavor parton distributions at high energy colliders.” *Physics Letters B*, volume 664(1-2) 133, June 2008.
- [73] K. Golec-Biernat and M. Wusthoff. “Saturation effects in deep inelastic scattering at low  $Q^2$  and its implications on diffraction.” *Phys. Rev. D*, volume 59(1) 014017, January 1999.
- [74] E. W. Grashorn et al. “The atmospheric charged kaon/pion ratio using seasonal variation methods.” *Astroparticle Physics*, volume 33(3) 140, April 2010.
- [75] V. N. Gribov. “A Reggeon Diagram Technique.” *Sov. Phys. JETP*, volume 53 654, 1968.
- [76] V. N. Gribov and A. A. Migdal. “Properties of the pomeranchuk pole and the branch cuts related to it at low momentum transfer.” *Sov. J. Nucl. Phys.*, volume 8 583, 1969.
- [77] G. Gustafson et al. “Total, inelastic and (quasi-)elastic cross sections of high energy  $pA$  and  $\gamma^*A$  reactions with the dipole formalism.” *Journal of High Energy Physics*, volume 2015(10) 1, October 2015.
- [78] D. Heck and T. Pierog. *Extensive Air Shower Simulation with CORSIKA: A User’s Guide (Version 74xxx)*, September 2013.
- [79] D. Heck et al. “CORSIKA: A Monte Carlo Code to Simulate Extensive Air Showers.” Technical Report FZKA 6019, Karlsruhe, 1998.

- [80] M. Honda et al. “Calculation of atmospheric neutrino flux using the interaction model calibrated with atmospheric muon data.” *Phys. Rev. D*, volume 75(4), February 2007.
- [81] M. Honda et al. “Atmospheric neutrino flux calculation using the NRLMSISE-00 atmospheric model.” *Phys. Rev. D*, volume 92(2) 023004, July 2015.
- [82] J. R. Hörandel. “On the knee in the energy spectrum of cosmic rays.” *Astroparticle Physics*, volume 19(2) 193, 2003.
- [83] J. I. Illana et al. “Atmospheric muon and neutrino fluxes at very high energy.” *Astroparticle Physics*, volume 34(9) 663, October 2010.
- [84] G. Ingelman and P. E. Schlein. “Jet structure in high mass diffractive scattering.” *Phys.Lett.*, volume B152 256, 1985.
- [85] L. L. Jenkovszky, A. I. Lengyel and D. I. Lontkovskyi. “The pomeron and odderon in elastic, inelastic and total cross-sections at the LHC.” *International Journal of Modern Physics A*, volume 26(27n28) 4755, November 2011.
- [86] B. J. P. Jones. *Sterile Neutrinos in Cold Climates*. Ph.D. thesis, microboone-docdb.fnal.gov, Fermi National Accelerator Laboratory (FNAL), Batavia, IL (United States), September 2015.
- [87] A. B. Kaidalov. “The quark-gluon structure of the pomeron and the rise of inclusive spectra at high energies.” *Physics Letters B*, volume 116(6) 459, October 1982.
- [88] N. N. Kalmykov, S. S. Ostapchenko and A. I. Pavlov. “Quark-gluon-string model and EAS simulation problems at ultra-high energies.” *Nuclear Physics B - Proceedings Supplements*, volume 52(3) 17, 1997.
- [89] T. Kasemets. “Inclusion of Parton Distribution Functions in PYTHIA8.” February 2010. 1002.4376.
- [90] V. Khachatryan et al. “Charged particle multiplicities in pp interactions at  $\sqrt{s} = 0.9, 2.36$ , and  $7 \text{ TeV}$ .” *Journal of High Energy Physics*, volume 2011(1) 1, January 2011.
- [91] V. Khachatryan et al. “Measurement of diffractive dissociation cross sections in p p collisions at  $\sqrt{s} = 7 \text{ TeV}$ .” *Phys. Rev. D*, volume 92(1) 012003, July 2015.
- [92] V. Khachatryan et al. “Pseudorapidity distribution of charged hadrons in proton-proton collisions at  $\sqrt{s} = 13 \text{ TeV}$ .” July 2015.
- [93] A. A. Kochanov, T. S. Sinegovskaya and S. I. Sinegovsky. “High-energy cosmic-ray fluxes in the Earth atmosphere: Calculations vs experiments.” *Astroparticle Physics*, volume 30(5) 219, December 2008.

- [94] H.-L. Lai et al. “Parton distributions for event generators.” *Journal of High Energy Physics*, volume 2010(4) 1, April 2010.
- [95] P. Lipari. “Lepton spectra in the earth’s atmosphere.” *Astropart.Phys.*, volume 1 195, 1993.
- [96] L. N. Lipatov. “Small-x physics in perturbative QCD.” *Physics Reports*, volume 286 131, July 1997.
- [97] J. Lunze. *Regelungstechnik 1*. Springer-Lehrbuch. Springer Berlin Heidelberg, Berlin, Heidelberg, 2010.
- [98] J. Lunze. *Regelungstechnik 2*. Springer-Lehrbuch. Springer Berlin Heidelberg, Berlin, Heidelberg, 2010.
- [99] A. D. Martin, M. G. Ryskin and A. M. Stasto. “Prompt Neutrinos from Atmospheric cbar c Production and the Gluon at Very Small x.” *Acta Physica Polonica B*, volume 34(6) 3273, June 2003.
- [100] A. D. Martin and T. D. Spearman. *Elementary Particle Theory*. North Holland Publishing Company, Amsterdam, 1970.
- [101] R. C. Martin. *Agile Software Development*. Principles, Patterns, and Practices. Prentice Hall, 2003.
- [102] D. Müller. “Generalized Parton Distributions: Visions, Basics, and Realities.” *Few-Body Systems*, volume 55(5) 317, June 2014.
- [103] S. Muraro. *The Calculation of atmospheric muon flux using the FLUKA Monte Carlo code*. Ph.D. thesis, 2007.
- [104] E. Nagy et al. “Measurements of elastic proton-proton scattering at large momentum transfer at the CERN intersecting storage rings.” *Nuclear Physics B*, volume 150 221, 1979.
- [105] V. A. Naumov, T. S. Sinegovskaya and S. I. Sinegovsky. “The K(lepton 3)form-factors and atmospheric neutrino flavor ratio at high-energies.” *CPC*, volume A111 129, 1998.
- [106] K. A. Olive and Particle Data Group. “Review of Particle Physics.” *Chinese Physics C*, volume 38(9) 090001, August 2014.
- [107] S. Ostapchenko. “QGSJET-II: towards reliable description of very high energy hadronic interactions.” *Nuclear Physics B - Proceedings Supplements*, volume 151(1) 143, January 2006.
- [108] S. Ostapchenko. “Monte Carlo treatment of hadronic interactions in enhanced Pomeron scheme: QGSJET-II model.” *Phys. Rev. D*, volume 83(1) 014018, January 2011.

- [109] A. D. Panov et al. “Energy spectra of abundant nuclei of primary cosmic rays from the data of ATIC-2 experiment: Final results.” *Bulletin of the Russian Academy of Sciences: Physics*, volume 73 564, June 2009.
- [110] B. Peters. *Nuovo Cimento Nuovo Cimento*, volume 22 800, 1961.
- [111] P. Peterson. “F2PY: a tool for connecting Fortran and Python programs.” *International Journal of Computational Science and Engineering*, volume 4(4) 296, 2009.
- [112] V. A. Petrov and A. V. Prokudin. “The first three pomerons...” *Eur. Phys. J. C*, volume 23(1) 135, March 2002.
- [113] J. M. Picone et al. “NRLMSISE-00 empirical model of the atmosphere: Statistical comparisons and scientific issues.” *Journal of Geophysical Research: Space Physics (1978–2012)*, volume 107(A12) SIA 15, December 2002.
- [114] T. Pierog and K. Werner. “EPOS Model and Ultra High Energy Cosmic Rays.” *Nuclear Physics B - Proceedings Supplements*, volume 196(0) 102, December 2009.
- [115] W. H. Press et al. *Numerical recipes in C. The art of scientific computing*. Cambridge: University Press, 1992.
- [116] J. Ranft. “DPMJET version II.5: Sampling of hadron hadron, hadron - nucleus and nucleus-nucleus interactions at accelerator and cosmic ray energies according to the two component dual parton model: Code manual.” Technical Report SI-99-6, University of Siegen, 1999.
- [117] F. Riehn et al. “A new version of the event generator Sibyll.” *Proc. of 34th Int. Cosmic Ray Conf., The Hague*, 2015.
- [118] F. Riehn et al. “Charm production in SIBYLL.” *ISVHECRI 2014 - 18th International Symposium on Very High Energy Cosmic Ray Interactions*, August 2015.
- [119] S. Roesler, R. Engel and J. Ranft. “The Monte Carlo Event Generator DPMJET-III.” *arXiv*, December 2000. [hep-ph/0009327v1](#).
- [120] S. Rösler. *Aspects of Nuclear Collisions of Relevance to Cosmic Ray Cascades*. Ph.D. thesis, February 1997.
- [121] M. G. Ryskin, A. D. Martin and V. A. Khoze. “Soft processes at the LHC I: Multi-component model.” *Eur. Phys. J. C*, volume 60(2) 249, February 2009.
- [122] A. Sherstnev and R. S. Thorne. “Parton distributions for LO generators.” *Eur. Phys. J. C*, volume 55(4) 553, June 2008.

- [123] T. S. Sinegovskaya, A. D. Morozova and S. I. Sinegovsky. “High-energy neutrino fluxes and flavor ratio in the Earth’s atmosphere.” *Phys.Rev.*, volume D91(6) 063011, July 2014.
- [124] T. Sjöstrand, S. Mrenna and P. Skands. “PYTHIA 6.4 physics and manual.” *Journal of High Energy Physics*, volume 2006(05) 026, May 2006.
- [125] T. Sjöstrand, S. Mrenna and P. Skands. “A brief introduction to PYTHIA 8.1.” *Computer Physics Communications*, volume 178(11) 852, June 2008.
- [126] T. Sjöstrand and P. Z. Skands. “Multiple interactions and the structure of beam remnants.” *Journal of High Energy Physics*, volume 2004(03) 053, March 2004.
- [127] T. Sjöstrand and M. van Zijl. “Multiple Parton-parton Interactions in an Impact Parameter Picture.” *Phys.Lett.*, volume B188(1) 149, 1987.
- [128] T. Sjöstrand et al. “An introduction to PYTHIA 8.2.” *CPC*, volume 191 159, June 2015.
- [129] U. S. Standard Atmosphere. “US Standard Atmosphere, 1976.” *US Gov. Print. Off., Washington, DC*, 1976.
- [130] R. P. Tewarson. *Sparse matrices*. Math. Sci. Eng. Academic Press, New York, NY, 1973.
- [131] The ATLAS Collaboration et al. “Measurement of the inelastic proton-proton cross-section at  $\sqrt{s} = 7$  TeV with the ATLAS detector.” *Nature Communications*, volume 2 463, September 2011.
- [132] The CMS Collaboration. “Measurement of the charge ratio of atmospheric muons with the CMS detector.” *Physics Letters B*, volume 692(2) 83, August 2010.
- [133] The LHCb Collaboration et al. “Measurement of charged particle multiplicities and densities in  $pp$  collisions at  $\sqrt{s} = 7$  TeV in the forward region.” *The European Physical Journal C - Particles and Fields*, volume 74(5) 2888, May 2014.
- [134] The NA49 Collaboration. “Inclusive production of charged pions in p+p collisions at 158 GeV/c beam momentum.” *Eur. Phys. J. C*, volume 45(2) 343, December 2005.
- [135] The NA49 Collaboration et al. “Inclusive production of charged kaons in p+p collisions at 158 GeV/c beam momentum and a new evaluation of the energy dependence of kaon production up to collider energies.” *Eur. Phys. J. C*, volume 68(1-2) 1, June 2010.

- [136] The TOTEM Collaboration et al. “First measurement of the total proton-proton cross-section at the LHC energy of  $\sqrt{s} = 7$  TeV.”
- [137] The TOTEM Collaboration et al. “Proton-proton elastic scattering at the LHC energy of  $\sqrt{s} = 7$  TeV.” *EPL*, volume 95(4) 41001, August 2011.
- [138] M. Thunman, G. Ingelman and P. Gondolo. “Charm production and high energy atmospheric muon and neutrino fluxes.” *Astroparticle Physics*, volume 5(3–4) 309, 1996.
- [139] S. Tilav et al. “Atmospheric Variations as observed by IceCube.” *arXiv*, January 2010. 1001.0776v2.
- [140] A. N. Vall, V. A. Naumov and S. I. Sinegovsky. “Hadronic Component of High-energy Cosmic Rays and Growth of Inelastic Cross-sections. (In Russian).” *Sov. J. Nucl. Phys.*, volume 44 806, 1986.
- [141] K. R. Wadleigh and I. L. Crawford. *Software optimization for high-performance computing*. Prentice Hall PTR, Upper Saddle River, N.J., 2000.
- [142] V. I. Zatsepin and N. V. Sokolskaya. “Three component model of cosmic ray spectra from 10 GeV to 100 PeV.” *Astronomy and Astrophysics*, volume 458(1) 1, October 2006.



# Appendix A

## Supporting programs

All software which can have multiple purposes are written and maintained as standalone tools or libraries. In case a program or library reaches a stable, or at least beta state, and it could be of interest to the community, it is declared open source and published to a broader community. Typically numerical calculations require a set of re-occurring "ingredients", for example a database of particle properties or numerical models of cosmic ray spectra. The community should feel free to use, modify or fork the tools according to their needs. In this chapter the applications created for the astroparticle physics field of this project are shortly introduced.

### A.1 Package `CRFluxModels`

The collection of high-energy cosmic ray flux models has its origin in a part of a previous work [62]. The idea behind the module was to create a unique interface and centralize the published models in one place. It contains one abstract base class which requires the definition of a single virtual method `nucleus_flux(corsika_id, E)` in the derived class. The method is expected to return the flux of protons or nuclei at the top of the atmosphere as a function of their energy and the nucleus code according to the CORSIKA air-shower simulator [79]. The implementation of cosmic ray flux parameterizations is not further restricted. Details about the included models can be found in section 2.2.1 and the software documentation<sup>22</sup>.

### A.2 Package `ParticleDataTool`

The package fulfills the task to convert proprietary particle codes into a common standard and to provide access to a database of particle properties, such as mass, name and charge.

The `class PYTHIAParticleData` extracts particle properties from an XML file, which is part of the PYTHIA 8 Monte Carlo program [125]. The file is

---

<sup>22</sup> <http://crfluxmodels.readthedocs.org>

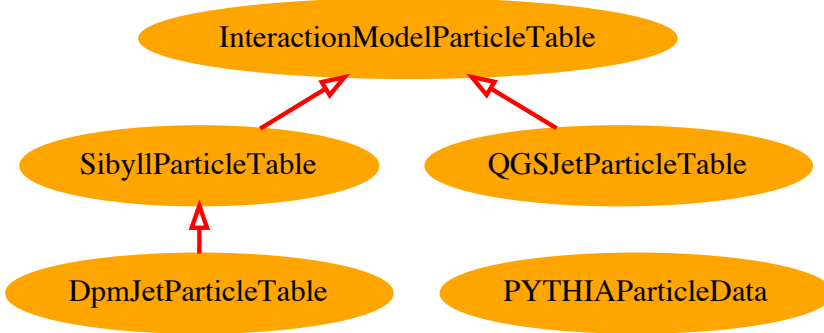


Figure A.1: (UML) Class diagram of the `ParticleDataTool` module.

parsed, filtered for information relevant for particle cascades and then converted into a lightweight database based on PYTHON dictionaries. To avoid the parsing step at each initialization, the data structures are serialized on disc using the `pickle` module.

The rest of the classes in this module implements particle code conversions. The `HEPEVT` [23] common block is the de-facto standard for FORTRAN and the `HepMC` [54] interface for C++ based Monte Carlo generators. Although these standards have been established in the early 90's and 2000's, respectively, the event generators use proprietary internal particle codes for historical or efficiency reasons. To conform with the standards and reduce error-prone code, all MCEQ related packages utilize the *PDG Monte Carlo Particle Numbering Scheme* [106] as a common particle indexing code.

### A.3 Package `PyInteractionModels`

This tool is a collection of event generator source codes together with their standardized PYTHON interfaces. The main goal is to provide an abstraction layer between the Monte Carlo programs and other code which use the generators through the standardized interface. All of the cosmic ray Monte Carlos are written in FORTRAN 77 and which can be accessed from PYTHON by using the program F2PY [111]. The tool parses the sources, generates function signatures and compiles a binary shared library with PYTHON bindings. With respect to the age of the FORTRAN codes and their various coding styles, F2PY performs remarkably well without any issue.

At the moment of writing the program contains the following event generators:

- SIBYLL-2.1 [64, 18],
- various development versions of SIBYLL-2.2/2.3 [118, 117],
- QGSJET-01c [88],
- QGSJET-II-03 and QGSJET-II-04 [108],

- DPMJET 3.06 [119],
- PYTHIA 6.427 [124].

The basic interface contains classes for each interaction model based on derived from three base classes:

- `class MCRun`: wrapper class for initialization in event loop for fixed-target or collider kinematics at a single collision energy,
- `class MCEvent`: calculates typical collider variables, such as momenta, pseudo-rapidity  $\eta$ , Feynman- $x_F$ ,
- `class CascadeRun`: initialization at the highest energy for various projectile-target combinations. The event loop expects to be called from the `SpectraForMCEq` (see section A.4) package for fixed-target or collider kinematics at a single collision energy,
- `class CascadeEvent`: calculates the minimum amount of kinematic variables relevant for particle cascades in laboratory frame, i.e.  $E$ ,  $p_z$ .

The goal of the inheritance structure is to read out the elementary kinematic variables  $p_x$ ,  $p_y$ ,  $p_z$ ,  $E$  and  $m$  from the proprietary event common block in the constructor of derived class. Then, the invocation of the base class constructor calculates the more complex variables. Although written in PYTHON the code achieves very high performance by minimizing memory copy operations when casting FORTRAN arrays to `numpy` arrays.

## A.4 Package `SpectraForMCEq`

The calculation of inclusive particle spectra for MCEQ requires batch execution of event generators on general computing clusters. The task of this management tool is to create input files for batch systems, to handle the granularity of parallel computing chunks, to maintain the integrity of the simulated dataset and to re-submit missing or canceled calculations if necessary. The common energy grid for MCEQ is initially defined here.

The parallelization method is based on simple multiprocessing of similar chunks of work. In each chunk a single event generator is run for a series of energies and one projectile target combination. To obtain very smooth distributions for rare (charm) particles at large  $x_F$  ca. 2.5 million events per energy point are necessary, requiring roughly 3500 CPUh to process. Smooth pion and kaon spectra can be obtained with a factor of 100 less statistics. The script writes the histograms on disk in a data structure indexed as a function of projectile energy, projectile particle ID and secondary particle ID. After verifying the integrity the chunks are merged into one big data structure and converted in the appropriate matrix form for MCEQ.

## A.5 Tool PYTHIADECAYS

The inclusive spectra of decay products is simulated with the PYTHIA 8.180 Monte Carlo [125]. The software is fully written in C++ and became one of the baseline general purpose generators for collider physics during the LHC Run-1, replacing the discontinued FORTRAN version 6.428. The code is very well documented<sup>23</sup>, including the mathematical details of its physical models and parameters [124]. Here, it is used to simulate repeatedly the decay of all kinds of unstable mesons for  $2 \cdot 10^7$  times and to obtain a smooth distribution of daughter energies. MCEQ requires histograms of daughter energies and rates for mother particles at each point in the energy grid. To avoid aliasing or re-binning effects, the program follows this approach:

1. clear the particle stack,
2. put one hadron at rest on the stack and declare it unstable,
3. launch decay routine,
4. loop through stable daughters,
5. for each point of the energy grid, calculate the boost parameters, of the primary particle  $\beta$  and  $\gamma$
6. boost the four-vector of the daughter into this frame and fill its energy into the corresponding histogram.

The data analysis framework ROOT<sup>24</sup> is selected to represent the histograms, since its serialization mechanisms are very easy to use inside C++ programs. The calculation is split into several tens of jobs and carried out on a general purpose cluster. The ROOT tree files of the individual jobs are merged into one big file using the ROOT executable `hadd` and converted later into python data structures for MCEQ.

## A.6 Package `AcceleratorData`

This PYTHON package is a standardized database representation for a collection of experimental data of any kind. It contains measurements of cross-sections, multiplicities and all kinds of differential distributions. It is one of the abstraction layers between MCVD (see next section) and the various formats in which data points are published. Each set of points is derived from a base class, which contains defines convenience functions. A command line tool is provided to parse the files and to compile a database, based on PYTHON dictionaries. This relational database is stored on disk using the `pickle` module and it is therefore very small and efficient when used from other modules.

---

<sup>23</sup> <http://home.thep.lu.se/~torbjorn/pythia81html/Welcome.html>

<sup>24</sup> <https://root.cern.ch/>

Each set of data-points is accompanied by the official reference and, if obtained from a web recourse, the URL of the original table.

## A.7 MCVD - Monte Carlo ValiDation

The particle physics part in theses is mostly related to tuning and validation of FORTRAN based Monte Carlo event generators, in particular PHOJET, DPMJET and SIBYLL. As cosmic ray generators, they are covering a large span in interaction energies starting as low as  $\sqrt{s} = 5\text{-}10$  GeV up to several PeV in center-of-mass or hundreds of EeV in laboratory frame. After each change to the parameters or the models of a generator one wants to know at which part of the phase-space the modifications are effective and that across the whole energy range there are no unexpected results. Two tools are shared with the astroparticle physics part, the Packages `PyInteractionModels` (section A.3) and `ParticleDataTool` (section A.2).

The idea behind MCVD is to have a very efficient method to run a set of Monte Carlo generators and to compare the obtained distributions with experimental data. The event generators are internally very different, since they have been created in a time, when the standardization of interfaces in particle physics was not as common as now. To some extend the functionality can be compared to the popular Monte Carlo validation tool RIVET<sup>25</sup>. The idea

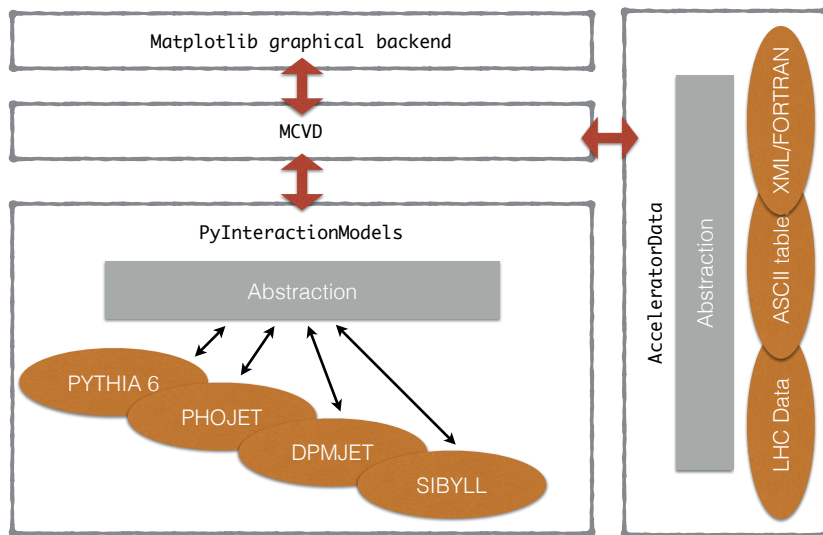


Figure A.2: Abstraction in MCVD.

of abstraction, the separation of the interaction model code from the graphical result representation, is sketched in Figure A.2. The responsibilities of The library for visualization is the very versatile PYTHON library `matplotlib`<sup>26</sup>.

The multi-threaded execution is governed by PYTHON's Pool (of workers) module from the `multiprocessing` package, where each task is launched in a

<sup>25</sup> <https://rivet.hepforge.org>

<sup>26</sup> <http://matplotlib.org>

separate operating system process. This approach allows to load individual instances of FORTRAN libraries, since usually each library can be only imported once per PYTHON process. The execution performance increases by the number of available cores. Before splitting individual runs into independent threads, MCVD performs a scheduling optimization. A single run is characterized by a set of settings, for example: PHOJET,  $pp$  collisions, 7 TeV center-of-mass, all particles with  $c\tau < 10^{-10}$  s stable, only charged final states). The scheduling optimization compares the settings of all requested histograms and computes the distributions for those with equal settings in one run of the event generator, reducing arithmetical computations of dependent variables to a minimum.

The approach to re-run the generators spend CPU time, instead of storing events to disk and run analysis software afterwards, is often more efficient. In particular at high energies each event can contain tens of thousands of particles, requiring gigabytes of space for a few thousand events.

The code has suffered from many modifications during its development and is not yet in an appropriate shape for publication, but it is foreseen to share it as PYTHON alternative to other available programs.

## Erklärung zur Eigenständigkeit der Dissertation

Ich versichere, dass ich diese Arbeit selbständig verfasst und keine anderen als die angegebenen Quellen und Hilfsmittel benutzt sowie Zitate kenntlich gemacht habe.

Karlsruhe, den 11.11.2015

---

Anatoli Fedynitch

Vorgelegt von: Dipl.-Phys. Dipl.-Ing. Anatoli Fedynitch

Abgabedatum: 11.11.2015